

ABSTRACT

CETINKAYA, MUSTAFA YAVUZ. Rapid Seismic Assessment of Alaska Highway Bridges Using a Direct Displacement-Based Methodology (Under the direction of Dr. Mervyn J. Kowalsky).

The invention of ShakeMap (by USGS) has led to use of HAZUS post-earthquake assessment methodology (by FEMA) for rapid seismic assessment of bridge structures via ShakeCast (by Caltrans/USGS) with the aim of determining inspection priorities. The HAZUS approach was developed by using coarse limit state definitions for the purpose of assessing bridges with limited information, hence it is not ideal for assessment of bridges whose limit states can be identified more accurately with available bridge metadata. Utilizing ShakeMap, a simple and accurate seismic assessment procedure for the case where bridge details are known can be preferable in lieu of the HAZUS method to determine inspection priorities.

In this research, the implementation of a displacement-based rapid assessment approach for Alaska highway bridges using ShakeMap is proposed. The approach is based on the direct displacement-based design (DDBD) methodology developed by Priestley et al. (2007), which allows for characterization of Multi Degree of Freedom (MDOF) structures by equivalent Single Degree of Freedom (SDOF) system properties (system displacement, damping and effective period) to a specified limit state. Limit state displacements of a set of bridges (three reinforced concrete and four reinforced concrete steel tube) from Alaska were identified at different performance levels. A scenario earthquake created from ShakeMap was used to check whether limit state displacements were achieved during a given earthquake scenario, which is an indication of damage level. An inspection priority list of the bridges based on the results of the direct displacement-based assessment (DDBA) approach was proposed. The accuracy of the DDBA was checked performing incremental dynamic analysis (IDA) with spectrum compatible records. The

results of IDA indicate that the DDBA method provides satisfactory estimates of the performance level of a bridge under a given seismic hazard. Finally, DDBA application of the three bridges under the ShakeMap of a real earthquake is shown.

© Copyright 2019 by Mustafa Yavuz Cetinkaya

All Rights Reserved

Rapid Seismic Assessment of Alaska Highway Bridges Using a Direct Displacement-Based
Methodology

by
Mustafa Yavuz Cetinkaya

A thesis submitted to the Graduate Faculty of
North Carolina State University
in partial fulfillment of the
requirements for the degree of
Master of Science

Civil Engineering

Raleigh, North Carolina
2019

APPROVED BY:

Dr. Mervyn J. Kowalsky
Chair of Advisory Committee

Dr. Ashly Cabas Mijares

Dr. James M. Nau

DEDICATION

To My Parents

BIOGRAPHY

Mustafa Yavuz Cetinkaya was born in 1991 in the city of Ankara, Turkey. He received his Bachelor of Science in Civil Engineering from Manisa Celal Bayar University in June 2013. He worked as a graduate student in Civil Engineering from September 2013 to November 2014 at Sakarya University, where he did research on equivalent-linear dynamic linear impedance functions in developing solution approaches for dynamic soil-foundation-interaction problems under the advice of Dr. Erkan Celebi. In November of 2014, he was rewarded with a study abroad fellowship from Turkish Ministry of National Education for a Master of Science study. He moved to Raleigh in January 2017 to pursue his master under the direction of Dr. Mervyn J. Kowalsky. His research interests include mainly performance-based seismic design and assessment of structures, structural dynamics, nonlinear response of structures and soil-foundation-structure interaction.

ACKNOWLEDGMENTS

I would like to express my gratitude to my advisor Dr. Mervyn J. Kowalsky for his support, patience and guidance throughout my research. It has been a great pleasure working with him and being part of his research group. I would also like to extend my appreciation to my committee members, Dr. James Nau and Dr. Ashly Cabas Mijares.

I would like to acknowledge Mr. Elmer Marx from AKDOT & PF for providing bridge plans for this research, and Dr. Eric Thompson from USGS for helping me to learn how to run scenario earthquakes from the ShakeMap software.

I give thanks to my friends and colleagues at the Constructed Facilities Lab, especially Arjun Jayaprakash, Rajprabhu Thangappa, and Diego Martinez for the time they devoted to discussing my research in a constructive manner.

In addition, many thanks to Tugay Demiraslan, Hussam Abu Nimeh, Abhinav Kumar Syal and Mayur Sharma for their companionship. I would also like to sincerely thank Emrah Tasdemir for being an older brother and a friend to me. This was true since my first day in Raleigh, and I am grateful to have known him.

Finally, I would have not been able to accomplish this success without the support of my parents, sister and brother. Their continuous support and belief in me were, is and will forever be inspiring, motivational and encouraging me to reach my career goals. I am truly thankful to each one of them.

TABLE OF CONTENTS

LIST OF TABLES	viii
LIST OF FIGURES	ix
CHAPTER 1	1
1. INTRODUCTION.....	1
1.1 Motivation.....	1
1.2 Organization.....	3
CHAPTER 2	5
2. LITERATURE REVIEW	5
2.1. Introduction.....	5
2.2. Fundamentals of Direct Displacement-Based Design	5
2.3. Direct Displacement-Based Assessment of Bridges.....	7
2.4. Hazard Definition for Rapid Seismic Assessment.....	12
2.4.1 Shake Map.....	12
2.4.2 Shake Map Scenario Methodology	14
2.5 HAZUS Bridge Damage Estimation.....	16
2.6 Study Plan and Objectives	17
CHAPTER 3.....	19
3. APPLIED DIRECT DISPLACEMENT-BASED APPROACH.....	19
3.1 Introduction.....	19
3.2 Performance Limit States.....	19
3.3 Critical Curvature Evaluation at Performance Limit States	21

3.3.1	Material Strength.....	21
3.3.2	Strain Limits.....	21
3.3.2.1	RC Bridge Piers.....	21
3.3.2.2	RCFST Bridge Piers.....	22
3.3.3	Material Models	24
3.4	Deformation Limit States and Equivalent Viscous Damping of the Bridge Piers.....	25
3.4.1	Deformation Limit States	25
3.4.1.1	RC Bridge Piers.....	25
3.4.1.2	RCFST Bridge Piers.....	27
3.4.2	Equivalent Viscous Damping.....	30
3.4.2.1	RC and RCFST Bridge Piers.....	30
3.5	Equivalent System Properties at Performance Limit States	31
3.5.1	Limit State System Displacement	31
3.5.2	Equivalent Limit State System Damping	33
3.5.3	Effective Limit State Periods	34
3.5.3.1	RC Bridges	34
3.5.3.2	RCFST Bridges	36
3.6	Performance Level Estimation.....	39
	CHAPTER 4.....	41
	4. ASSESSMENT APPLICATION of the CASE STUDY BRIDGES	41
4.1	Introduction.....	41
4.2	General Information about the Bridges.....	41

4.3	Equivalent System Properties of the Bridges.....	46
4.4	Alaska Earthquake Scenario and DDBA Estimations	61
	4.4.1 Earthquake Scenario.....	61
	4.4.1.1 Location-specific ground motion hazard	63
	4.4.2 DDBA Estimations.....	68
4.5	Incremental Dynamic Analysis.....	72
	4.5.1 Computational Model for Incremental Dynamic Analysis	74
	4.5.2 Comparison of the Results	76
4.6	Rapid Post-Earthquake Assessment Application under 2018 Anchorage Earthquake	82
4.7	Conclusion	86
4.8	Discussion and Future Research	87
	REFERENCES.....	90
	APPENDIX.....	97

LIST OF TABLES

Table 3.1 Performance Strain Limits used for RC Bridge Piers	22
Table 3.2 Performance Strain Limits Used for RCFST Bridge Piers	24
Table 4.1 Bridge configuration summary	45
Table 4.2 Column Section Properties.....	46
Table 4.3 Limit state curvature and moment values of BN0547 pier section.....	48
Table 4.4 Limit state moment and curvature values of top-hinge sections in the Piers.....	54
Table 4.5 Limit state moment and curvature values of bottom-hinge sections in the Piers.....	54
Table 4.6 Moment and curvature values for cracked section stiffness	60
Table 4.7 Equivalent system properties of the bridges	61
Table 4.8 Bridge locations, Vs30 values and spectral acceleration responses at the periods	66
Table 4.9 Elastic limit state system displacements and effective limit state system	69
Table 4.10 Inspection Priority chart under the considered earthquake scenario.....	72
Table 4.11 Earthquake records used to generate compatible accelerograms with the.....	74
Table 4.12 BN1903 Limit state displacement demands from the matched records.....	79
Table 4.13 Mean and Standard deviation for ratio $S_d(T_{eff})/\Delta_{sys}(DDBA)$	82
Table 4.14 Intensity measure outputs and epicentral distances	84

LIST OF FIGURES

Figure 1.1 Alaska 2018 Seismicity (“Alaska Earthquake Center” 2019)	2
Figure 2.1 Fundamentals of Direct Displacement-Based Design (Priestley et al., 2007).....	6
Figure 2.2 Flow chart for direct displacement-based assessment (Sadan et al., 2013).....	8
Figure 2.3 Example of PGA evaluation through adaptive inverse capacity spectrum method (Cardone, 2014).....	11
Figure 2.4 ShakeMap Ground motion interpolation scheme (Worden & Wald, 2016).....	13
Figure 3.1 An example of force-displacement relations for ductile structures	20
Figure 3.2 A typical RCFST - Cap beam connection (Elmer Marx, personal correspondence) .	23
Figure 3.3 Idealized moment-curvature distribution: (a) single bending case, (b) double bending case	25
Figure 3.4 Equivalent cantilever model for fixed-head RCFST shafts Aguirre (2017).....	28
Figure 3.5 Possible inelastic displacement shapes for continuous bridges with rigid superstructure and no abutment restraint: (a) rigid superstructure, plan view, (b) rigid superstructure with rotation, plan view Kowalsky (2002)	32
Figure 3.6 Secant stiffness determination for a limit state: (a) piers with same deformation capacities (b) piers with different deformation capacities.....	36
Figure 3.7 Definition of the equivalent elastic limit state demand	40
Figure 4.1 Satellite view of the bridge locations in Alaska (Google Earth, 2019)	43
Figure 4.2 General layout of RC bridges	44
Figure 4.3 General layout of RCFST bridges	44
Figure 4.4 Elevation view of BN0547	47
Figure 4.5 Simplified bridge geometry for BN0547.....	47

Figure 4.6 Moment-curvature response of BN0547 pier section.....	48
Figure 4.7 Elevation view of BN0610	53
Figure 4.8 Simplified bridge geometry for BN0610.....	53
Figure 4.9 Intensity overlay of the earthquake (Google Earth, 2019)	63
Figure 4.10 Response Spectrum Shape (FEMA 450, 2003).....	65
Figure 4.11 Acceleration response spectrum at each bridge site	67
Figure 4.12 Displacement response spectrum at each bridge site.....	67
Figure 4.13 Yield performance level	70
Figure 4.14 Serviceability performance level	70
Figure 4.15 Damage-control performance level	71
Figure 4.16 Modified Takeda hysteresis rule for RUAUMOKO analyses (Carr, 2017).....	75
Figure 4.17 Examples of multi-column bent models for RUAMOKO: (a) RC bent (b) RCFST.....	76
Figure 4.18 Comparison of IDA and DDBA at yield performance level	78
Figure 4.19 Comparison of IDA and DDBA at serviceability performance level.....	78
Figure 4.20 Comparison of IDA and DDBA at damage-control performance level	79
Figure 4.21 Spectral displacement responses of the seven records matched to BN1903 hazard.....	80
Figure 4.22 $S_d(T_{eff})/\Delta_{sys}$ (DDBA) ratios for Yield, Serviceability and Damage-Control performance limit states	81
Figure 4.23 Intensity overlay of Anchorage earthquake (Google Earth, 2019).....	84
Figure 4.24 Four-point acceleration response spectrum	85
Figure 4.25 Four-point displacement response spectrum	85
Figure 4.26 Yield performance level under 2018 Anchorage earthquake	86

CHAPTER 1

1. INTRODUCTION

1.1 Motivation

Alaska (AK) is one of the most seismically active places on Earth. Eleven percent of the world's earthquakes have been located in this region since instrumental seismicity monitoring was initiated (Koehler and Carver, 2018). Large earthquakes are also common in the area as five of the twenty largest earthquakes occurred in AK (USGS, 2019). During the last five years, 31 $M \geq 6$ and 4 $M \geq 7$ earthquakes struck this region ("Alaska Earthquake Center", 2019). Figure 1.1 shows the earthquakes recorded in AK in 2018 to illustrate the seismic activity in the region. Moreover, it is reported that magnitude 6 and 7 earthquakes can occur nearly anywhere in Alaska ("Alaska Earthquake Center", 2019). The potential seismicity of the region signifies that structures situated in this area may experience various levels of seismic hazard that could be sufficiently strong to cause structural damage during their lifetime.

Highway bridges are of great importance to maintain the transportation network between cities as they pass over rivers or valleys. Disruption of a highway network due to an earthquake may result in delay of emergency aids to the affected zones. Rapid reporting about seismic performance of bridges would assist emergency managers in assessing the impacts of the earthquake and allow them to direct aid operations in a more practical manner. Rapid damage estimation of bridges could also be useful for department of transportations (DOT) to prioritize their post-earthquake field inspections. Furthermore, having an idea about bridge damage levels before conducting visual inspections would provide efficiency for inspection teams to prioritize bridge retrofiting.

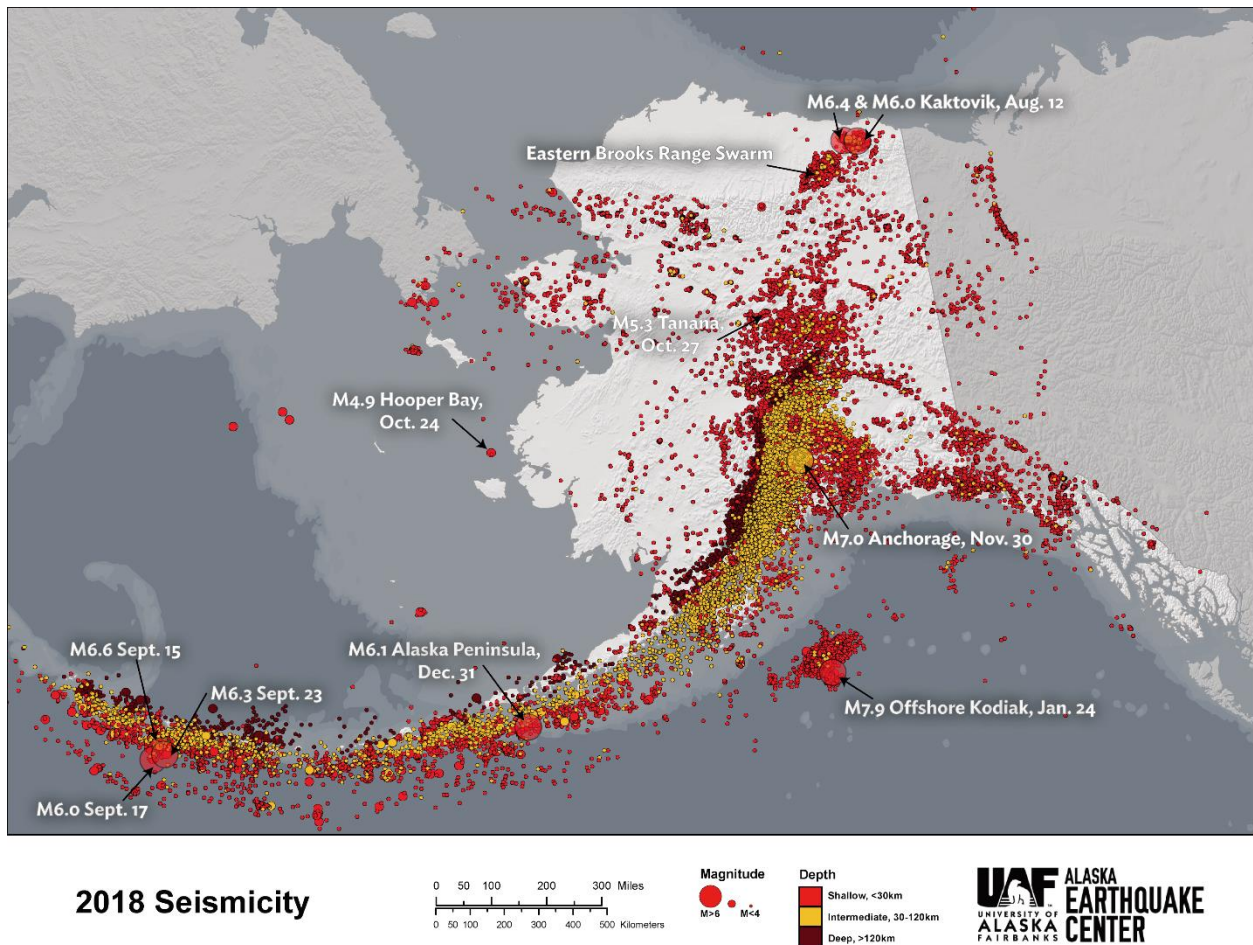


Figure 1.1 Alaska 2018 Seismicity (“Alaska Earthquake Center” 2019)

The amount of information available about the bridge and the hazard essentially forms the basis of a post-earthquake assessment strategy. For example, HAZUS (by FEMA) bases its assessment strategy on limited information about the bridge and the hazard. This methodology provides damage functions for standardized bridge typologies at a period of 1 second. Such an approach may be preferable to use for the cases where limited bridge information is available, or where there is a large population of bridges that would be difficult to characterize deformation capacities individually. However, when accurate bridge-specific information is available for a small set of bridges, a more specific post-earthquake assessment strategy can be implemented

rather than generalizing bridge deformation capacities and limiting the seismic demand at a single period, as done in the HAZUS approach.

The direct displacement based-design (DDBD) method developed by Priestley et al. (2007) aims to design structures to achieve a prescribed target displacement under a design level hazard. The DDBD methodology represents system performance by displacements and corresponding strengths at limit states of interest. Such an attribute provides an opportunity to make use of the method for assessment purposes. By identifying limit states for a particular bridge while also having the likely deformation demand at the structure site, it may be possible to estimate the performance level of the bridge for a given hazard. The rapid assessment approach that will be described in this thesis builds its strategy on the following. For an existing group of bridges where details are available, limit state displacements and corresponding strengths are identified at different performance levels based upon the DDBD approach. The identified performance levels of the bridges are then examined to assess whether they are achieved under the hazard defined at the bridge site. The ShakeMap tool (by USGS) is adopted in this study to define site-specific seismic demand at the bridge sites for either a scenario or a real earthquake.

1.2 Organization

Chapter 2 first starts with an overview of DDBD methodology followed by past research regarding development of DDBA for bridge structures. Then the second part describes the ShakeMap tool along with its feature of generation of scenario earthquake and gives an overview of a recent study used ShakeMap scenario earthquakes for bridge assessment. Finally, HAZUS post-earthquake methodology for bridge structures is covered. The main objective and specific goals of the research given the literature reviewed are described at the last section of chapter 2.

Chapter 3 presents considered performance limit states with their corresponding damage levels, the DDBA procedure for construction of equivalent SDOF properties at a performance level of interest, and performance level estimation of the bridge under a given hazard.

Chapter 4 contains assessment applications of the case study bridges. Comparison of DDBA estimations against the results of nonlinear time history analyses are presented for an earthquake scenario generated from ShakeMap. Rapid seismic assessment of bridges by the DDBA under a ShakeMap scenario of a real event is described, and assessment application of the three case study bridges is shown under the ShakeMap of the 2018 Anchorage Earthquake. Moreover, conclusion of the study, recommendations on possible future research are provided.

CHAPTER 2

2. LITERATURE REVIEW

2.1. Introduction

Generally, post-earthquake assessment strategies lack bridge-specific information as they target the bridges about which limited information is known, or they try to handle damage estimation of a large bridge inventory. Uncertainty about bridge details often leads to coarse limit state definitions. However, for a small set of bridges with more detailed metadata, limit state displacements can be more accurately estimated. The deformation limit states can then be used for rapid seismic performance estimation of bridges once the seismic demand is defined at the bridge sites. In this regard, the literature review below first presents the direct displacement-based design (DDBD) strategy and past research pertaining to implementation of DDBD for seismic assessment of existing bridges. The second part covers site-specific hazard definition for rapid seismic assessment, and lastly, the third part gives information about a current post earthquake bridge damage assessment module along with its limitations regarding limit state definition and seismic demand parameters.

2.2. Fundamentals of Direct Displacement-Based Design

The Direct displacement-based design (DDBD) methodology developed by Priestley et al.(2007) aims to design structures for a desired displacement (defined by drift ratio, ductility level or a critical strain) under a given seismic hazard. Figure 2.1 illustrates the DDBD fundamentals. The approach represents multi degree of freedom (MDOF) structures as equivalent single degree of freedom (SDOF) systems (Figure 2.1a). The Lateral force-displacement response of the equivalent SDOF system is characterized by the secant stiffness, K_e , and equivalent viscous

damping, ξ_e , at the prescribed design displacement, Δ_d (Figure 2.1b). Upon determination of the yield displacement of the equivalent system, Δ_y , the corresponding displacement ductility may be obtained. This is followed by calculation of the equivalent damping (Figure 2.1c). The effective period, T_e , is obtained from the displacement spectra that is consistent with the effective damping of the system as shown in Figure 2.1(d).

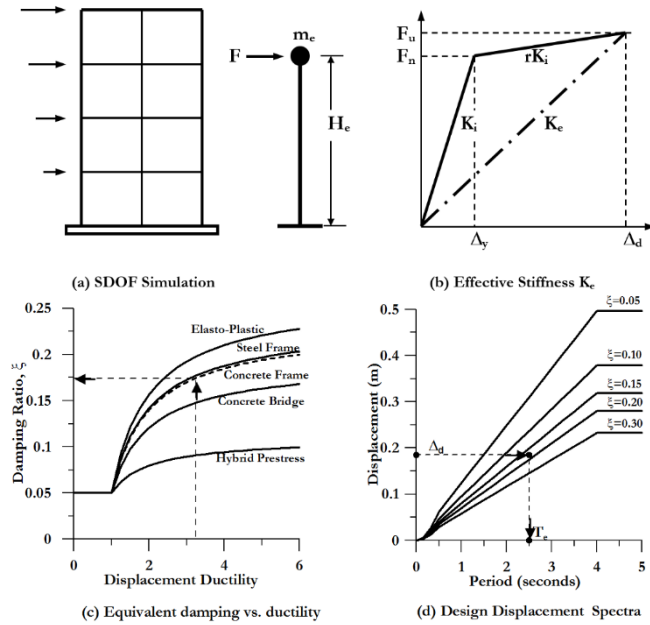


Figure 2.1 Fundamentals of Direct Displacement-Based Design (Priestley et al., 2007)

Then T_e is converted into an effective stiffness K_e using the following expression.

$$K_e = \frac{4\pi^2 m_e}{T_e^2} \quad (2.1)$$

Where m_e is the effective mass of the structure that participates in the first inelastic mode of vibration. Finally, the design base shear, V_b , is calculated by multiplying the effective stiffness by the design displacement.

2.3. Direct Displacement-Based Assessment of Bridges

Extending the DDBD procedure to assessment, Priestley et al. (2007) proposed a direct displacement-based assessment (DDBA) procedure for SDOF structures. The steps for DDDBA of SDOF structures from Priestley et al. (2007) can be summarized as follows:

1. Calculate effective mass, m_e
2. Identify the force-displacement response of the structure up to the displacement level of interest, Δ_{cap} , and calculate the secant assessment stiffness, K_A , at the displacement capacity, Δ_{cap} .
3. Calculate effective assessment period, T_A ,
4. Determine the ductility demand, μ ,
5. Determine the effective damping, ξ_a ,
6. Find spectral reduction factor, R_ξ , and convert Δ_{cap} into equivalent elastic displacement Δ_{cap-el} .
7. Determine the demand, Δ_{dem-el} , from a given elastic displacement spectra and assess the structure by the ratio of $\Delta_{cap-el} / \Delta_{dem-el}$.

In addition to DDDBA of SDOF structures, Sadan et al. (2013) extends the DDBD design methodology developed for bridge structures by Priestley et al. (2007) to a DDDBA procedure for multi-span RC bridges with single-column piers. The proposed procedure starts by collecting bridge details (Step 1) as a pre-analysis phase. It is then followed by generating the displacement shape (Step 2) of the bridge to idealize the bridge with equivalent SDOF properties (Step 3). Finally, seismic assessment of the bridge (Step 4) is conducted. A flow chart of the procedure with sub steps is given in Figure 2.2.

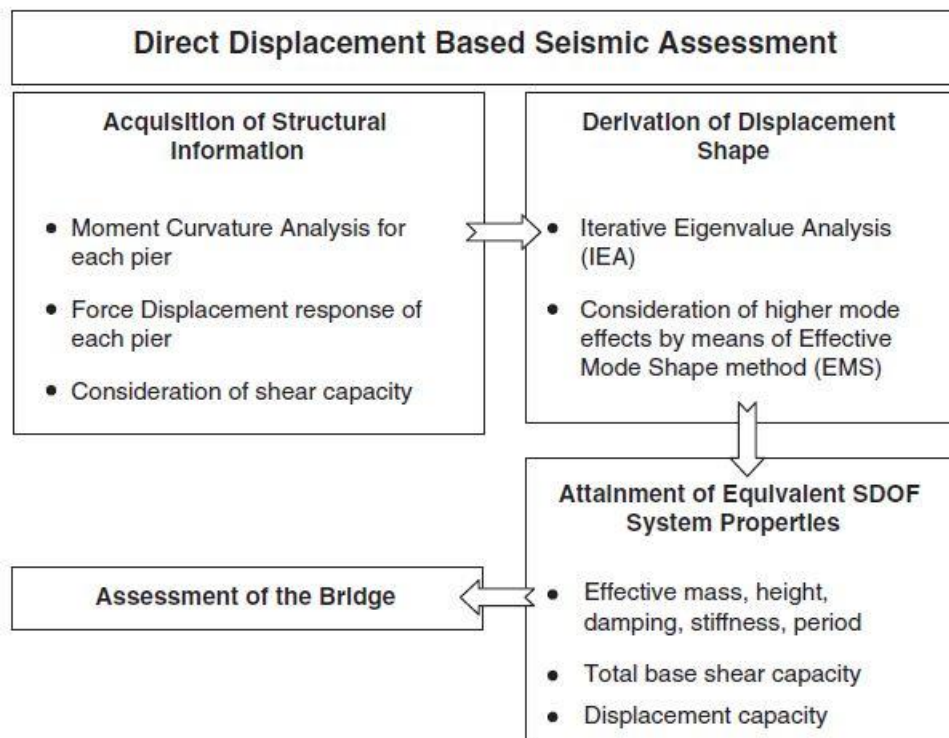


Figure 2.2 Flow chart for direct displacement-based assessment (Sadan et al., 2013)

Step 1 refers to obtaining structural information (material and section properties) to determine seismic vulnerability of bridge piers. The next step evaluates which pier of the bridge will first reach its prescribed limit, determined in Step (1). The critical pier that reaches its limit can be determined without any iteration in the longitudinal direction. To obtain the displaced shape for the transverse direction, the study adopts iterative eigen value analysis (IEA, Kowalsky, 2002). For highly irregular bridges whose mass participation is less than 65-70 % in the transverse direction, the authors suggest modifying the displaced shape using the effective mode shape method (EMS, Kowalsky, 2002) in addition to IEA in order to account for the impact of higher modes on the bridge response. Displacement and corresponding strength capacity are calculated from limit state displacement profile of the bridge, obtained in step (2). The structure is then

idealized with equivalent SDOF properties (Sub steps of step (3) in Figure 1) similar to DDBD. The last step is to find the equivalent elastic displacement capacity using a damping scaling factor (DSF). As a result, DDBA of the bridge is defined with a ratio of elastic displacement capacity to the corresponding elastic displacement demand under a given seismic hazard.

The proposed method was applied to 13 hypothetically generated multi-span reinforced concrete bridges with single-column piers, 9 with bearing deck connection and 4 with monolithic deck connections. Damage assessment of the bridges was done for a single pier limit state, and it was assumed that abutments remain elastic. Response spectrum analysis (RSA) of the bridges was also conducted as a force-based assessment to compare RSA results with the results from DDBA. Both DDBA and RSA of the bridges were done under a design level hazard. Accuracy of the results was investigated with incremental dynamic analysis (IDA) of 5 spectrally matched records. Based on the results, DDBA damage estimations were reasonably close to the results of IDA with 9 bridges less than 5 % error, 3 bridges at 5-10 % error and 1 bridge at 15-20 % error. RSA damage estimations were very different from results of IDA, with only 2 bridges at less than 5% error, 1 bridge at 5-10 % error, 2 bridges at 10-15 %, 1 bridge at 15-20 % and 7 bridges at more than 20% error.

Cardone (2014) proposed a DDBA procedure that identifies the level of bridge damage in terms of peak ground acceleration (PGA) for a given hazard. Furthermore, the procedure accounts for damage levels for other bridge elements such as abutments, bearings, shear keys, and piers. Four critical displacement limits were defined for each component at damage levels named as slight, moderate, severe and collapse prevention. After defining displacement limit states for each component, a displacement profile corresponding to attainment of a damage level in a bridge element was obtained. Displacement adaptive pushover analysis (DAP, ANTONIOU and PINHO,

2004), effective modal analysis (EMS, Kowalsky, 2002), individual pier approach (IPM) and rigid deck model approach (RDM) were used as example methods for obtaining damage state displacement profiles. After determining the critical displacement profile at each defined damage state, the procedure uses DDBD equations given by Priestley et al. (2007) to idealize structures at each damage state with corresponding displacement, acceleration, equivalent mass and damping, effective period and stiffness. The final step is to find critical PGAs associated with each damage state. The procedure adopts the inverse adaptive capacity spectrum (IACSM) method proposed by Cardone et al. (2011) to obtain critical PGA values at each damage state. IACSM uses 5% normalized demand spectrum (NDS) where all spectral accelerations are normalized to the PGA of the given seismic hazard. The normalized spectral acceleration demand for a performance level ($S_{a1,PL}$) is obtained from the over-damped NDS reduced by a damping reduction factor to the damping level of the PL. The ratio of spectral acceleration of the PL, $S_{a,PL}$, to the $S_{a1,PL}$ is used to evaluate to the PGA required for the bridge to reach that PL. General PGA evaluation of the method is illustrated in Figure 2.3.

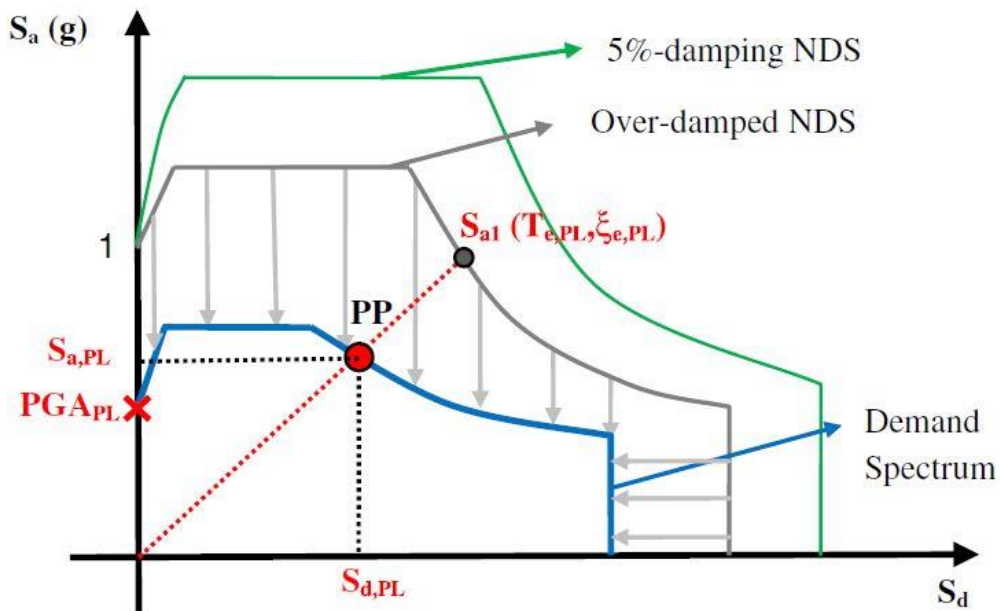


Figure 2.3 Example of PGA evaluation through adaptive inverse capacity spectrum method

(Cardone, 2014)

The proposed DDBA procedure was applied by using prescribed displacement profiles, DAP, EMA, IPM and RDM to 10 different bridge configurations under a given seismic hazard. Example bridges vary in terms of deck types, pier heights, and bearing types. Suitability of DAP, EMA, IPM and RDM methods was examined against non-linear response history analysis (NLRHA) of the bridges using 7 spectrum compatible records. Based on the results it was observed that the DAP method gives the closest results with that of NLRHA. EMA provides satisfactorily good results for the bridges with fixed bearings, but for the bridges with neoprene pads accuracy of EMA against DAP and NLRHA reduces. IPM and RDM give acceptable results for the bridges with simply supported internal movement decks and for the bridges with rigid continuous decks, respectively.

As summarized from the DDBA studies above, performance estimation of the bridges can be conducted under a given hazard. As far as damage assessment of a bridge is concerned due to an earthquake, seismic demand at the bridge site needs to be known so that the performance of the bridge can be evaluated. Site-specific hazards can be defined using empirical relations mostly governed by magnitude and distance parameters, however, the ShakeMap tool makes it possible to rapidly define more realistic site-specific hazards. The next section presents information about ShakeMap as a means for hazard definition for rapid assessment.

2.4. Hazard Definition for Rapid Seismic Assessment

2.4.1 Shake Map

Traditionally, magnitude and epicentral distance have been used as impact measure in the wake of a significant earthquake (Worden & Wald, 2016). However, it has been realized from past earthquakes that magnitude and epicenter information are not adequate for defining earthquake impact over the region. For instance, damage investigations after the 1971 San Fernando Earthquake (M6.7) showed that the most damaged area was 15 km away from the epicenter (Worden & Wald, 2016). For the 1999 Kocaeli Earthquake (M7.4), earthquake damage was more predominant at the east-west side of the causative fault than that of north-south side (ERDIK, 2001). Severity of the damage from 1995 Kobe, Japan (M6.9) earthquake was identified by the central government in Tokyo hours after occurrence of the event Yamakawa (1998). Therefore, this late notice of the earthquake impact caused delay in response to the earthquake. Recognizing the complex nature of earthquakes, more information about an earthquake is needed to facilitate rapid earthquake response actions. Hence, the ShakeMap tool has been developed by United States of Geological Survey (USGS) for the purpose of increasing accuracy of earthquake loss estimation. This tool provides ground shaking levels in the region after a very short time of an earthquake.

ShakeMap releases extensive information about an earthquake shortly after the event but the main products of the tool for earthquake engineering applications are interpolated intensity measure types (IMTs), PGA, Peak Ground Velocity (PGV) and Spectral Accelerations (SA) at 0.3, 1.0 and 3.0seconds, in a finely-sampled grid pattern (nominally 1km spacing) over the impacted region. Each point is represented with latitude and longitude pairs and corresponding amplitude of IMTs. There are two types of input data used by ShakeMap for generation of interpolated IMTs. IMTs from ground motion stations are called “primary observations”, and IMTs converted from individual intensity reports (DYFI, USGS) using ground motion intensity conversion equations (GMICE), are called “converted observations” (Wald, et al. 1999b, Worden et al., 2012). Peak horizontal IMTs from each station and IMTs from converted observations are collected for input to ShakeMap. The key steps taken by ShakeMap in data processing are schematized in Figure 2.4 and a brief summary about each step is given in the following.

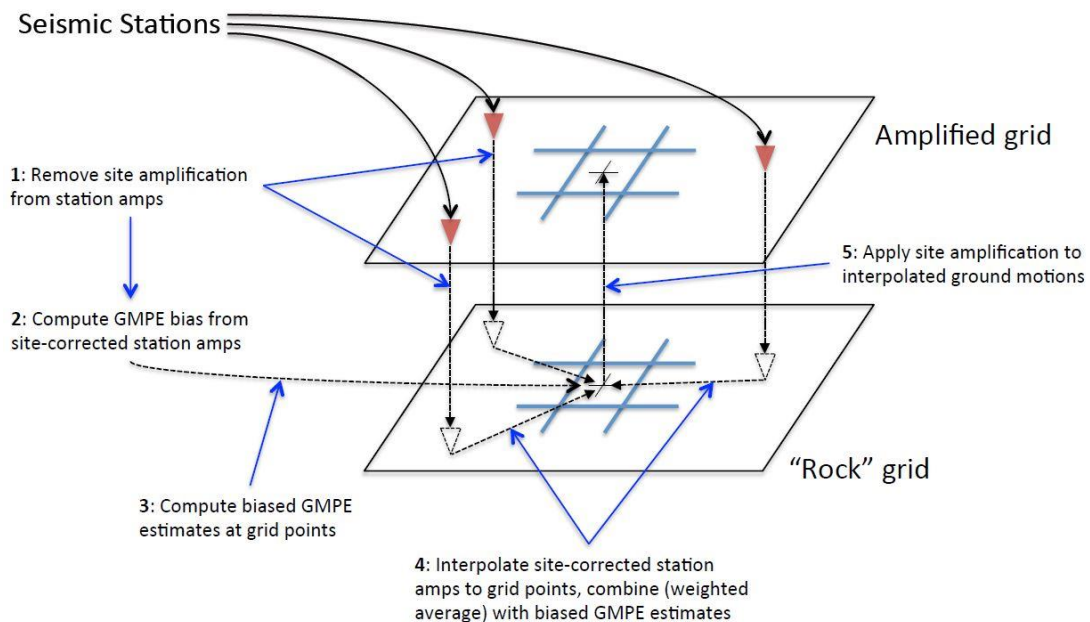


Figure 2.4 ShakeMap Ground motion interpolation scheme (Worden & Wald, 2016)

First, ShakeMap removes Vs30 site-amplifications from all inputted IMTs such that the input may be expressed at the common base of Vs30 rock level. The second step starts by making estimations of IMTs through a selected GMPE at direct and converted observation points. Then a bias correction process is applied in order to minimize the misfit between GMPE estimations and observational data by adjusting magnitude parameters of the selected GMPE. In the third and fourth step, IMTs are interpolated between pre-defined grid points combining observed data and bias adjusted GMPE at the rock level. The last step is applying Vs30 amplifications to IMTs at each point and bringing all of them to the ground level. More information about data processing and interpolation process of IMTs can be found in Worden & Wald (2016) and Worden et al. (2010), respectively.

2.4.2 Shake Map Scenario Methodology

Federal government or local agencies would like to measure their post-earthquake response capabilities under various levels of earthquakes so that they can be better prepared when a real event occurs. In addition to the use of ShakeMap ground motion estimates for a real event, the tool is also employed for pre-earthquake planning purposes through hypothetical earthquake scenarios. A scenario event is a representation of a historical earthquake or a potential earthquake based on active faults in the region. Any scenario event can be run when magnitude, location and fault geometry with the rupture distance are specified to ShakeMap. Output types do not change from real to scenario events, thus earthquake loss estimation or inspection prioritization of structures can be easily determined from scenario events just as if the events were real. For a scenario event, Vs30 soil amplified IMTs are estimated by a selected GMPE over a region. Directivity effects can also be added to IMTs if the direction of rupture would like to be considered. However, resulting shaking distribution from a scenario event is not as complex as a real event since ShakeMap

scenario methodology does not account for all the expected variabilities from a real event such as 2D and 3D wave propagation, and basin-edge effects. Nevertheless, the ShakeMap scenario tool is useful as it provides an opportunity for emergency response planners, and engineers to assess the impact of various levels of earthquake hazards over a region. While it is possible to generate any desired earthquake scenario for a particular region as long as the above-mentioned parameters are provided, it would be more instructive to refer earthquake scenarios that represent historical or potential future earthquakes in the region. For this purpose, USGS provides a list of scenario catalogs (“USGS Scenario Catalogs”, 2019) that contain historical earthquake scenarios and scenario earthquakes for a specific state. Generation of scenario earthquakes for a specific state is based on potential future earthquakes evaluated by disaggregating probabilistic seismic hazard maps. Seismic hazard disaggregation analysis for a specific region provides individual earthquakes that form the hazard in the region with their own magnitudes, rupture distances and contributions to the hazard. Such an analysis helps to prioritize earthquake scenarios for the region.

Biasi et al. (2016) conducted damage estimation of 1831 Nevada highway bridges under deterministic and probabilistic seismic hazards. 112 deterministic earthquake scenarios were created by ShakeMap based on active faults in the region. ShakeCast, the USGS loss estimation tool, was used to estimate bridge damage under the scenario earthquakes. ShakeCast automatically retrieves intensity measures from ShakeMap at each pre-defined bridge location. Then damage estimation of each bridge is defined by log-normal bridge fragility functions, which give probability of exceedance of a specific damage level under a given intensity measure. The bridges were classified according to HAZUS (2011), which considers bridges based on their seismic design, number of spans, structure, pier, abutment and span types. Bridges built before 1983 are considered to be non-seismic design. One second spectral accelerations [SA (1)] from the scenarios

were used as intensity measure inputs into ShakeCast since HAZUS-MH (2011) bridge damage functions are defined for one second bridge period. However, damage capacities were not adopted from HAZUS (2011) due to the following reasons. First, it was realized that HAZUS suggests same bridge capacity values for continuous box girder bridges irrespective of construction year. Second, proposed bridge capacities from HAZUS were found to be substantially higher for each damage level when those capacities compared with design capacities of the case study bridges. For these reasons, bridge capacities were revised at three damage levels, namely moderate, extensive and complete. Eight non-seismic concrete continuous box girder bridges with multiple girders were observed to experience different level of damage ranging from moderate to complete under seven deterministic scenario earthquakes out of 112 that were run through ShakeMap. For probabilistic assessment, the 2014 USGS National Seismic Hazard Maps (NSHM) were used. The purpose was to obtain return periods of the scenario earthquakes that cause extensive damages by entering seismic hazard curves with [SA (1)] and reading corresponding return periods. The resulting return periods were compared to the 1000-year return period, which is considered as the return period of design level earthquakes by AASHTO. If the return period is less than the 1000-year, it was considered that the bridge was vulnerable against the design level earthquake. Therefore, strengthening was suggested for those bridges suffered from the earthquakes whose probability of occurrence was bigger than 7% in 75 years (1,000-year return period).

The next section summarizes bridge damage estimation strategy by HAZUS that currently employs intensity measure outputs provided by ShakeMap.

2.5 HAZUS Bridge Damage Estimation

HAZUS-MH (2011) is a program of FEMA that estimates loss out of multiple hazards including flood, windstorm, tsunami, and earthquake amongst others. Bridge physical damage

estimation is a part of the HAZUS (2011) earthquake loss estimation module. The module considers 28 different bridge types which are classified based on the characteristics of the National Bridge Inventory (NBI, 2010). Damage parameters for each bridge type are standardized employing fragility curves developed by Basoz & Mander (1999). Definition of limit states by Basoz & Mander (1999) are drift-based and the vulnerability of the bridge is represented by the vulnerability of the columns. Fragility parameters at different damage states are provided depending upon seismic design, number of spans, structure type (concrete, steel, etc.), pier type, abutment and bearing types of the bridge. Fragility parameters can then be modified in order to account for skewness of the bridge and the 3D response of the bridge. Log-normal fragility functions are used to estimate probability of exceedance of each damage state using 1 second peak spectral acceleration SA[1s] intensity measure.

Traditional ways of defining intensity measures at the structure sites in HAZUS would be using empirical relations which are mostly governed by the epicenter and magnitude of the earthquake (Worden & Wald, 2016). With the advent of ShakeMap, HAZUS can be driven using intensity measures provided by ShakeMap for an event. ShakeMap generates HAZUS intensity measures files that can be inputted into HAZUS software for events that are larger than magnitude 4.5 (Worden & Wald, 2016).

2.6 Study Plan and Objectives

The major challenge of seismic assessment of existing structures is that it requires examination of the seismic behavior at various performance levels. Each performance level corresponds to a different level of damage and hence, for a given bridge, the structural behavior needs to be identified when a bridge element reaches the specified performance limit. Sadan et. al. (2013) and Cardone (2014) verified that under a selected mechanism, performance limit state

identification provides satisfactorily good results following a direct displacement-based methodology.

Given the promise of DDBA studies from past research, this study strives to implement a rapid post-earthquake assessment strategy for Alaska Highway bridges. The ShakeMap tool will be utilized to create seismic demands at the bridge sites. This research aims at achieving the following objectives:

- 1) Identify limit state displacements of a set of bridges from Alaska at different performance levels using a direct displacement-based methodology.
- 2) Estimate damage levels of these bridges by the applied methodology under an earthquake scenario that is processed by ShakeMap.
- 3) Check the accuracy of the applied direct displacement-based methodology against time history analyses.
- 4) Propose how ShakeMap intensity measures can be employed to estimate quick seismic performance estimation.

CHAPTER 3

3. APPLIED DIRECT DISPLACEMENT-BASED APPROACH

3.1 Introduction

This chapter presents the applied direct displacement-based approach to identify equivalent system properties of the bridges considered in this study from Alaska. Prior to discussing the methodology, limitations and assumptions that shape it are outlined first. In this study, limit state displacements of 3 reinforced concrete (RC) and 4 reinforced concrete filled steel tube (RCFST) continuous bridges from Alaska were identified in the transverse direction. Rigid superstructure and rigid cap beams were assumed, and abutment restraints were ignored. Bridge vulnerability was defined only by column damage. Flexural mode of failure defined by column plastic hinges were considered for identifying limit state displacements. Bridge column failures due to geometric nonlinearity e.g., $P-\Delta$ effect, interaction of shear strength with flexural response were not considered. Based on the assumptions and the limitations discussed above, the methodology is described in the following sections.

3.2 Performance Limit States

A well-designed ductile structure will pass through several limit states on its way to the ultimate displacement capacity. Figure 3.1 illustrates a force-deformation relationship for ductile structures. Cracking and first-yield limit states are not significant for structures located in high seismic regions. Instead, the equivalent yield point can be considered as the first important limit state for the structure. In this study, yield, serviceability and damage control performance limit states were considered for limit state displacement evaluation of the case study bridges.

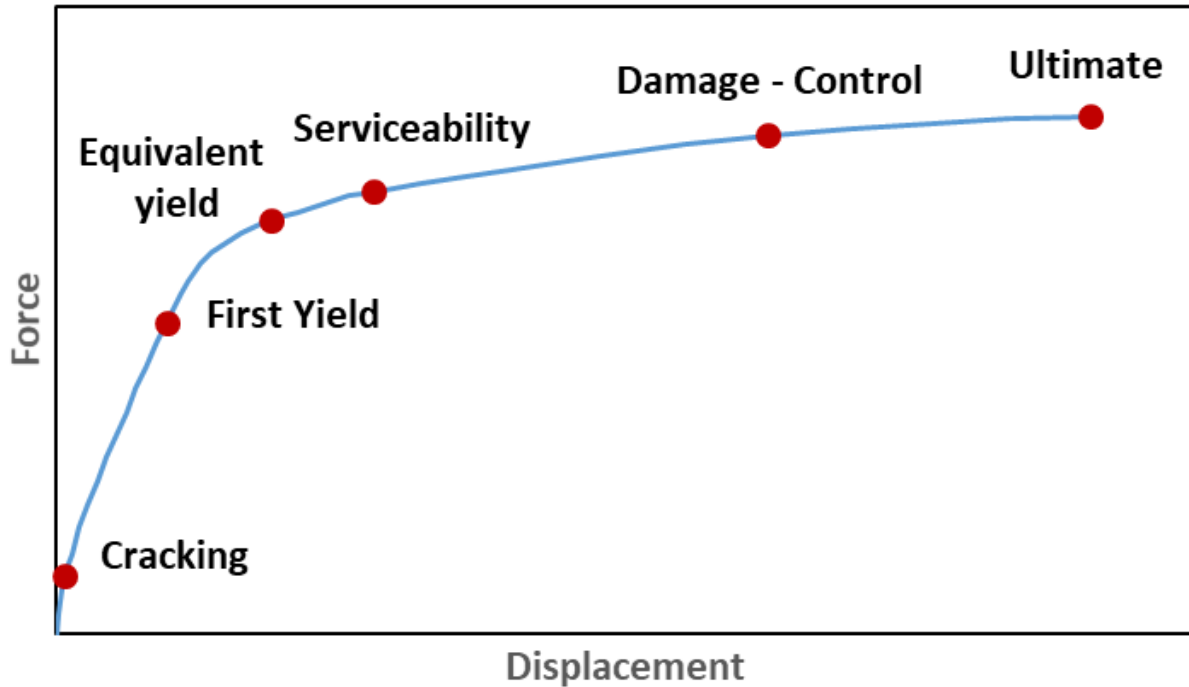


Figure 3.1 An example of force-displacement relations for ductile structures

The yield limit state is defined by visible small cracks at the surface of the pier. The damage at this level of response is considered minor, and the piers do not need more than cosmetic repair. The serviceability limit state is consistent with cover concrete crushing and residual crack widths exceeding 1mm. Achievement of this limit state requires minor repair, but the repair should not affect operability of the bridge. The damage-control limit state represents the point beyond which repair becomes costly, possibly exceeding cost of replacement of the bridge (or its components). Longitudinal bar buckling and significant damage to the core concrete (Goodnight et al., 2016) are traditional examples representing this limit state.

In addition to qualitative definitions of these limit states, there have been numerous efforts made in performance-based earthquake engineering (PBEE) for numerical quantification of these performance levels. It is recognized that performance level of bridge piers can be evaluated more accurately with material strains rather than setting fixed drift limits (Priestley et al., 2007). Thus,

pier limit state displacements were determined based on strain limits at yield, serviceability and damage-control limit states.

3.3 Critical Curvature Evaluation at Performance Limit States

Moment-curvature analysis of bridge piers is conducted using CUMBIA (Montejo and Kowalsky, 2007) to obtain critical curvatures associated with the limiting concrete compression and the steel tension strains for a limit state of interest. Critical curvature values at each limit state are then translated into displacements (see section 3.4.1). The following sections describes input parameters used for obtaining the moment-curvature response of the piers.

3.3.1 Material Strength

Using lower-bound material strengths is a common practice for assessing structures under gravity loading. However, for seismic assessment, expected properties are utilized. Therefore, the expected material strength factors proposed by Priestley et al. (2007) for both concrete and steel were adopted.

$$\text{Concrete: } f'_{ce} = 1.3f'_c \quad (3.1a)$$

$$\text{Steel: } f_{ye} = 1.1f_y \quad (3.2a)$$

3.3.2 Strain Limits

3.3.2.1 RC Bridge Piers

Limiting concrete and steel strains for each performance level are given in Table 3.1. Yield limit strains are defined by the yield strain of the extreme rebar, \mathcal{E}_y , and a 0.002 concrete cover strain. Serviceability limit strains and damage control tension strains were taken from the study of Goodnight et al. (2016). Ultimate confined concrete compression strains proposed by Mander et al. (1988) were used as damage-control compression strains.

Table 3.1 Performance Strain Limits used for RC Bridge Piers

Strain	Performance Level		
	Yield	Serviceability	Damage-Control
Tension	ϵ_y	0.015	$0.03 + 700\rho_s \frac{f_{yhe}}{E_s} - 0.1 \frac{P}{f'_{ce}A_g}$
Concrete	0.002	0.004	$0.004 + 1.4 \frac{\rho_s f_{yh} \epsilon_{su}}{f'_{cc}}$

For the parameters given in Table 3.1, ρ_s is the transverse volumetric steel ratio, f_{yhe} is the expected transverse steel yield stress, f_{yh} is the transverse steel yield stress, E_s is the modulus of elasticity of steel, ϵ_{su} is the maximum reinforcement strain (taken as 0.12), f'_{cc} is the compression strength of the confined concrete, P is the axial load acting at the section centroid, A_g is the gross area of the section and f'_{ce} is the expected concrete compressive strength.

3.3.2.2 RCFST Bridge Piers

The inelastic behavior of RCFST piers are affected by the configuration of the bridge bent. If the bent contains a single-column, i.e. pinned-head RCFST shaft, the inelastic behavior is governed by the plastic hinge that develops below ground. The case in which the bent contains multi-column, i.e. fixed-head RCFST shaft, the system has the potential to develop two plastic hinges which are the top-hinge at the cap beam-column interface and the below ground hinge. However, as will be explained in the next paragraph, the inelastic behavior of an RCFST fixed-head system is controlled by the top hinge. In this research, all RCFST case study bridges examined were multi-column bent bridges, therefore the focus hereafter will only be on fixed-head RCFST shafts. The flexural stiffness distribution of an RCFST member is not uniform throughout its length because the steel tube is not extended into the cap beam. The steel tube is cut short before the cap-

beam by leaving a gap of 50 mm. Therefore, the section at the cap beam-column interface effectively corresponds to an RC section, and the section below the gap is an RCFST section.

Figure 3.2 presents a typical example of a cap beam - RCFST connection of a bridge from Alaska. The gap between pipe and adjacent member can be seen in Figure 3.2. Since flexural capacity of the RC section at the top would be significantly lower than a section in the rest of the RCFST member, the onset of plastic behavior first initiates at the cap beam-column interface. After formation of the top plastic hinge, flexural stiffness is redistributed along the member and thus the inground moment starts increasing. It was observed from an analytical study by Aguirre (2017) that when the damage-control limit state is achieved in the top plastic hinge, the inground hinge hardly experiences its yield limit state.

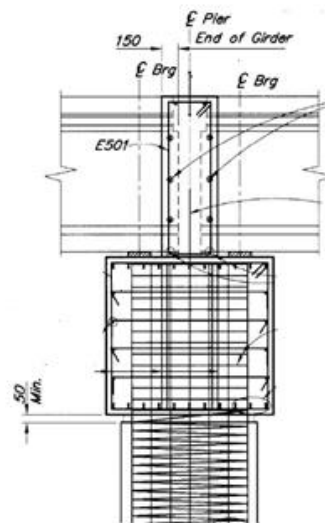


Figure 3.2 A typical RCFST - Cap beam connection (Elmer Marx, personal correspondence)

The POLA Seismic Code (2010) provides strain limits for pile top plastic hinges. In this code, strain limits are connected to earthquake return period to define the performance level. Strain limits defined for operating and contingency earthquake levels are considered as serviceability and damage control strain limits, respectively, for top plastic hinges of fixed-head RCFST sections.

Strain limits and corresponding performance levels for top hinges of RCFSTs are summarized in Table 3.2. ϵ_{sm} is the strain at peak stress of reinforcement, and 0.06 or $0.06\epsilon_{sm}$ (whichever is smaller) is used as damage-control tension strain. It should be noted that concrete strain limits in Table 3.2 are significantly higher than that of a regular RC sections at serviceability and damage-control limit states. The reason for larger concrete strain values is that the RC section in an RCFST system sustains indirect confinement by the steel pipe below and the cap beam above, while also being subjected to direct confinement from the transverse steel in the section. In order to account for this indirect confinement effect, moment-curvature analysis of the top RC section can be conducted considering 50% of confinement contribution by the steel tube in addition to transverse steel in the section (Montejo et al., 2012). CUMBIA was modified to include the partial effect of steel pipe confinement into the confinement of the concrete.

Table 3.2 Performance Strain Limits Used for RCFST Bridge Piers

Strain	Performance Level		
	Yield	Serviceability	Damage-Control
Tension	ϵ_y	0.015	$0.6\epsilon_{sm} \leq 0.06$
Concrete	0.002	0.010	0.025

3.3.3 Material Models

The Mander model (1988) was used for confined and unconfined concrete in RC sections. The King model (1986) was used for both reinforcement and pipe steel strain. The Mander model (1988) was modified to incorporate the confinement effect on the top hinge of the RCFST section (Montejo et al., 2008). For detailed information about the material models, see the CUMBIA user guide (Montejo and Kowalsky, 2007) and Montejo et al., (2008).

3.4 Deformation Limit States and Equivalent Viscous Damping of the Bridge Piers

3.4.1 Deformation Limit States

3.4.1.1 RC Bridge Piers

Having evaluated critical curvatures at the limit states, pier limit state displacements can be calculated following the plastic hinge method proposed by Priestley et al. (2007). The method uses an idealized curvature distribution to estimate the pier displacement for a given curvature. Figure 3.3 illustrates idealized moment and curvature distribution for two different types of piers.

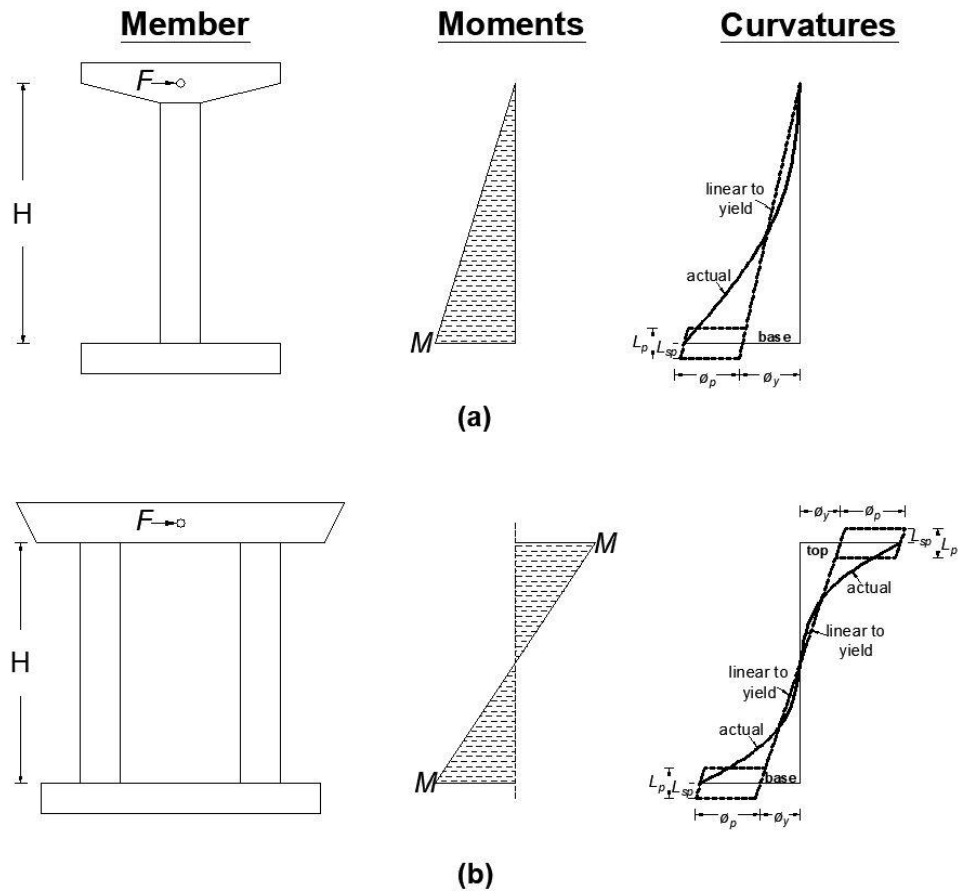


Figure 3.3 Idealized moment-curvature distribution: (a) single bending case, (b) double bending case

In case of a fully fixed bridge pier to the ground and no intermediate link, yield displacement of the pier can be calculated from Eq. (3.3) or (3.4) depending upon the fixity condition at the top of the column. Eq. (3.3) and (3.4) are employed for pin (Figure 3.3a) and fixed (Figure 3.3b) top connections, respectively.

$$\Delta_y = \frac{\phi_y (H + L_{sp})^2}{3} \quad (3.3)$$

$$\Delta_y = \frac{\phi_y (H + 2L_{sp})^2}{6} \quad (3.4)$$

Where ϕ_y is the yield curvature, H is the column height. Strain penetration length, L_{sp} , is introduced in order to account for anchorage deformation at plastic hinge regions. The strain penetration length can be obtained as follows:

$$L_{sp} = 0.022 f_{yre} d_{bl} \quad (3.5)$$

f_{yre} is the expected yield stress of longitudinal rebar and d_{bl} is the longitudinal rebar diameter. Serviceability and damage-control limit state displacements where the pier exhibits inelastic behavior can be calculated with the following expression:

$$\Delta_{ls} = \Delta_y + (\phi_{LS} - \phi_y) L_p H \quad (3.6)$$

ϕ_{LS} is the limit state curvature, and L_p is the plastic hinge length. L_p can be calculated as follows:

$$L_p = kL_c + L_{sp} \geq 2L_{sp} \quad (3.7)$$

$$k = 0.2 \left(\frac{f_{uer}}{f_{yre}} - 1 \right) \leq 0.08 \quad (3.7a)$$

In Eq. (3.7), L_c is defined as the clear length that is measured from the center of the plastic hinge length to the point of contra-flexure where flexural moment is zero in the member. Thus, for a pier in single bending $L_c = H$ and $L_c = H/2$ for double bending.

3.4.1.2 RCFST Bridge Piers

The equivalent cantilever plastic hinge approach proposed by Aguirre (2017) was utilized to estimate limit state displacements for RCFST bridge piers. When a fixed-head RCFST is considered, as illustrated in Figure 3.4, the method represents the RCFST system with an equivalent length between maximum moment locations. The proposed model also includes the effect of soil stiffness on the global response of an RCFST system. In this study, all RCFST case study bridges were assumed to be embedded in medium-sand soil. Thus, only expressions for sand from the model is provided herein. More details about the model can be found in Aguirre (2017).

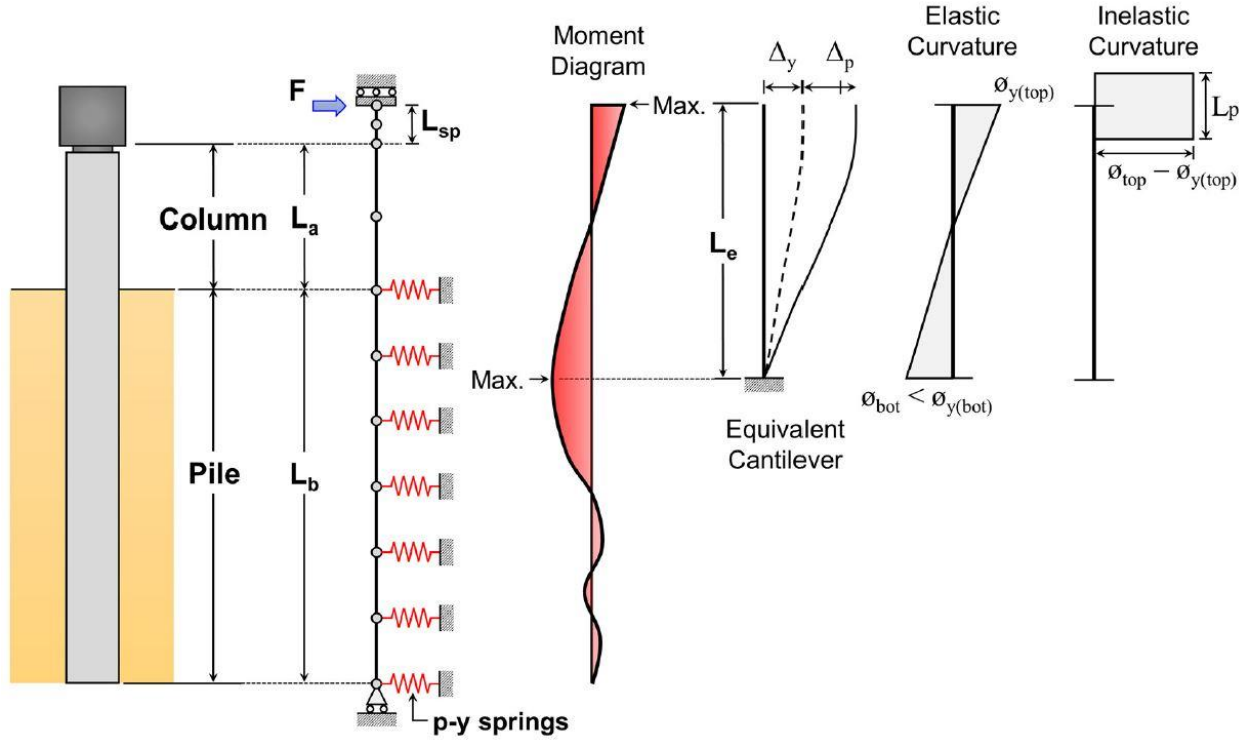


Figure 3.4 Equivalent cantilever model for fixed-head RCFST shafts Aguirre (2017)

The model allows for estimation of limit state displacements of the RCFST pier for a given curvature. Yield limit state displacements of a fixed-head RCFST pier can be calculated as follow:

$$\Delta_y = C_1 \phi_{y(top)} L_e^2 \quad (3.8)$$

In Eq. (3.8), C_1 is the yield displacement parameter, $\phi_{y(top)}$ is the yield curvature of the top RC section obtained through a moment curvature analysis, and L_e is the effective length of the cantilever model. C_1 and L_e parameters can be obtained from the following expressions:

$$C_1 = 0.207 - \frac{L_a}{300D} + \frac{D}{2800t} - \frac{\phi}{960}, \quad D(\text{m}), \phi(^{\circ}) \quad (3.9)$$

$$L_e = H_{ig} + L_{sp} \quad (3.10)$$

$$\frac{H_{ig}}{D} = 8.57 + 0.88 \frac{L_a}{D} - \frac{D}{130t} - \frac{\phi}{960} \quad (3.11)$$

In Eq. (3.9), (3.10) and (3.11), L_a is the above ground height, D is the pipe outer diameter, t is the pipe thickness and ϕ is the friction angle of the sand, which is taken as 30, 35 and 40 for flexible, medium and stiff sand, respectively. Eq. (3.5) is used for calculation of L_{sp} . Total displacement response for limit states after yield, the model proposes the following expression:

$$\Delta_{LS} = \Delta_y + (\phi_{LS(top)} - \phi_{y(top)}) L_{p(top)} \beta L_e \quad (3.12)$$

where β is the plastic displacement parameter and it can be obtained as follows:

$$\beta = 0.255 + 0.1D + \frac{L_a}{50D} \left(1 + \frac{D}{170t} \right) + 0.7ALR - \frac{\phi}{160} \quad (3.13)$$

In Eq. (3.13), ALR stands for axial load ratio acting on the RCFST shaft. Montejo et al. (2009) concluded the following expression for the top hinge length, $L_{p(top)}$, which was evaluated through RCFST-fixed head experimental tests.

$$L_{p(top)} = 9.3d_{bl} \frac{f_{uer}}{f_{yre}} + g \quad (3.14)$$

In Eq. (3.14), d_{bl} is the diameter of longitudinal bars, g is the gap between steel pipe and the adjacent member, f_{yre} and f_{sue} are the longitudinal expected yield and ultimate stress, respectively.

3.4.2 Equivalent Viscous Damping

3.4.2.1 RC and RCFST Bridge Piers

Equivalent viscous damping ratios of the piers for a given limit state can be estimated and include components of elastic and hysteretic damping. Elastic damping can be taken as 0.05 for concrete structures. Hysteretic damping relates to the energy dissipated when the structure undergoes inelastic deformation. Priestley et al. (2007) suggests the following expression for estimating equivalent damping of RC bridge piers:

$$\xi_{eq} = 0.05 + 0.444 \left(\frac{\mu - 1}{\mu\pi} \right) \quad (3.15)$$

The hysteretic damping part of the Eq. (3.15) is defined as a function of ductility demand, μ , of the pier. Ductility is defined by the ratio of limit state displacement to the yield limit state displacement as shown in Eq. (3.16).

$$\mu = \frac{\Delta_{LS}}{\Delta_y} \quad (3.16)$$

Effective length idealization for a RCFST system is composed of two parts. The first is the portion of the member above the ground and the second is the portion of the member below the ground. Normally, there will be a soil damping contributing to the overall damping of the RCFST system due to the interaction between soil and the below ground portion of the member. However, in order to avoid soil modelling for structural analysis of RCFST bridges, the soil damping contribution to the equivalent viscous damping calculation has been ignored in this study. Thus, the RC damping expression has also been employed for RCFST bridges.

Equivalent viscous damping of the piers that remain elastic when the critical pier reaches its limit state is taken as 5%.

3.5 Equivalent System Properties at Performance Limit States

DDBD characterizes MDOF structures with equivalent SDOF system properties (equivalent mass, equivalent viscous damping, and effective period) for a given target displacement. After obtaining deformation limit states of piers in a bridge, equivalent system properties at each limit state can be identified following DDBD principles.

3.5.1 Limit State System Displacement

Limit state system displacement evaluation in the transverse direction requires definition of the displaced shape of the bridge which depends on bridge geometry, superstructure stiffness, substructure stiffness and abutment fixity conditions. In this study, the displacement shape of the case study bridges at each limit state is defined under the assumption that the superstructure is rigid, and abutments are free to move and rotate. Hence, deformation shape definition of the bridges depends solely on relative column stiffness. Given these assumptions, possible deformation shapes considered in this study are illustrated in Figure 3.5.

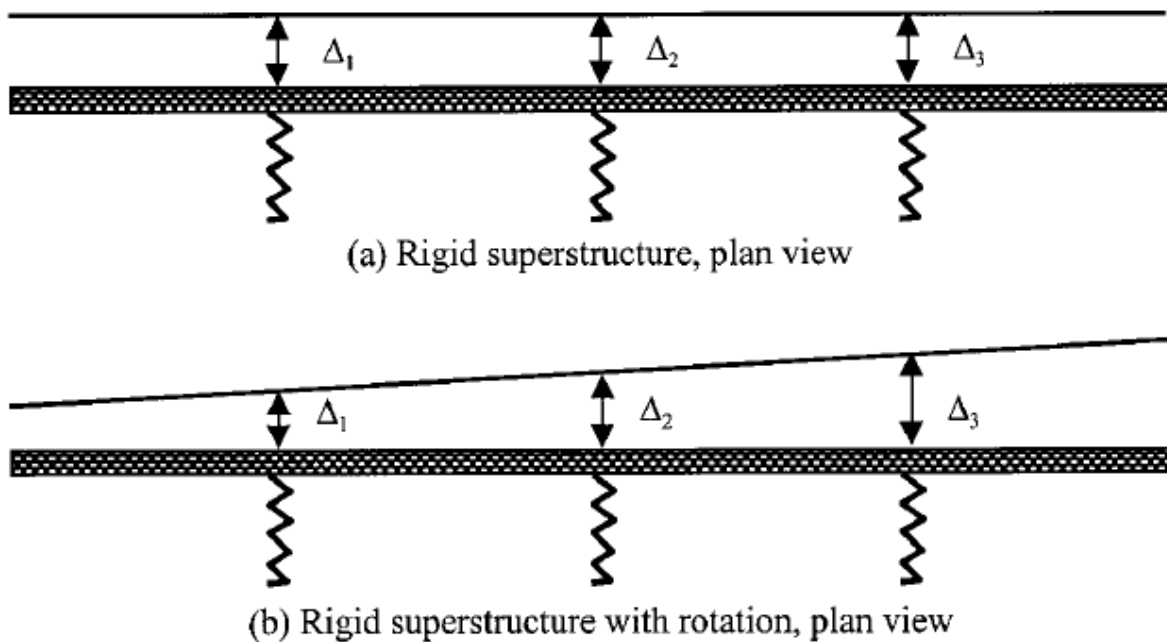


Figure 3.5 Possible inelastic displacement shapes for continuous bridges with rigid superstructure and no abutment restraint: (a) rigid superstructure, plan view, (b) rigid superstructure with rotation, plan view Kowalsky (2002)

Kowalsky (2002) proposed an effective modal analysis (EMA) procedure to obtain the displaced shape for displacement-based design of continuous deck bridges. The proposed procedure adopts “Eigen Value Analysis” (EVA) to define displaced shape of the bridge. In case of a rigid superstructure and no abutment restraint, the procedure requires no iteration. EVA is not required for bridge piers with the same deformation capacities as pier limit state displacements will define bridge limit state displacements (Fig. 3.5a). If bridge piers have different deformation capacities, EVA analysis of the bridge is conducted, and the resulting first mode shape in the transverse direction is recognized as displaced shape of the bridge. Next, the shape is scaled until one of the piers reaches its prescribed limit state. The pier that reaches the limit state is recognized

as the critical pier and its limit state displacement Δ_{cr} . The displacement of the other piers is obtained based on Δ_{cr} in proportion to the mode shape.

$$\Delta_i = \frac{\Delta_{cr} \Phi_i}{\Phi_{cr}} \quad (3.17)$$

Index i denotes the number of the pier. Thus, Φ_i is the shape factor of the i^{th} pier, Φ_{cr} is the shape factor of the critical pier, and Δ_i is the displacement of the i^{th} pier. Once the pier displacements have been obtained at the deformed shape associated with a limit state, the system displacements can be found as follows:

$$\Delta_{LS,sys} = \frac{\sum_{i=1}^n m_i \Delta_i^2}{\sum_{i=1}^n m_i \Delta_i} \quad (3.18)$$

where m_i and Δ_i are the lumped masses and displacements at the pier locations. Equivalent mass at each limit state is defined by:

$$m_{LS,eff} = \frac{\sum m_i \Delta_i}{\Delta_{LS,sys}} \quad (3.19)$$

3.5.2 Equivalent Limit State System Damping

Equivalent system damping of the bridge can be obtained by combining the effective damping of each bridge component in proportion to the work done by each component (Priestley et al., 2007). Due to the rigid superstructure and free abutment assumption, all shear forces will be carried by the piers. Therefore, piers will be the only bridge component that undergoes deformation in the bridge system. It is also very likely that all the columns would have equal longitudinal steel ratios which results in equal moment capacity. In the case of bridge piers with equal moment

capacities, each pier shear force will be inversely proportional to height. Thus, the system damping at each limit state can be obtained by combining individual pier damping as follows:

$$\xi_{eq,LS} = \frac{\left(\sum_{i=1}^n \frac{1}{H_i} \Delta_{i,LS} \xi_{i,LS}\right) / \sum_{i=1}^n \frac{1}{H_i}}{\left(\sum_{i=1}^n \frac{1}{H_i} \Delta_{i,LS}\right) / \sum_{i=1}^n \frac{1}{H_i}} \quad (3.20)$$

in Eq. (3.20) where H_i , $\Delta_{i,LS}$, and $\xi_{i,LS}$ are the height, limit state displacement, and equivalent damping of i^{th} the pier, respectively.

3.5.3 Effective Limit State Periods

Depending upon the type of the bridge pier (RC or RCFST), different approaches were taken to identify effective periods at performance limit states. Below are two sub-sections to explain approaches used for RC and RCFST bridges.

3.5.3.1 RC Bridges

The effective limit state period can be calculated if the effective mass, $m_{LS,eff}$, and the secant stiffness, k_s , at that limit state are known, given in equation (3.21).

$$T_{LS,eff} = 2\pi \sqrt{\frac{m_{LS,eff}}{k_s}} \quad (3.21)$$

$$k_s = \frac{V_{LS,Base}}{\Delta_{LS,sys}} \quad (3.22)$$

Effective mass of the system for a limit state is obtained from Eq. (3.19). In order to find the secant stiffness, k_s , at a particular limit state, the base shear, $V_{LS,Base}$, associated with the limit state system displacement, $\Delta_{LS,sys}$, needs to be identified, given in equation (3.22). The base shear for

a limit state of interest can be obtained by assembling each individual force-deformation response based upon the deformed shape of the bridge.

The force level that corresponds to a deformation demand over the pier can be easily obtained from the moment-curvature relationship of the pier section.

$$F = \frac{M}{L_c} \quad (3.23)$$

In Eq. (3.23), M denotes any bending moment value from the moment-curvature response, and consideration of L_c again depends upon whether the pier is in single ($L_c = H$) or double bending ($L_c = H/2$). The curvature values of the section are translated into displacements using the expressions from section 3.4.1.1. Bilinear moment-curvature relationships provided by CUMBIA were utilized to generate the force-deformation relationship of the piers. Bilinearization of a complete moment-curvature response is outside the scope of this study, the reader can be referred to Montejo and Kowalsky (2007) and Priestley et al.(2007) for information about the concept.

Once the force-deformation response of each pier is known in a bridge, the base shear for a limit state of interest can be obtained by assembling force-deformation response of the piers. Note that assemblage of pier force-displacement responses needs to be consistent with the assumed displacement shape. That is, first, the pier forces due to attainment of the prescribed limit state by the critical pier are identified, followed by summation of these resulting forces to produce the base shear for the limit state. The schematic explaining this process is illustrated in Figure 3.6.

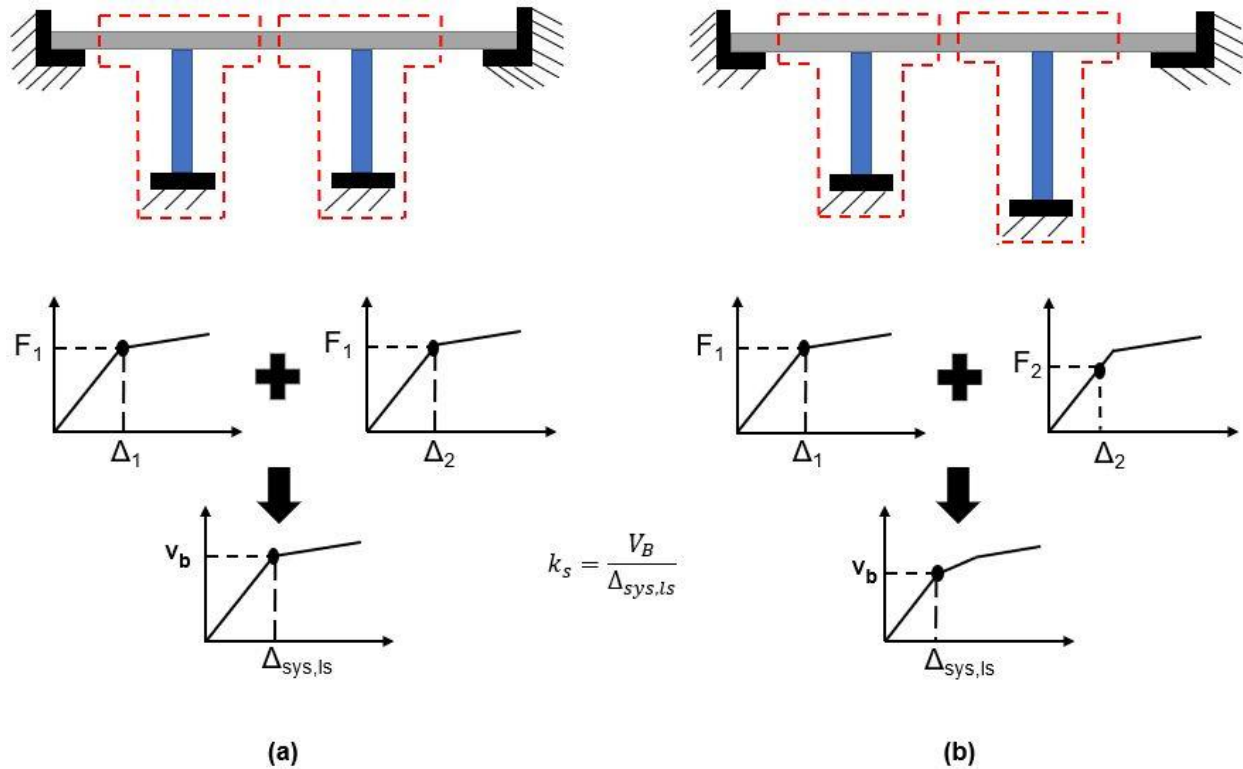


Figure 3.6 Secant stiffness determination for a limit state: (a) piers with same deformation capacities (b) piers with different deformation capacities.

3.5.3.2 RCFST Bridges

As stated before, an RCFST member contains two different sections (RC and RCFST), which result in a non-uniform flexural stiffness distribution along the member. Therefore, using the length of the member to obtain the force for a given displacement, as done for RC piers, will not apply to RCFST piers as contra-flexure length along the member will vary at each limit state. To tackle this issue, the effective period of RCFST bridges was estimated by a slightly different approach than that of RC bridges. First, an inelastic mechanism was selected for fixed-head RCFST piers. Based on the observation by Aguirre (2017) for fixed-head RCFST systems, it was assumed that the top hinge reaches its damage-control limit state while the bottom hinge stays

elastic. With this premise being made, the effective period of the bridge can be directly estimated through an Eigen value analyses (EVA) if the stiffness of the top hinge can be defined by the limit state displacement. Cracked section stiffness for both RC and RCFST sections were used to define member stiffness of the RCFST member. Cracked section stiffness is defined by the following expression (Priestley et al., 2007):

$$E_c I_e = \frac{M}{\phi} \quad (3.24)$$

In Eq. (3.24), where ϕ is the curvature that corresponds to a displacement demand over the pier, M is the corresponding moment value and E_c is the modulus elasticity of the concrete, and it is defined as follows:

$$E_c = 5000\sqrt{f_{ce}} \quad (3.25)$$

The cracked section stiffness of the sections was generated using bilinear moment curvature responses for both RC and RCFST sections at a limit state of interest. For EVA of the bridge, the pier length composed of RC and RCFST members was modelled as its effective length (see section 3.4.1.2). The length of the top RC member was assumed to be four times top plastic hinge length.

The steps of the procedure applied in this study to estimate effective limit state period of a RCFST fixed-head bridge are summarized as follows:

1. Generate bilinear moment-curvature responses for both RC and RCFST sections in each pier.
2. Identify moment and curvature values at each limit state for top RC sections in each pier and only the yield moment and curvature for RCFST sections.

3. Calculate limit state displacements of each pier using limit state curvatures of the top RC sections (Section 3.4.1.2).
4. Select displaced shape of the bridge based on deformation capacities of the piers (Section 3.5.1).
5. Identify the critical pier through the selected displaced shape (Section 3.5.1).
6. Find the displacement demand for each pier when the critical pier reaches its limit state displacement.
7. Convert each pier displacement into corresponding curvature through the equivalent cantilever model by Aguirre (2017). For piers that responds elastically, their yield curvature values are used. For piers that respond beyond yield, the corresponding curvature is identified from Eq. (3.12), reproduced here for convenience.

$$\Delta_{LS} = \Delta_y + (\phi_{LS(top)} - \phi_{y(top)})L_{p(top)}\beta L_e \quad (3.11)$$

8. After defining curvature levels of each pier when the critical pier reaches its limit state, corresponding moment values from the generated bilinear moment-curvatures are determined.
9. Using Eq. (3.24) cracked section stiffness of RC and RCFST members in each pier are obtained. Note that for RC members, moment and curvature values identified at step 7 and step 8 are used, but for RCFST members only yield moment and yield curvature are obtained.
10. The resulting cracked section stiffnesses are used for EVA analysis of the bridge and the resulting period is recorded as the limit state period of the bridge.

3.6 Performance Level Estimation

When system displacement, equivalent damping and effective period are obtained at each limit state, the performance level of the bridge for a limit state can be evaluated comparing limit state system displacement with the corresponding seismic displacement demand. Generally, seismic hazards are defined at the 5% elastic damping level. Therefore, all serviceability and damage-control limit state displacements are converted to 5% damping level in order to facilitate limit state-demand comparison for a given displacement spectrum. Damping scaling factors (DSF) in DDBD are utilized to generate displacement spectrum for a specific damping level associated with the target displacement. Utilizing a DSF expression, equivalent 5% limit state displacements can be found by dividing the limit state system displacement by the corresponding scaling factor.

$$\Delta_{eqLS,sys} = \frac{\Delta_{sys,ls}}{DSF} \quad (3.26)$$

Kong, C. and Kowalsky (2016) proposed a simplified *DSF* expression based on the Rezaeian et al. (2014) DSF model. The proposed DSF expression is a function of period T , damping ratio ξ , and magnitude M .

$$\text{for } 0.2s \leq T_{eff} \leq 0.75s$$

$$DSF = \left(\frac{12}{7 + \xi}\right)^{0.5} - \frac{9.2\sqrt{\xi}}{500} + \frac{7.6 - M}{3 + 30\left(\frac{12}{7 + \xi}\right)^{1.5}} \log_{10} 0.75 \quad (3.27)$$

for $0.75s \leq T_{eff} \leq 10s$

$$DSF = \left(\frac{12}{7+\xi}\right)^{0.5} - \frac{9.2\sqrt{\xi}}{500} + \frac{7.6-M}{3+30\left(\frac{12}{7+\xi}\right)^{1.5}} \log_{10} T_{LS,eff} \quad (3.28)$$

Upon defining limit state displacements at 5% damping, the performance level of the bridge for a limit state is defined by the ratio of the limit state displacement to the corresponding displacement demand under a given elastic displacement spectrum. If this ratio is greater than unity it is interpreted that the limit state will not likely be achieved under the considered seismicity. In the case where the ratio is equal or less than unity, it is expected that the bridge reaches the considered limit state.

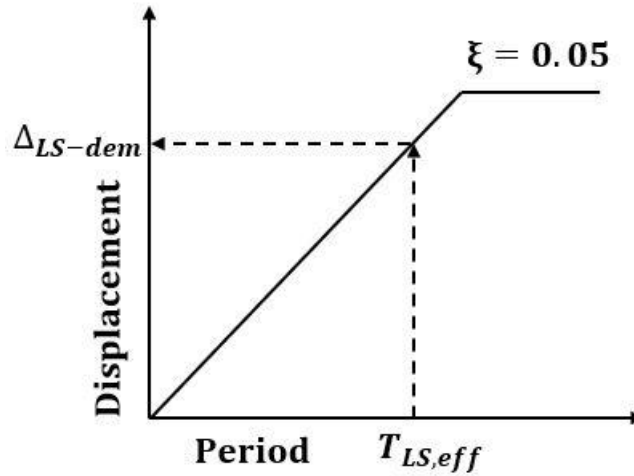


Figure 3.7 Definition of the equivalent elastic limit state demand

$$L.S./D. = \frac{\Delta_{LS-dem}}{\Delta_{eqLS,sys}} \quad (3.29)$$

CHAPTER 4

4. ASSESSMENT APPLICATION of the CASE STUDY BRIDGES

4.1 Introduction

In this chapter, the previously defined direct displacement-based assessment (DDBA) methodology was applied to the case study bridges from Alaska (AK). Only the transverse response of the bridges was considered assuming that the superstructure and the cap-beam behave rigidly without abutment restraint in the direction of loading. Acceleration and displacement response spectrum were generated at the bridge sites under a scenario earthquake that is processed by ShakeMap. DDBA estimations were made at yield, serviceability and damage-control performance limit states (PLS) of the bridges. Incremental Dynamic Analysis (IDA) was used as a nonlinear analysis method to test accuracy of DDBA estimations. Finally, rapid seismic assessment of two reinforced concrete (RC) and one reinforced concrete steel filled tube (RCFST) bridge was conducted under the 2018 Anchorage AK Earthquake (M7.1).

4.2 General Information about the Bridges

Distribution of the considered bridges over the AK region is shown in Figure 4.1. All of the bridges have multi-column bents and “Bulb-Tee” girders. Drawings of the bridges will be given in the Appendix. In this section, information about general layouts, configuration and column section properties of the bridges is provided. Figure 4.2 and Figure 4.3 show typical layouts for the case study RC and RCFST bridges, respectively. Table 4.1 shows configuration summaries for the bridges, and Table 4.2 presents column section and material properties for each bridge. In addition to the material properties given in Table 4.2, all longitudinal and transverse reinforcing steel are *ASTM A706, Grade 60*, and all steel pipe is *ASTM A709, Grade 50*. Therefore, yield stress

of reinforcing steel and steel pipe are taken as 420 and 345 MPa, respectively (“ASTM A706 / A706M” and "ASTM A709 / A709M", 2019). Ultimate stresses for both reinforcing and pipe steel are approximated by taking one and half times of the yield stresses. Pipe thickness is 25mm, and the gap between pipe and adjacent member is 50mm for all RCFST bridges.

Column axial load, P , considers weights from the superstructure and substructure. The former comprises weights of the paving and girder, and the latter comprises weights of cap beam, pier diaphragm and column self-weight. Area density for paving, ρ_{Ap} , is 2.4 kPa, and unit weight of concrete, ρ_c , has been taken as 23.5kN/m³. First, the superstructure load acting on the bent is identified. Weights of paving and girders are converted into distributed loads along the length of the superstructure. Next, using tributary superstructure length, the superstructure load acting on the bent, P_{sb} , is calculated. Since the cap beam load, P_{cb} , and pier diaphragm load, P_{pd} , is already at the bent level, P is determined by adding column self-weight, P_c , to the axial load due to the superstructure, cap beam and pier diaphragm, given in equation 4.1.

$$P = \frac{P_{sb} + P_{cb} + P_d}{N_c} + P_c \quad (4.1)$$

In eq. (4.1), where N_c is the number of columns in the bent.



Figure 4.1 Satellite view of the bridge locations in Alaska (Google Earth, 2019)

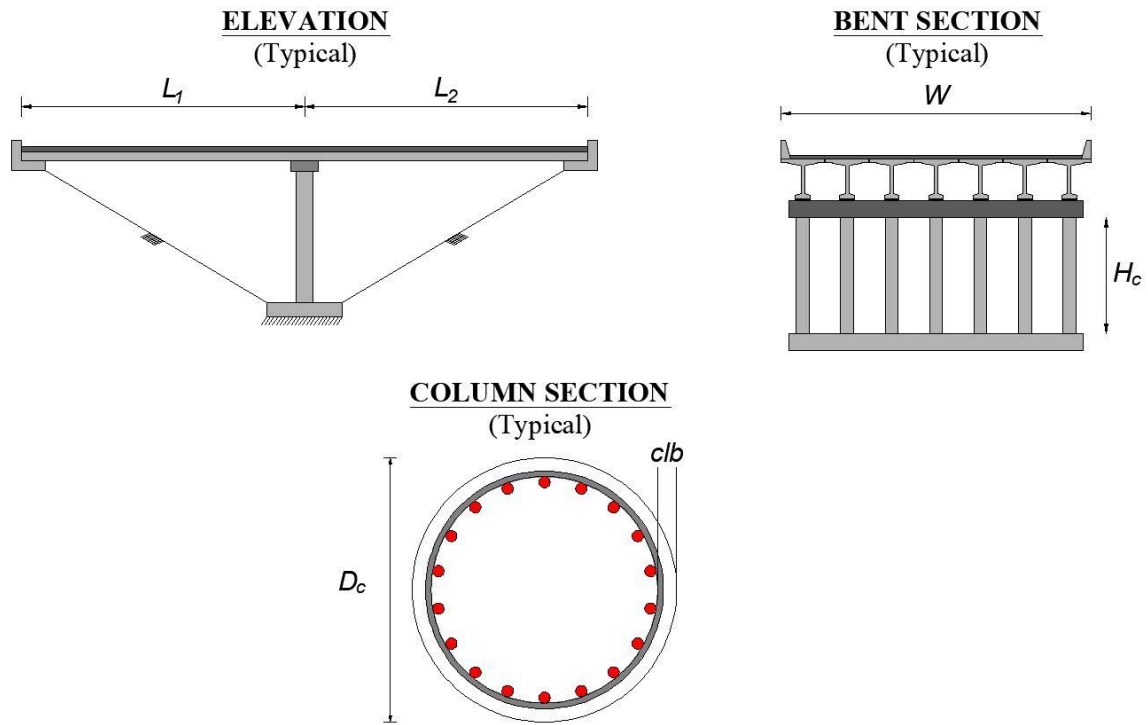


Figure 4.2 General layout of RC bridges

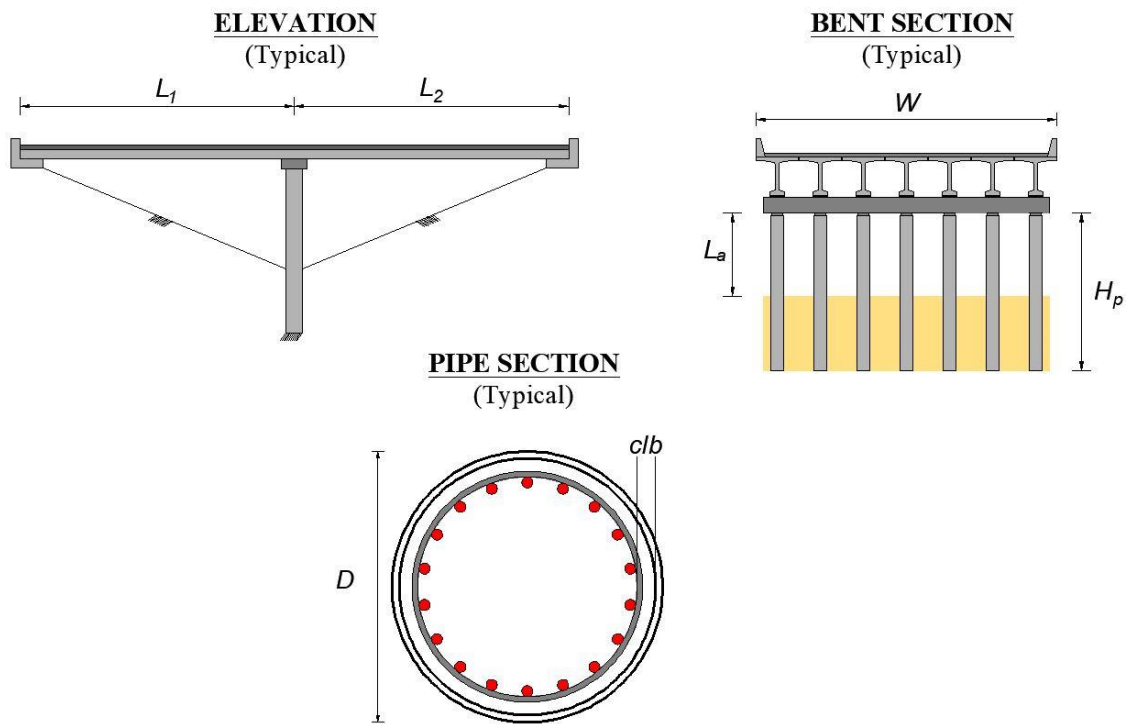


Figure 4.3 General layout of RCFST bridges

Table 4.1 Bridge configuration summary

Bridge Type	Bridge ID (BN)	N_s	L_i (m)	N_g	W (m)	N_c	$H_{c,j} H_{p,j}$ (m)	$L_{a,j}$ (m)
RC	1903	2	44.4,44.4	12	22.5	8	8.2	N.A.
	1391	2	39.5,42.6	13	27.13	8	7.2	N.A.
	0547	3	36.5,36.5,36.5	6	11.70	2	13.4,13.4	N.A.
RCFST	0596	2	35,35	8	16.28	6	14.0	2.82
	0597	2	35,35	8	16.28	6	14.0	3.72
	0639	2	36.7,36.7	7	13.11	4	20.7	2.59
	0610	3	38.9,39,38.9	6	11.89	2	31.3,22.3	4.09,5.04

Note: Numbering for i and j is from left to right. In the table above, N_s is the number of spans, L_i is the length of i^{th} span, N_g is the number of girders in the superstructure, W is the width of the superstructure, N_c is the number of columns per bent, $H_{c,j}$ is the height of the column and $H_{p,j}$ is the height of the pipe at j^{th} bent and $L_{a,j}$ is the above ground height at j^{th} bent, which is not applicable (N.A.) to RC bridges.

Table 4.2 Column Section Properties

Bridge ID (BN)	D (mm)	clb (mm)	Long. Steel (ρ_l)	Trans. Steel (ρ_s)	f'_c (MPa)	$\frac{P}{f'_{ce}A_g}$
1903	914	64	18#11 (2.8%)	#4 at 88.5mm (0.7%)	21	0.092
1391	914	51	18#11 (2.8%)	#4 at 88.9mm (0.7%)	21	0.170
0547	1520	69	24#14 (1.9%)	#6 at 75.0mm (1.1%)	28	0.052
0596	1220	66	20#14 (2.7%)	#5 at 75.0mm (5.5%)	28	0.038
0597	1220	66	20#14 (2.7%)	#5 at 75.0mm (5.5%)	28	0.038
0639	1220	67	16#10 (1.2%)	#5 at 76.2mm (5.5%)	28	0.046
0610	1220	67	20#10 (1.5%)	#5 at 76.2mm (5.5%)	28	0.098,0.093

Note: clb is the cover to longitudinal bars, and A_g is the gross area of the section. The longitudinal bar Nominal Diameter (mm) for #4=12.7mm, #5=15.875mm, #10=32.26mm, #11=35.81mm and #14=43mm (“Harris Supply Steel Rebar Sizes”, 2019)

4.3 Equivalent System Properties of the Bridges

This section presents the results of equivalent system properties of the bridges at yield, serviceability and damage-control performance limit states. The procedure will be applied for BN0547 and 0610 as examples of RC and RCFST bridges, respectively.

BN0547

Figure 4.4 shows an elevation view of the bridge. Other details about the bridge can be found in the Appendix. Simplified bridge geometry considered in identifying equivalent system properties is illustrated in Figure 4.5. Since piers in the bridge contain the same column heights and section properties (see Figure 4.5 and Table 4.2), system properties of the bridge can be defined by one of the piers.

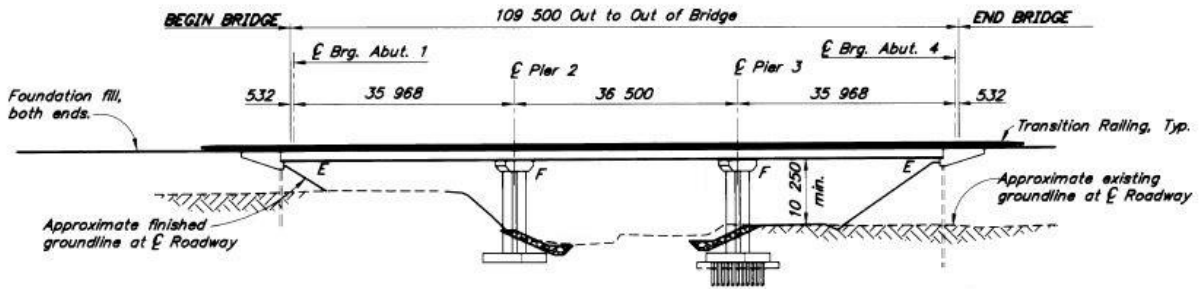


Figure 4.4 Elevation view of BN0547

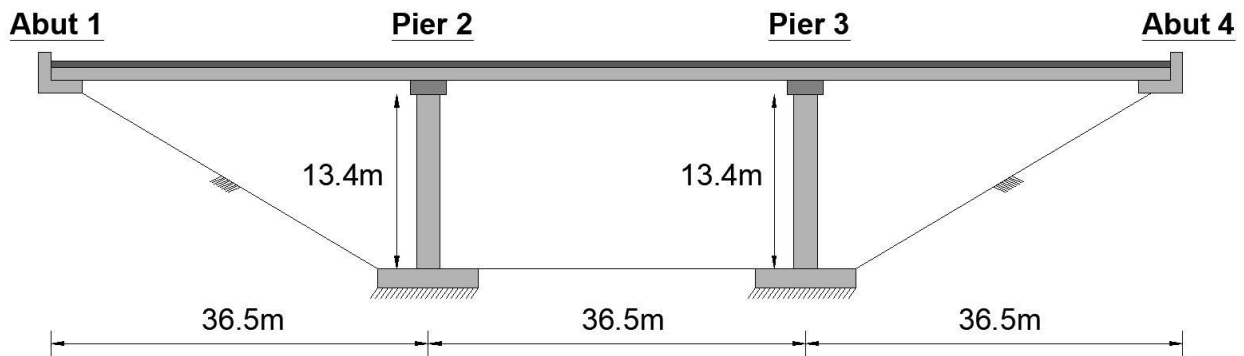


Figure 4.5 Simplified bridge geometry for BN0547

Step 1 Moment-Curvature Response

Figure 4.6 shows complete and bilinear moment-curvature response of the column section along with that of three strain-based limit-states (LS). Table 4.3 gives limit state moment and curvature values. Note that, the moment value at a LS are identified from bilinear moment-curvature response of the section.

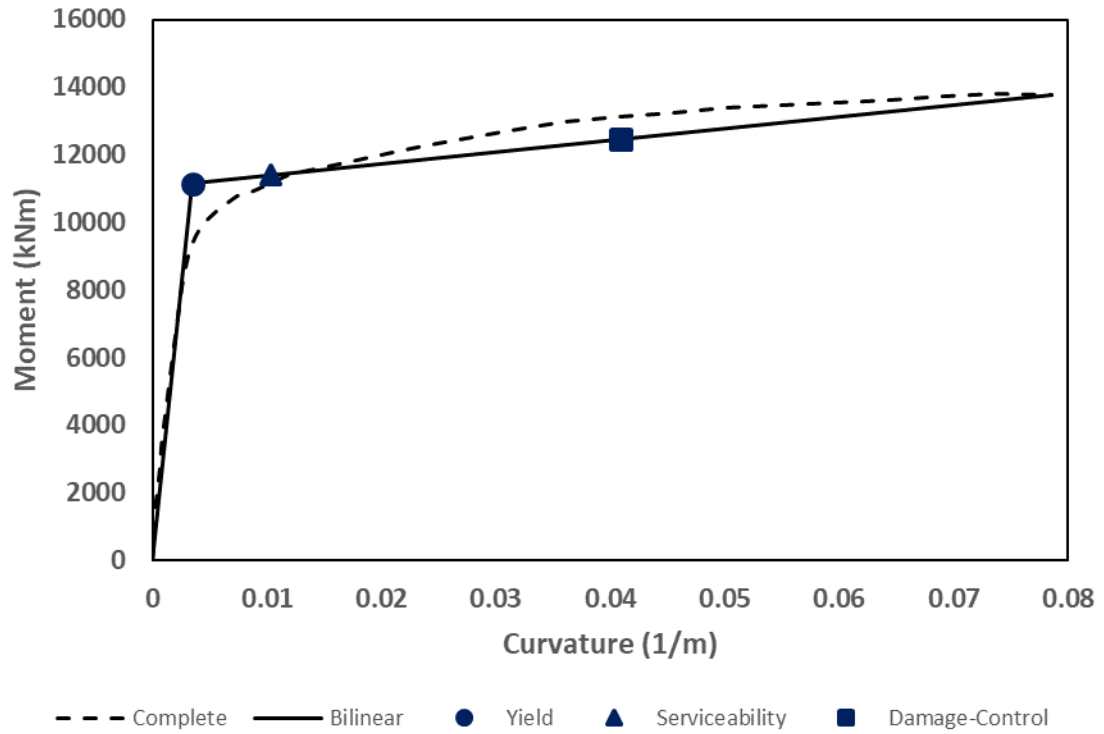


Figure 4.6 Moment-curvature response of BN0547 pier section

Table 4.3 Limit state curvature and moment values of BN0547 pier section

Performance Level	Curvature (1/m)	Moment (kNm)
Yield	0.0035	11158
Serviceability	0.0103	11397
Damage-Control	0.0409	12471

Step 2 Deformation limit states of the piers

Multi-column piers can be considered to develop equal moments at top and bottom of the columns under transverse response (Priestley et al., 2007). Thus, double bending is considered for pier limit state displacements.

Yield Limit State

Yield curvature: $\phi_y = 0.0035/\text{m}$

Yield limit state displacement for double bending:

$$\Delta_y = \frac{\phi_y (H + 2L_{sp})^2}{6}$$

$$L_{sp} = 0.022 f_{yre} d_{bl}$$

$$f_{yre} = 420 \times 1.1 = 462 \text{MPa}$$

$$d_{bl} = 43 \text{mm (Table 4.2)}$$

$$L_{sp} = 0.022 \times 462 \times 43 = 437 \text{mm}$$

$$H_c = 13.4 \text{m (Table 4.1)}$$

$$\Delta_y = \frac{0.0035 \times (13.4 + 2 \times 0.437)^2}{6} = 0.119 \text{m}$$

Serviceability Limit State

Serviceability curvature: $\phi_s = 0.0103/\text{m}$

Limit state displacement beyond yield limit state:

$$\Delta_s = \Delta_y + (\phi_s - \phi_y) L_p H$$

$$L_p = k L_c + L_{sp} \geq 2 L_{sp}$$

$$k = 0.2 \left(\frac{f_{uer}}{f_{yre}} - 1 \right) \leq 0.08$$

$$f_{uer} = 420 \times 1.5 \times 1.1 = 693 \text{MPa}$$

$$k = 0.2 \left(\frac{693}{462} - 1 \right) \leq 0.08 = 0.08$$

$$L_c = 13.4/2 = 6.7\text{m (Double bending } L_c = H/2)$$

$$L_p = 0.08 \times 6.7 + 0.437 = 0.937\text{m} \geq 2 \times 0.437\text{m}$$

$$L_p = 0.937\text{m}$$

$$\Delta_s = 0.119 + (0.0103 - 0.0035) \times 0.937 \times 13.4 = 0.204\text{m}$$

Damage-Control Limit State

Damage-control curvature: $\phi_{dc} = 0.0409/\text{m}$

$$\Delta_{dc} = \Delta_y + (\phi_{dc} - \phi_y) L_p H$$

$$\Delta_{dc} = 0.119 + (0.0409 - 0.0035) \times 0.937 \times 13.4 = 0.589\text{m}$$

Step 3 Equivalent System Properties at Performance Limit States

The bridge is expected to make only translational deformation under transverse response as the piers have the same deformation capacities. Thus, limit state pier deformations obtained in the previous step can be used to define system displacement and damping properties of the bridge at yield, serviceability and damage-control performance limit states (PLS).

$$\Delta_{y,sys} = 0.119\text{m} ; \xi_{y,sys} = 5\%$$

$$\Delta_{s,sys} = 0.204\text{m}$$

$$\mu_s = \frac{\Delta_{LS}}{\Delta_y} = \frac{0.204}{0.119} = 1.71$$

$$\xi_{eq} = 0.05 + 0.444 \left(\frac{\mu - 1}{\pi \mu} \right)$$

$$\xi_s = 0.05 + 0.444 \left(\frac{1.71 - 1}{\pi \times 1.71} \right) = 0.109$$

$$\xi_{s,sys} = 10.9\%$$

$$\Delta_{dc,sys} = 0.589\text{m}$$

$$\mu_{dc} = \frac{0.589}{0.119} = 4.95$$

$$\xi_{dc} = 0.05 + 0.444 \left(\frac{4.95 - 1}{\pi \times 4.95} \right) = 0.163$$

$$\xi_{dc,sys} = 16.3\%$$

As a consequence of the bridge displaced shape, the effective mass is the total mass since all piers sustain the same amount of displacement. The total mass of the bridge considers inertia weights of the superstructure (paving and girders), cap beam, pier diaphragm and one third of columns. Inertia weight of the bridge deemed to interact with seismic loading has been calculated as:

$$W = 16486 \text{ kN}$$

$$m_{eff} = \frac{W}{g} = \frac{16486}{9.81} = 1681 \text{ kNs}^2/\text{m}$$

Effective Limit State Periods

Limit state column forces are defined from the moment-curvature relation of the column section, given in Table 4.3. Addition of limit state column forces based on the displaced shape of the PLS results in the base shear of the bridge for that PLS. Once base shear forces are identified at each PLS, secant stiffness at each PLS can be defined and thus effective limit state periods.

$$\text{Yield moment: } M_y = 11158 \text{ kNm}$$

$$F_y = 11158/6.7 = 1665 \text{ kN}$$

$$V_y = 1665 \times 4 = 6660 \text{ kN (The bridge contains two columns at each bent)}$$

$$k_y = \frac{6660}{0.119} = 55966 \text{ kN/m}$$

$$T_{y,eff} = 2\pi \sqrt{\frac{1681}{55966}} = 1.09 \text{ s}$$

Serviceability moment: $M_s = 11397\text{kNm}$

$$F_s = 11397/6.7 = 1701\text{kN}$$

$$V_s = 1701 \times 4 = 6804\text{kN}$$

$$k_s = \frac{6804}{0.204} = 33353\text{kN/m}$$

$$T_{s,eff} = 2\pi \sqrt{\frac{1681}{33353}} = 1.41\text{s}$$

Damage-Control moment: $M_{dc} = 12471\text{kNm}$

$$F_{dc} = 12471/6.7 = 1861\text{kN}$$

$$V_{dc} = 1861 \times 4 = 7444\text{kN}$$

$$k_{dc} = \frac{7444}{0.589} = 12638\text{kN/m}$$

$$T_{dc,eff} = 2\pi \sqrt{\frac{1681}{12638}} = 2.29\text{s}$$

BN0610

Figure 4.7 and Figure 4.8 show the elevation view and simplified geometry of the bridge, respectively. Piers of the bridge are irregular in terms of above ground column heights. Thus, the piers will have different deformation capacities, and system properties of the bridge will be based on the critical pier.

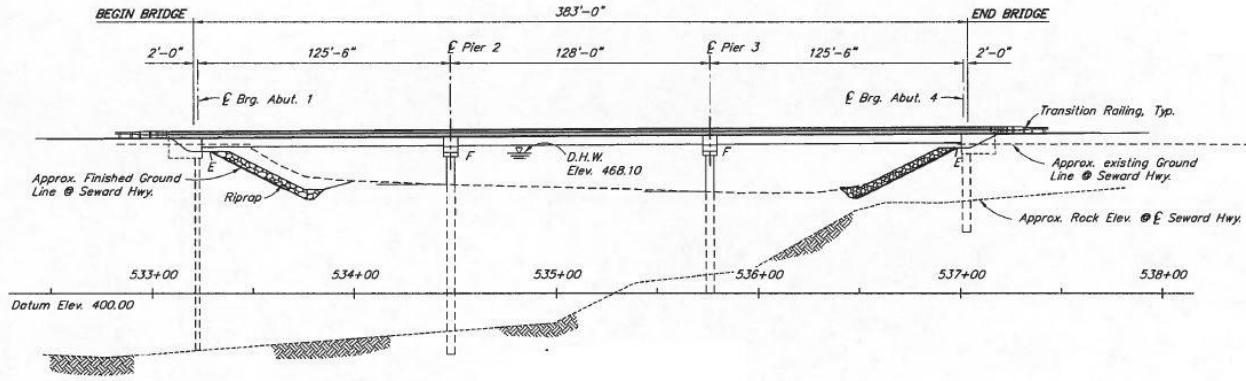


Figure 4.7 Elevation view of BN0610

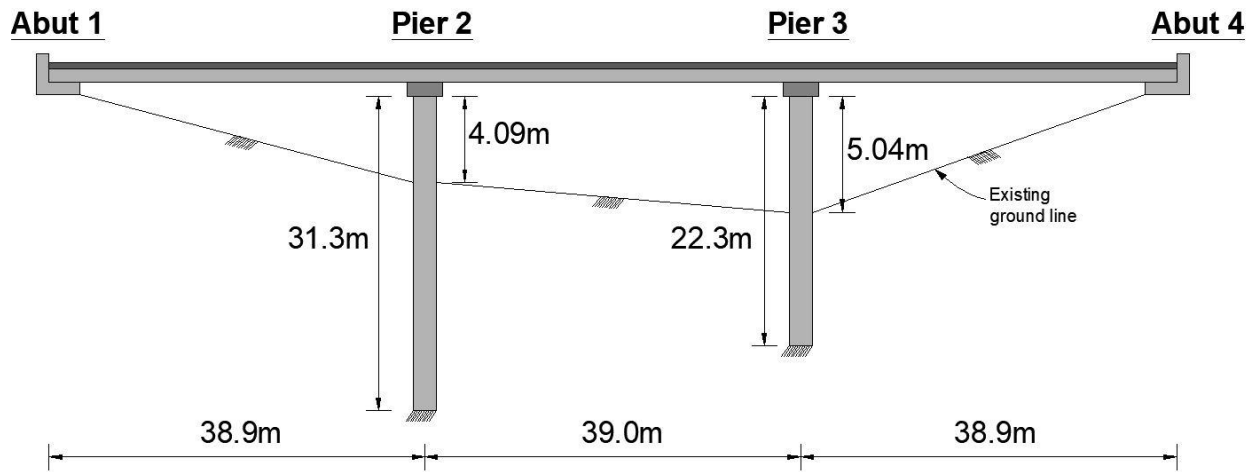


Figure 4.8 Simplified bridge geometry for BN0610

Step 1 Moment-Curvature Response

Due to axial load differences acting on the piers, limit state moment and curvature values of top and bottom hinge sections in the piers are different. Table 4.4 and Table 4.5 presents critical curvature and corresponding moment values for top and bottom-hinge sections of Pier 2 and 3, respectively. Note that only yield curvature and moment values are provided for bottom-hinge since it is assumed to remain elastic during a seismic attack.

Table 4.4 Limit state moment and curvature values of top-hinge sections in the Piers

Performance Level	Pier 2		Pier 3	
	Curvature (1/m)	Moment (kNm)	Curvature (1/m)	Moment (kNm)
Yield	0.00453	4807	0.00452	4757
Serviceability	0.01925	4948	0.01912	4895
Damage-Control	0.07498	5480	0.07476	5422

Table 4.5 Limit state moment and curvature values of bottom-hinge sections in the Piers

Performance Level	Pier 2		Pier 3	
	Curvature (1/m)	Moment (kNm)	Curvature (1/m)	Moment (kNm)
Yield	0.00418	19935	0.00418	19918

Step 2 Deformation limit states

The properties that are same for deformation calculation of the piers are:

$$D = 1.22\text{m}$$

$$t = 25\text{mm}$$

$$f_{yre} = 420 \times 1.1 = 462\text{MPa}$$

$$d_{bl} = 32.26\text{mm (Table 4.2)}$$

$$\phi = 35^\circ$$

$$L_{sp} = 0.022 f_{yre} d_{bl}$$

$$L_{sp} = 0.022 \times 462 \times 32.26 = 328\text{mm}$$

$$L_{p(top)} = 9.3d_{bl} \frac{f_{uer}}{f_{yre}} + g$$

$$g = 50\text{mm}$$

$$f_{uer} = 420 \times 1.5 \times 1.1 = 693\text{MPa}$$

$$L_{p(top)} = 9.3 \times 32.26 \times \frac{693}{462} + 50 = 500\text{mm}$$

Yield Limit State

Yield limit state displacement of a fixed-head RCFST pier:

$$\Delta_y = C_1 \phi_{y(top)} L_e^2$$

$$C_1 = 0.207 - \frac{L_a}{300D} + \frac{D}{2800t} - \frac{\phi}{960}, \quad D(\text{m}), \phi(^{\circ})$$

$$L_e = H_{ig} + L_{sp}$$

$$\frac{H_{ig}}{D} = 8.57 + 0.88 \frac{L_a}{D} - \frac{D}{130t} - \frac{\phi}{10}$$

Pier 2

Yield curvature: $\phi_{y(top)} = 0.00453/\text{m}$

$$C_1 = 0.207 - \frac{4.09}{300 \times 1.22} + \frac{1.22}{2800 \times 0.025} - \frac{35}{960} = 0.177$$

$$H_{ig} = \left(8.57 + 0.88 \times \frac{4.09}{1.22} - \frac{1.22}{130 \times 0.025} - \frac{35}{10} \right) \times 1.22 = 9.33\text{m}$$

$$L_{sp} = 0.328\text{m}$$

$$L_e = 9.33 + 0.328 = 9.66\text{m}$$

$$\Delta_y = 0.177 \times 0.00453 \times 9.66^2 = 0.075\text{m}$$

Pier 3

Yield curvature: $\phi_{y(top)} = 0.00452/\text{m}$

$$C_1 = 0.207 - \frac{5.04}{300 \times 1.22} + \frac{1.22}{2800 \times 0.025} - \frac{35}{960} = 0.174$$

$$H_{ig} = \left(8.57 + 0.88 \times \frac{5.04}{1.22} - \frac{1.22}{130 \times 0.025} - \frac{35}{10} \right) \times 1.22 = 10.16 \text{m}$$

$$L_{sp} = 0.328 \text{m}$$

$$L_e = 10.16 + 0.328 = 10.49 \text{m}$$

$$\Delta_y = 0.174 \times 0.00452 \times 10.49^2 = 0.087 \text{m}$$

Serviceability Limit State

$$\Delta_s = \Delta_y + (\phi_{LS(top)} - \phi_{y(top)}) L_{p(top)} \beta L_e$$

$$\beta = 0.255 + 0.1D + \frac{L_a}{50D} \left(1 + \frac{D}{170t} \right) + 0.7ALR - \frac{\phi}{160}$$

Pier 2

$$\text{Serviceability curvature: } \phi_{s(top)} = 0.01925/\text{m}$$

$$\beta = 0.255 + 0.1 \times 1.22 + \frac{4.09}{50 \times 1.22} \left(1 + \frac{1.22}{170 \times 0.025} \right) + 0.7 \times 0.098 - \frac{35}{160} = 0.313$$

$$\Delta_s = 0.075 + (0.01925 - 0.00453) \times 0.5 \times 0.313 \times 9.66 = 0.097 \text{m}$$

Pier 3

$$\text{Serviceability curvature: } \phi_{s(top)} = 0.01912/\text{m}$$

$$\beta = 0.255 + 0.1 \times 1.22 + \frac{5.04}{50 \times 1.22} \left(1 + \frac{1.22}{170 \times 0.025} \right) + 0.7 \times 0.093 - \frac{35}{160} = 0.330$$

$$\Delta_s = 0.087 + (0.01912 - 0.00452) \times 0.5 \times 0.330 \times 10.49 = 0.112 \text{m}$$

Damage-Control Limit State

$$\Delta_{dc} = \Delta_y + (\phi_{LS(top)} - \phi_{y(top)}) L_{p(top)} \beta L_e$$

Pier 2

$$\text{Damage-control curvature: } \phi_{dc(top)} = 0.07498/\text{m}$$

$$\Delta_{dc} = 0.075 + (0.07498 - 0.00453) \times 0.5 \times 0.313 \times 9.66 = 0.182\text{m}$$

Pier 3

Damage-control curvature: $\phi_{dc(top)} = 0.07476/\text{m}$

$$\Delta_{dc} = 0.087 + (0.07476 - 0.00452) \times 0.5 \times 0.330 \times 10.49 = 0.209\text{m}$$

Step 3 Equivalent System Properties at Performance Limit States

The bridge is expected to make rotational as well as translational motion due to different deformation capacity of the piers. Thus, EVA of the bridge is conducted in order to obtain the displaced shape of the bridge in the transverse direction. For EVA, the yield limit state moment and curvature values of Pier 2 and 3 are used to define stiffness properties of RC and RCFST members in the piers. The pier lengths are modelled as their effective length, and length of the top RC members are four times the plastic hinge length ($4 \times L_{p(top)}$).

Shape Factors from the EVA

$$\text{Pier 2: } \Phi_2 = 0.870$$

$$\text{Pier 3: } \Phi_3 = 0.740$$

Shape factor of Pier 2 is bigger than Pier 3. This means that Pier 2 will reach its limit state first.

The scale factor proportion to pier 2:

$$\text{Scale Factor} = 1/0.87 = 1.149$$

$$\Phi_2 = 0.870 \times 1.149 = 1.0$$

$$\Phi_3 = 0.740 \times 1.149 = 0.85$$

Yield System Displacement and Damping

Pier 2

$$\Delta_2 = 0.075\text{m}$$

Inertial weight that goes to Pier 2: $W_2 = 8657.5\text{kN}$

Pier 3

$$\Delta_3 = 0.075 \times 0.85 = 0.064 \text{m}$$

Inertial weight that goes to Pier 3: $W_3 = 8675.5 \text{kN}$

$$\Delta_{y,sys} = \frac{8657.5 \times 0.075^2 + 8675.5 \times 0.064^2}{8657.5 \times 0.075 + 8675.5 \times 0.064} = 0.070 \text{m}$$

$$\xi_{y,sys} = 0.05$$

Serviceability System Displacement and Damping

Pier 2

$$\Delta_2 = 0.097 \text{m}$$

$$\mu_2 = 0.097 / 0.075 = 1.29$$

$$\xi_2 = 0.05 + 0.444 \left(\frac{1.29 - 1}{\pi \times 1.29} \right) = 0.082$$

Pier 3

$$\Delta_3 = 0.097 \times 0.85 = 0.082 \text{m}$$

$$\mu_2 = 0.082 / 0.087 = 0.94 \leq 1 \text{ remain elastic}$$

$$\xi_3 = 0.05$$

$$\Delta_{s,sys} = \frac{8657.5 \times 0.097^2 + 8675.5 \times 0.082^2}{8657.5 \times 0.097 + 8675.5 \times 0.082} = 0.090 \text{m}$$

Since the moment capacity of the piers is very close (see Table 4.4 and Table 4.5), it is reasonable to assume that piers have the same moment capacity for finding the system damping of the bridge.

$$\xi_{s,sys} = \frac{\left(\frac{1}{9.67} * 0.097 * 0.082 + \frac{1}{10.50} * 0.082 * 0.050 \right)}{\frac{\left(\frac{1}{9.67} + \frac{1}{10.50} \right)}{\left(\frac{0.097}{9.67} + \frac{0.082}{10.50} \right)}} = 0.068$$

Damage-Control System Displacement and Damping

Pier 2

$$\Delta_2 = 0.182\text{m}$$

$$\mu_2 = 0.182/0.075 = 2.43$$

$$\xi_2 = 0.05 + 0.444 \left(\frac{2.43 - 1}{\pi \times 2.43} \right) = 0.133$$

Pier 3

$$\Delta_3 = 0.182 \times 0.85 = 0.155\text{m}$$

$$\mu_2 = 0.155/0.087 = 1.78$$

$$\xi_2 = 0.05 + 0.444 \left(\frac{1.78 - 1}{\pi \times 1.78} \right) = 0.112$$

$$\Delta_{dc,sys} = \frac{8657.5 \times 0.182^2 + 8675.5 \times 0.155^2}{8657.5 \times 0.182 + 8675.5 \times 0.155} = 0.170\text{m}$$

$$\xi_{dc,sys} = \frac{\left(\frac{1}{9.67} * 0.182 * 0.133 + \frac{1}{10.50} * 0.170 * 0.112 \right)}{\left(\frac{1}{9.67} + \frac{1}{10.50} \right)} \frac{\left(\frac{0.182}{9.67} + \frac{0.170}{10.50} \right)}{\left(\frac{1}{9.67} + \frac{1}{10.50} \right)} = 0.123$$

Effective Limit State Periods

Curvature and moment values for the top-hinge sections of Pier 2 and 3 are determined from the displacement demand over the piers at each performance limit states (PLS). Since Pier 2 is the critical pier, its limit state moment and curvature values from Table 4.4 are used. Pier 3 remains elastic at serviceability PLS, but exceeds its yield when the bridge experiences damage-control PLS. Curvature and moment values of the top section of Pier 3 at damage-control PLS:

$$0.155\text{m} = 0.087 + (\phi_{pier3(top)} - 0.00452) \times 0.5 \times 0.330 \times 10.49$$

$$\phi_{pier3(top)} = 0.0438 \text{ 1/m}$$

Corresponding moment value to this curvature is obtained by interpolating moment-curvature data of Pier 3, given in Table 4.4.

$$M_{pier3(top)} = 4757 + \frac{5422 - 4757}{0.07476 - 0.00452} = 5129\text{kNm}$$

Curvature and moment values for the bottom-hinge sections of Pier 2 and 3 are the same as all PLS because they are not expected to go beyond their yield limit state. Table 4.6 presents curvature and moment values used for defining cracked section stiffness of the pier sections (top and bottom). Cracked section stiffnesses are then distributed to RC and RCFST members in each pier, and effective limit state periods of the bridge are determined through EVA at each PLS.

Table 4.6 Moment and curvature values for cracked section stiffness

Performance Level	Hinge-Location	Pier 2		Pier 3	
		Curvature (1/m)	Moment (kNm)	Curvature (1/m)	Moment (kNm)
Yield	Top	0.00453	4807	0.00452	4757
	Bottom	0.04180	19935	0.04180	19918
Serviceability	Top	0.01925	4948	0.00452	4757
	Bottom	0.04180	19935	0.04180	19918
Damage-Control	Top	0.07498	5480	0.04380	5129
	Bottom	0.04180	19935	0.04180	19918

Limit state period s of BN0610 from EVA:

$$T_{y,eff} = 0.84s$$

$$T_{s,eff} = 0.89s$$

$$T_{dc,eff} = 1.02s$$

In this section, the DDBA procedure has been shown to solve examples from an RC and an RCFST bridge. Summary of equivalent system property results of all bridges is given in Table 4.7.

Table 4.7 Equivalent system properties of the bridges

	Performance Level								
	Yield			Serviceability			Damage-Control		
Bridge ID (BN)	$\Delta_{y,sys}$ (m)	$\xi_{y,sys}$ (%)	$T_{y,eff}$ (s)	$\Delta_{s,sys}$ (m)	$\xi_{s,sys}$ (%)	$T_{s,eff}$ (s)	$\Delta_{dc,sys}$ (m)	$\xi_{dc,sys}$ (%)	$T_{dc,eff}$ (s)
1903	0.085	5	1.18	0.125	9.5	1.42	0.391	16.1	2.41
1391	0.067	5	1.30	0.095	9.2	1.54	0.285	15.8	2.58
0547	0.119	5	1.09	0.204	10.9	1.41	0.589	16.9	2.29
0596	0.064	5	0.46	0.084	8.3	0.51	0.163	13.6	0.61
0597	0.076	5	0.52	0.100	8.4	0.58	0.192	13.5	0.67
0639	0.056	5	0.48	0.070	7.8	0.53	0.124	12.7	0.61
0610	0.070	5	0.84	0.090	6.8	0.89	0.170	12.3	1.02

4.4 Alaska Earthquake Scenario and DDBA Estimations

4.4.1 Earthquake Scenario

The global legacy catalog is one of the earthquake scenario catalogs of USGS that contains a wide range of historical earthquake scenarios from all over the world (“USGS Scenario Catalogs”, 2019). The magnitude 9.2 AK earthquake scenario in that catalog has been chosen to evaluate DDBA estimations. This earthquake scenario represents a realization of the 1964 AK earthquake (M9.2), which is the second largest earthquake with an instrumentally measured magnitude after the 1960 Chile earthquake (M9.5). Metadata and ShakeMap outputs of the

scenario are available on the USGS website (“USGS Alaska Mainshock M9.2 Scenario”, 2019). The scenario earthquake does not consider basin-edge and directivity effects. A subduction zone GMPE by Zhao et al. (2006) and GMICE by Worden et al. (2012) are used to generate site-specific IMTs and Modified Mercalli Intensity (MMI), respectively.

Google Earth intensity overlay of the scenario event is shown in Figure 4.9. The red dot and the blue dots in Figure 4.9 represent the epicenter of the event and the case study bridges, respectively. Figure 4.9 shows that all the bridges are within the regions that experience strong or very strong shaking under this earthquake scenario. Although the bridges appear to be in the area where earthquake intensity is high, earthquake intensity is not sufficient information by itself to draw a conclusion about seismic performance of the bridges. If ground shaking levels are known at the bridge site, a more accurate seismic performance estimation may be achieved by comparing site-specific ground shaking demand with deformation capacity of the bridge. Equivalent system properties of the bridges have been defined in the previous section by system displacement, equivalent damping and effective period at yield, serviceability and damage-control performance limit states. . The next section explains how location-specific ground motion hazard is generated based on IMTs outputs of the scenario earthquake processed by ShakeMap

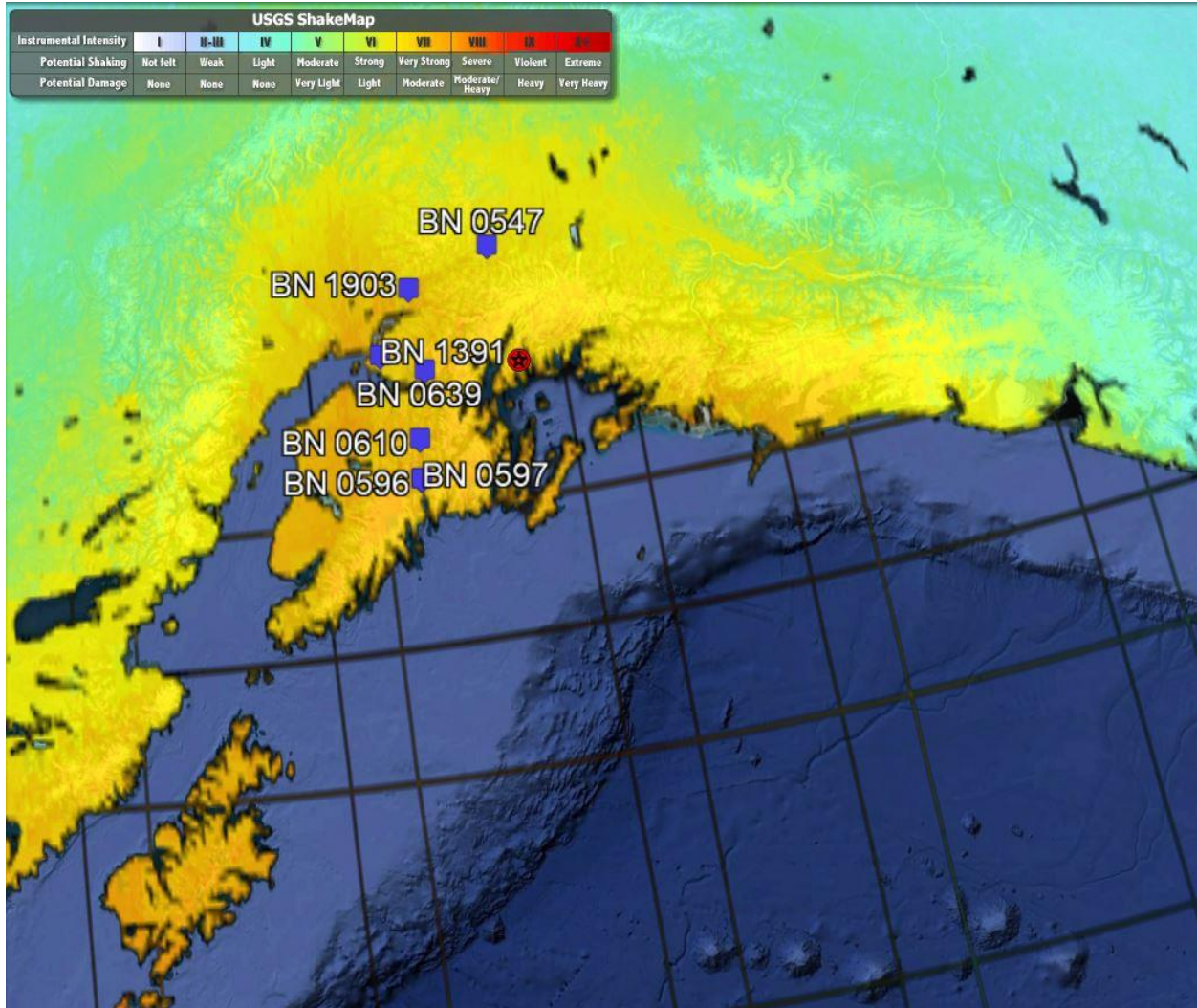


Figure 4.9 Intensity overlay of the earthquake (Google Earth, 2019)

4.4.1.1 Location-specific ground motion hazard

A standardized elastic response spectrum (5% damping) shape, which is shown in Figure 4.10, is used to characterize ground shaking at a bridge site. The spectrum is defined by soil amplified short period spectral acceleration, S_{DS} , soil amplified spectral acceleration at a period of 1 second, S_{D1} , and long-period level, T_L . S_{DS} response is defined by spectral acceleration at a period of 0.3 seconds. T_L is called “long-period transition period” or “corner period” beyond which

spectral displacement responses stay constant. Priestley et al. (2007) proposed the following expression based on the work by Faccioli et al. (2004) for definition of T_L :

$$T_L = \begin{cases} 1 + 2.5(M_w - 5.7); & M_w > 5.7 \\ 1; & M_w \leq 5.7 \end{cases} \quad (4.2)$$

where M_w is the moment magnitude of the earthquake. T_L works out to be 9.75 seconds for the considered earthquake scenario ($M_w = 9.2$).

Having established T_L , elastic response spectrum can be constructed using site-specific spectral acceleration outputs at 0.3 and 1.0 seconds from the ShakeMap scenario earthquake. Grid spacing for IMTs specified by the ShakeMap scenario earthquake (“USGS Alaska Mainshock M9.2 Scenario”, 2019) are 2.786km and 1.352km between two latitudes and longitudes, respectively. In order to obtain IMTs at the bridge locations, the same earthquake scenario was rerun through ShakeMap by specifying coordinates of the bridges and Vs30 values at the bridge locations. Table 4.8 shows inputted bridge locations along with Vs30 values to ShakeMap and the resultant soil amplified spectral accelerations at 0.3 and 1.0 seconds. Vs30 values at the bridge sites have been extracted from USGS Vs30 database (“USGS Vs30 Models and Data”, 2019). This database is a combination of experimentally measured and derived Vs30 values (Alan et. al., 2016). Therefore, Vs30 values, given in Table 4.8, are approximated. If available, experimentally obtained Vs30 values at the bridge sites can also be used to increase the accuracy of site-specific responses, but ShakeMap will use its own Vs30 database to generate site responses for a real event. Figure 4.11 shows elastic acceleration response spectrum generated for each bridge site. Displacement response spectrum are generated from acceleration spectrum using the relationship between displacement and acceleration, given in equation (4.6). Figure 4.12 shows displacement response spectrum at the bridge sites.

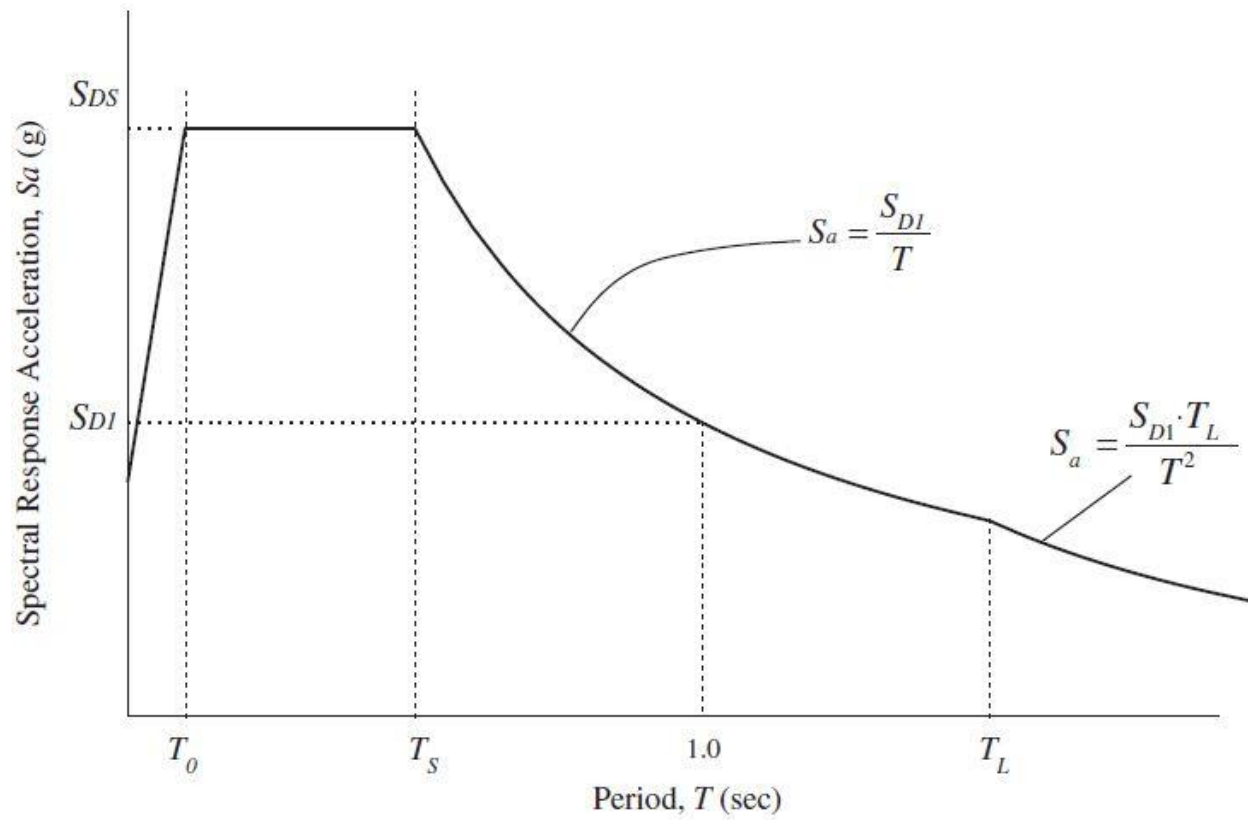


Figure 4.10 Response Spectrum Shape (FEMA 450, 2003)

$$S_a = \begin{cases} S_{DS} \left(0.4 + 0.6 \frac{T}{T_0} \right); & T < T_0 \\ S_{DS}; & T_0 \leq T \leq T_s \\ \frac{S_{D1}}{T}; & T_s < T \leq T_c \\ \frac{S_{D1} T_c}{T^2}; & T > T_c \end{cases} \quad (4.3)$$

$$T_0 = 0.2 \frac{S_{D1}}{S_{DS}} \quad (4.4)$$

$$T_S = \frac{S_{D1}}{S_{DS}} \quad (4.5)$$

$$SD = \frac{T^2}{4\pi^2} S_{A(T)} \quad (4.6)$$

Table 4.8 Bridge locations, Vs30 values and spectral acceleration responses at the periods of 0.3 and 1.0 seconds

Bridge ID (BN)	Latitude	Longitude	Vs30 (m/s)	SA[0.3s] (g)	SA[1.0s] (g)
1903	61.5627	-149.2662	399	0.83	0.39
1391	61.0944	-149.8361	454	0.93	0.43
0547	61.7910	-147.9364	655	0.35	0.20
0596	60.1382	-149.4220	255	1.29	0.66
0597	60.1400	-149.4200	236	1.29	0.66
0639	60.9387	-149.1674	473	1.05	0.48
0610	60.4357	-149.3726	860	0.66	0.34

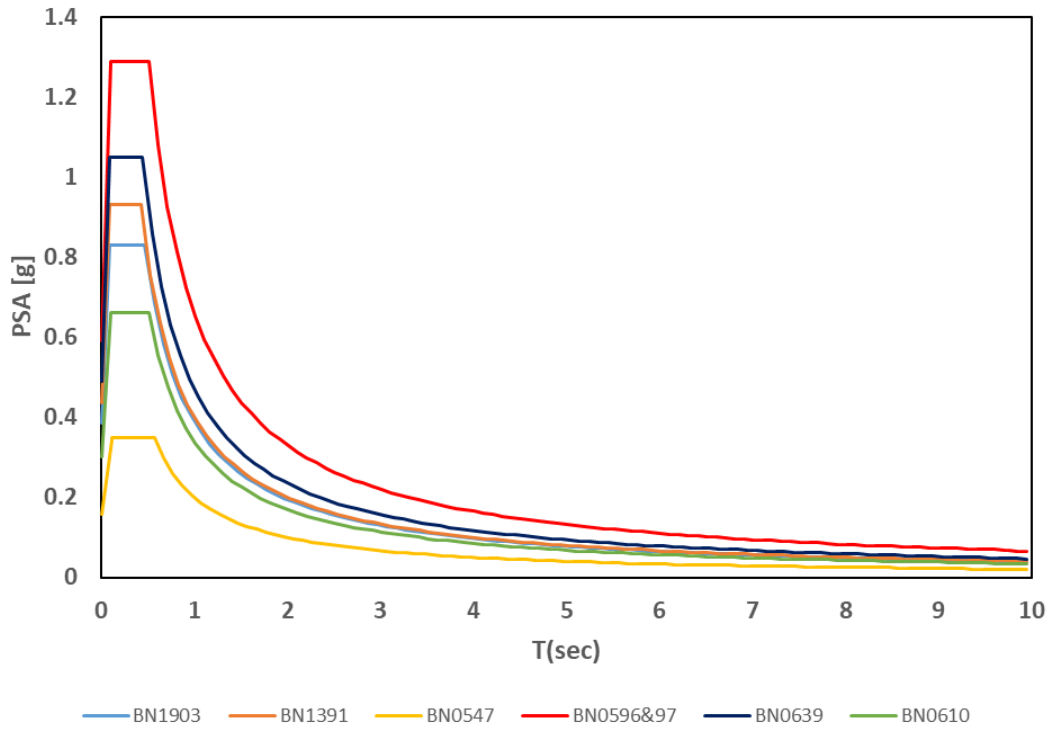


Figure 4.11 Acceleration response spectrum at each bridge site

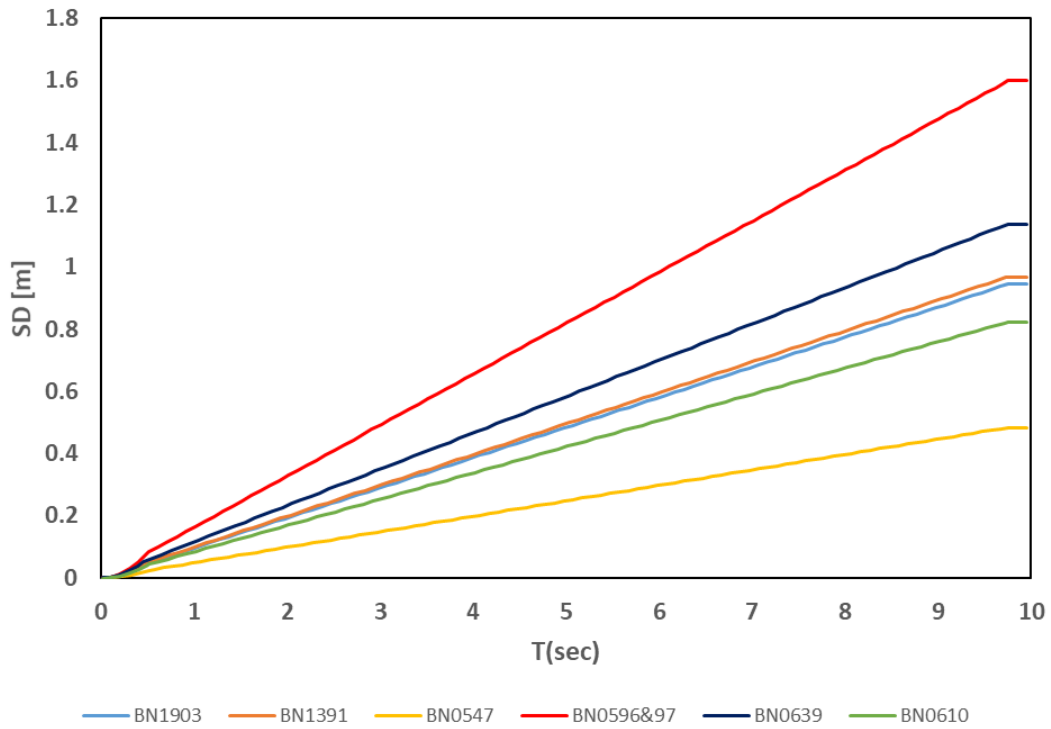


Figure 4.12 Displacement response spectrum at each bridge site

4.4.2 DDBA Estimations

Serviceability and damage-control limit state system displacements of the bridges are converted to 5% elastic damping level by the DSF expression given in Eq. (3.27) or (3.28). Table 4.9 presents equivalent elastic limit state system displacements and effective limit state periods of the bridges. For corresponding effective limit state periods, displacement demands are determined from the individually generated displacement response spectrum at each bridge site (see Figure 4.12). The performance level of the bridges is then estimated by taking the ratio of elastic limit state system displacement to the corresponding demand (LS/D). Figure 4.13, Figure 4.14 and Figure 4.15 show the performance levels of the bridges under this scenario earthquake at yield, serviceability and damage-control, respectively. Figure 4.13 demonstrates that most of the bridges including BN1903, 1391, 0596, 0597 and 0639 have reached or exceeded their yield limit state. LS/D ratios at the serviceability limit state are greater than unity except for BN1391 (see Figure 4.14). Thus, it is likely that BN1391 has achieved the serviceability limit state.

Figure 4.15 shows that none of the bridges achieves damage-control limit state since all the LS/D ratios are greater than unity. Therefore, it can be interpreted that operability of the considered bridges is not of concern under this earthquake scenario. BN0610 and BN0547 remained elastic during this scenario. As a result of this earthquake scenario, field inspection sequence of the bridges ranked in order of importance is given in Table 4.10.

Table 4.9 Elastic limit state system displacements and effective limit state system displacements of the bridges

	Performance Level					
	Yield		Serviceability		Damage-Control	
Bridge ID (BN)	$\Delta_{y,sys}$ (m)	$T_{y,eff}$ (s)	$\Delta_{eqs,sys}$ (m)	$T_{s,eff}$ (s)	$\Delta_{eqdc,sys}$ (m)	$T_{dc,eff}$ (s)
BN1903	0.085	1.18	0.160	1.42	0.652	2.41
BN1391	0.067	1.30	0.120	1.54	0.467	2.58
BN0547	0.119	1.09	0.272	1.41	0.998	2.29
BN0596	0.064	0.46	0.100	0.51	0.230	0.61
BN0597	0.076	0.52	0.119	0.58	0.270	0.67
BN0639	0.056	0.48	0.081	0.53	0.170	0.61
BN0610	0.070	0.84	0.102	0.89	0.236	1.02

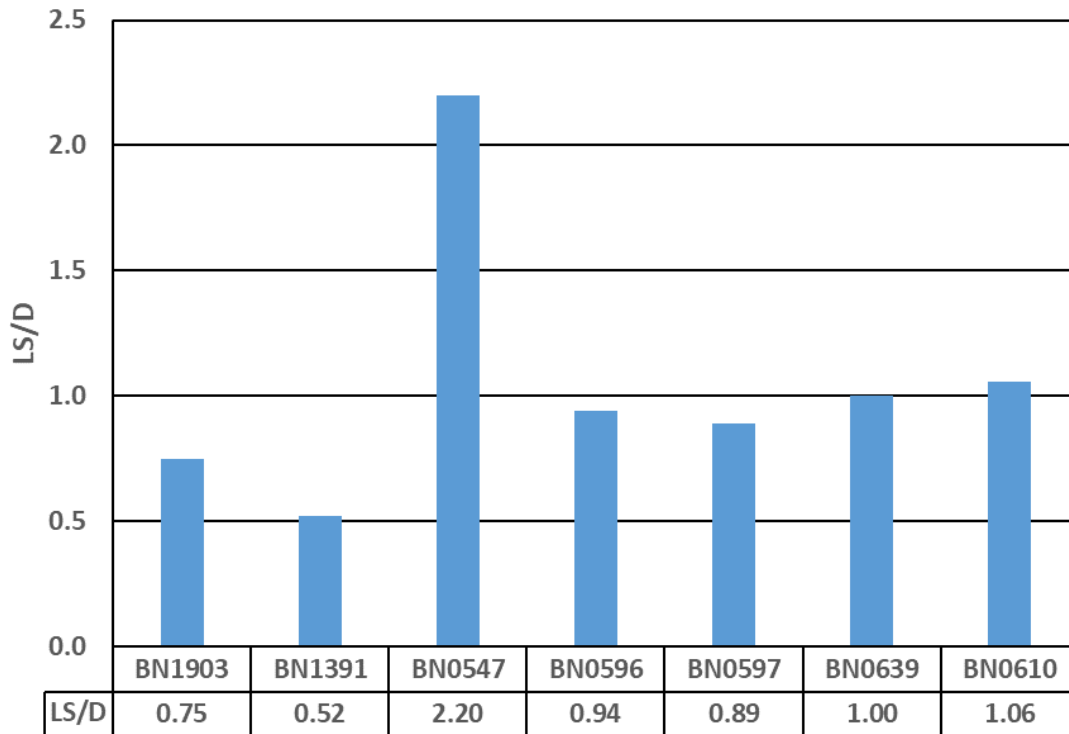


Figure 4.13 Yield performance level

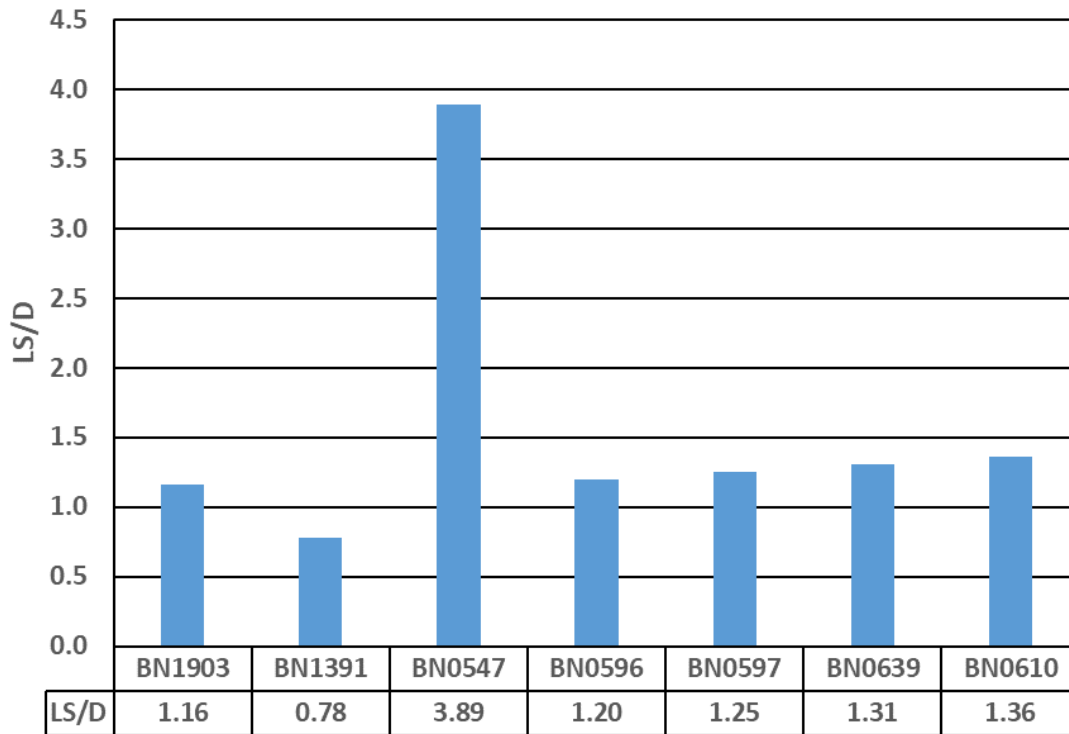


Figure 4.14 Serviceability performance level

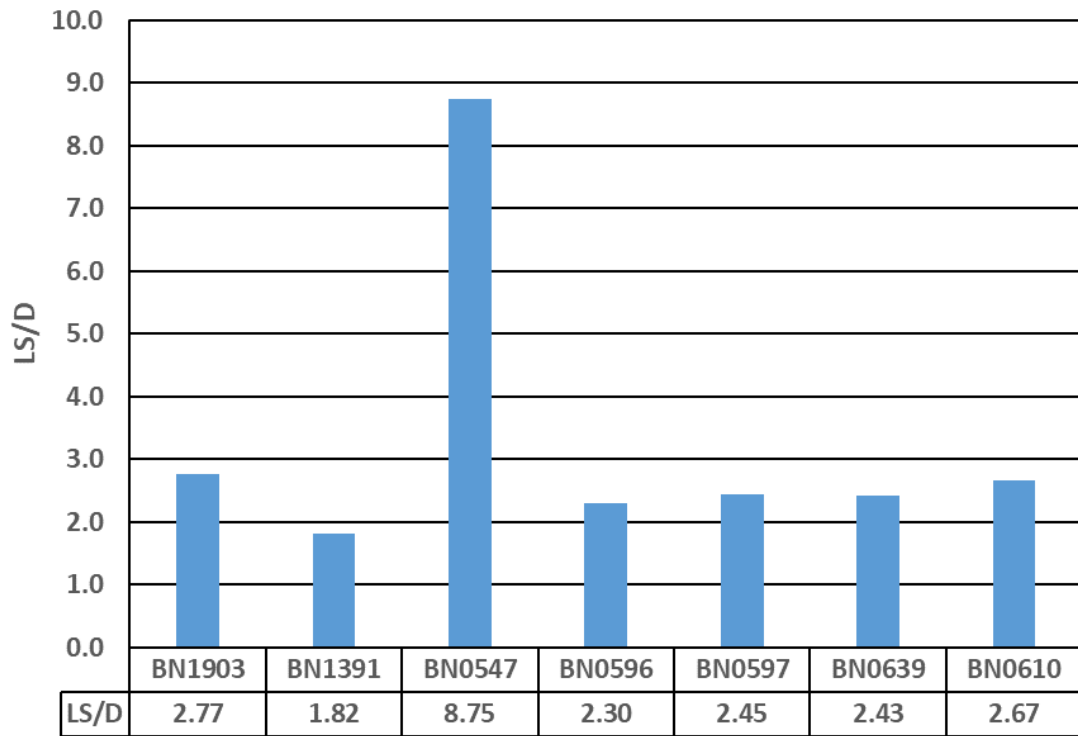


Figure 4.15 Damage-control performance level

Table 4.10 Inspection Priority chart under the considered earthquake scenario

Bridge ID (BN)	Performance Level	Inspection Priority	Inspection Priority Ranking
1391	Serviceability	Medium	1
1903	Yield	Low	2
0597	Yield	Low	3
0596	Yield	Low	4
0639	Yield	Low	5
0610	Elastic	None	6
0547	Elastic	None	7

Inspection priority color scheme based on performance level of the bridge

Damage-Control	Serviceability	Yield	Elastic

4.5 Incremental Dynamic Analysis

Incremental dynamic analysis IDA (Vamvatsikos and Cornell, 2002) has been used as a benchmark tool to verify accuracy of LS/D ratios estimated by the applied DDBA approach. In the IDA procedure, the structure is subjected to a series of inelastic time history analysis (ITHA) by varying the intensity level of input motions. To that end, seven earthquake ground motions, given in Table 4.11, have been individually matched using wavelet theory (Montejo and Suarez, 2013) to each acceleration response spectrum at the bridge sites. This has resulted in 49 compatible records that each group of seven records represent the ground motion hazard at a bridge site. The resultant matched records have then been incrementally scaled until one of the piers first reaches

its predefined yield, serviceability and damage-control limit states. The following two ratios have been considered from the results of IDA to compare with that of DDBA.

- **L.S./D. by IDA**

When one of the piers first reaches its predefined limit state displacement, the corresponding scale factor of the record is recorded as the LS/D ratio. The mean value of seven LS/D ratios for a limit state is considered as global LS/D ratio of the bridge for that particular limit state. The difference between the ratios of LS/D by IDA and DDBA is defined by percentage difference, given in equation 4.7, and variability in the scale factors investigated by sample standard deviation, given in equation 4.8.

$$\%Difference = \left| \frac{\bar{x} - DDBA}{\bar{x}} \right| \quad (4.7)$$

$$\sigma = \sqrt{\frac{\sum_i^n (x_i - \bar{x})^2}{n - 1}} \quad (4.8)$$

For a limit state of interest, x_i is the LS/D ratio for i^{th} acceleration record and \bar{x} is the mean of LS/D ratios of n records.

- **$S_d(T_{eff})/\Delta_{eq,sys}$**

$S_d(T_{eff})$ is the elastic spectral displacement (5% damping) corresponding to the effective period of a bridge for a limit state, and $\Delta_{eq,sys}$ is the elastic system displacement of the bridge for that limit state. Ideally, the ratio of $S_d(T_{eff})/\Delta_{eq,sys}$ would be around 1 if the applied DDBA approach was sufficiently accurate to estimate the system displacement of a bridge.

Table 4.11 Earthquake records used to generate compatible accelerograms with the ground-motion hazards

	PEER ID	Earthquake	Station	M_w
EQ1	180	Imperial Valley, CA 1979	El Centro Array #5	6.53
EQ2	848	Landers, CA 1992	Coolwater	7.28
EQ3	953	Northridge, CA 1994	Beverly Hills - 14145 Mulhol	6.69
EQ4	1111	Kobe, Japan 1995	Nishi-Akashi	6.90
EQ5	1158	Kocaeli, Turkey 1999	Duzce	7.51
EQ6	1205	Chi-Chi, Taiwan 1999	CHY041	7.62
EQ7	6923	Darfield, New Zealand 2010	Kaiapoi North School	7.00

Note: Earthquake records were selected from PEER NGA West2 database (PEER, 2019).

4.5.1 Computational Model for Incremental Dynamic Analysis

Incremental dynamic analysis have been performed with finite element software RUAUMOKO (Carr, 2017) which considers line elements with inelastic springs characterized by force-displacement hysteresis rules. The Modified Takeda hysteresis (Otani, 1974), shown in Figure 4.16, has been used to model both RC and RCFST piers. Unloading stiffness factor of $\alpha = 0.5$, reloading stiffness factor $\beta = 1$, and reloading stiffness power factor of 1 have been common parameters assigned to all pier models. The post-yield stiffness ratio, r , has been identified individually from moment-curvature response of the pier sections. RC and RCFST columns have been modeled as their clear heights and effective lengths, respectively. The top RC members in the RCFST piers have been modelled with a length of four times the top plastic hinge. In addition to length of RC and effective length of RCFST members, an elastic frame element which is a

length of half height of the cap beam ($0.5H_{cb}$) has been introduced between the cap-beam and the column in order to account for strain penetration at the yield limit state. Section properties of this elastic element are the same as elastic section properties of the column section below. Cap beam and superstructure have been modelled as rigid elements to be consistent with the assumptions made in DDBA calculations. Figure 4.17 illustrates typical examples of multi-column RC and RCFST bridge bent models employed for modelling the bridge bents. Constant average acceleration by Newmark (1959) has been chosen as numerical integration scheme in nonlinear analyses. Tangent stiffness proportional damping (with the secant damping matrix – ICTYPE 6) has been considered for the members that inelastic behavior is expected.

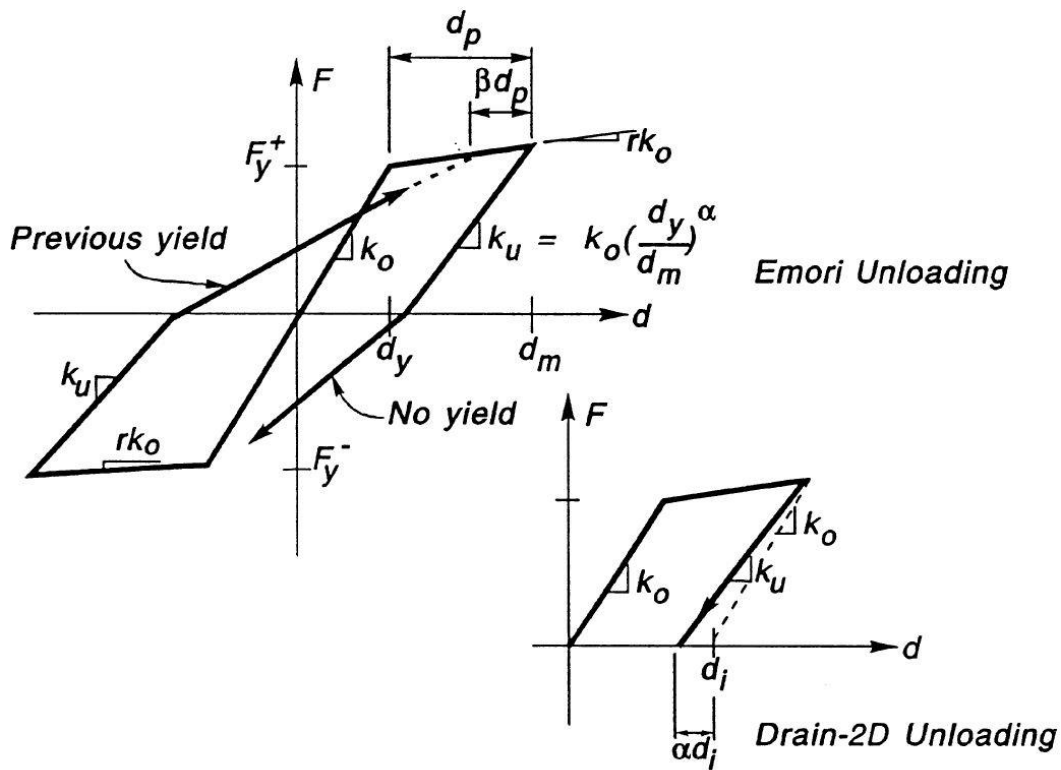


Figure 4.16 Modified Takeda hysteresis rule for RUAUMOKO analyses (Carr, 2017)

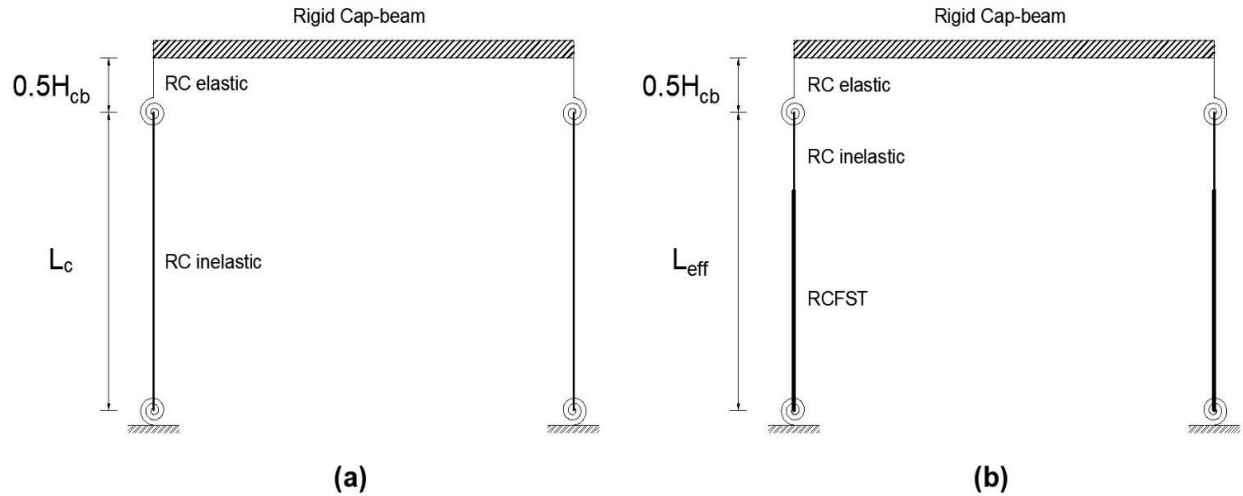


Figure 4.17 Examples of multi-column bent models for RUAMOKO: (a) RC bent (b) RCFST

4.5.2 Comparison of the Results

Figure 4.18, Figure 4.19 and Figure 4.20 show comparison of IDA results with DDBA estimations at yield, serviceability and damage-control performance limit states (PLS), respectively. Percentage differences at each PLS indicate that the applied DDBA approach satisfactorily estimates performance level of bridges (LS/D). From the DDBA estimations of 21 different assessment cases (the seven bridges at three PLS) presented in Figure 4.18, Figure 4.19 and Figure 4.20, for thirteen of them, (%62) LS/D is estimated with a percentage difference in the range of 0-5%, for seven of them (%33), LS/D is estimated with a percentage difference in the range of 5-10% and only for one of them (5%) is LS/D estimated with a percentage difference in the range of 10-15%.

Standard deviation of the scale factors, given in the data table of each figure, increases from yield to damage-control. This can be attributed to variability between the records. To exemplify, Table 4.12 shows displacement demand variability from the seven records matched to the hazard of BN1903 at effective yield, serviceability and damage-control limit state period of

BN1903, and these limit state displacement demands are plotted in Figure 4.21. As can be seen from Table 4.12 and Figure 4.21 that displacement demand variability between the records has increasing trend as the limit state period goes from yield to damage-control. Similar trends have also been seen from the records matched to the other ground motion hazards. Therefore, it is expected to see a higher scatter of scale factors from IDA results for damage-control limit states as opposed to serviceability and yield. However, as stated above, the applied DDBA methodology reasonably estimates the global response of the bridges at the considered PLS.

Figure 4.12 shows the ratios of limit state displacement demands from IDA analyses to the elastic limit state system displacements obtained from DDBA at yield, serviceability and damage-control PLS. The Overall ratios, given in Table 4.12, are close to 1.0 with some scatter of 0.03, 0.10 and 0.13 for yield, serviceability and damage-control, respectively. The reason of more scatter at serviceability and damage-control compared to yield is the increase in variability of IDA results from yield to damage-control PLS, as discussed above.

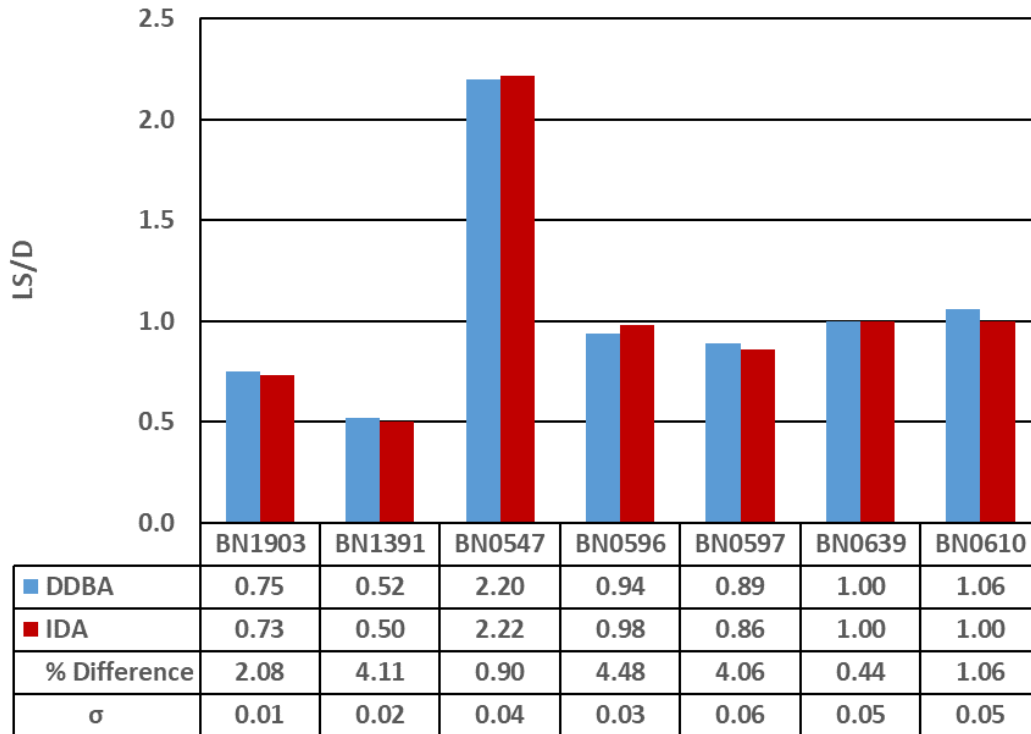


Figure 4.18 Comparison of IDA and DDBA at yield performance level

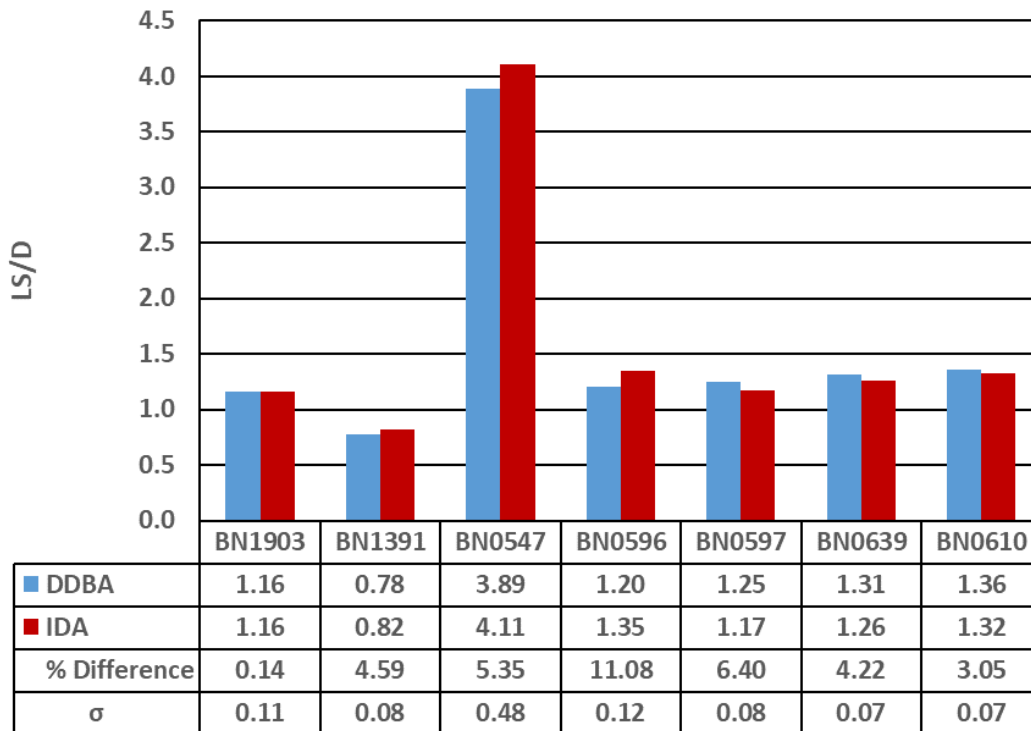


Figure 4.19 Comparison of IDA and DDBA at serviceability performance level

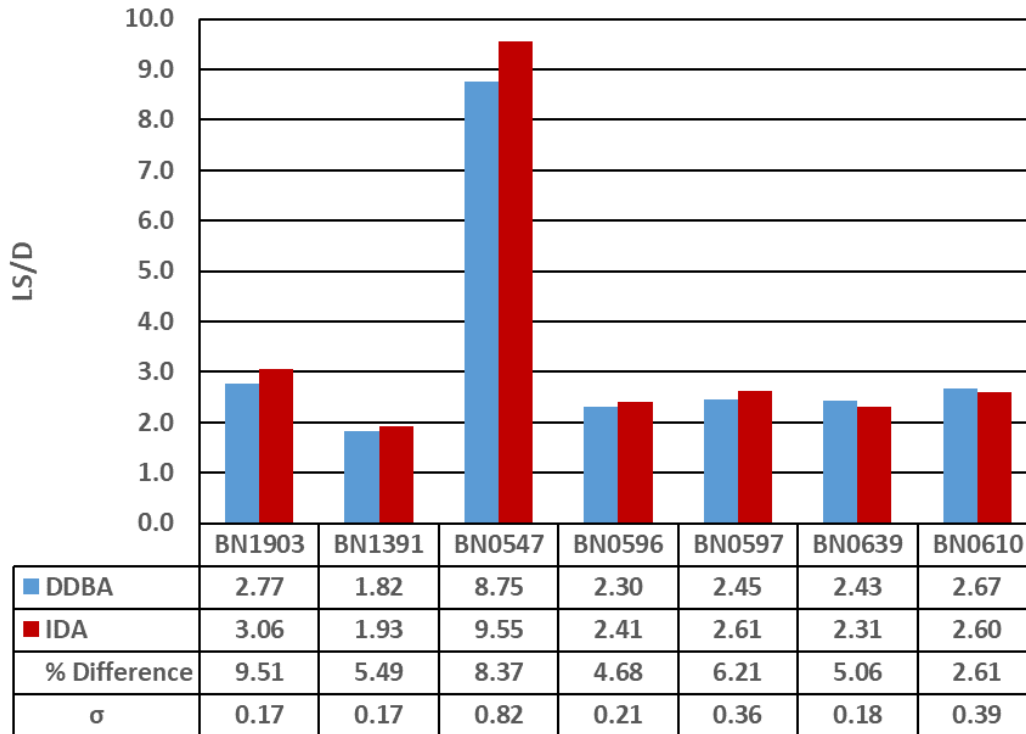


Figure 4.20 Comparison of IDA and DDBA at damage-control performance level

Table 4.12 BN1903 Limit state displacement demands from the matched records

	Sd at 1.18s	Sd at 1.42s	Sd at 2.41s
EQ1	0.118	0.131	0.232
EQ2	0.118	0.141	0.240
EQ3	0.112	0.143	0.228
EQ4	0.118	0.140	0.248
EQ5	0.117	0.136	0.242
EQ6	0.123	0.139	0.239
EQ7	0.122	0.137	0.275
Standard deviation	0.0025	0.004	0.015

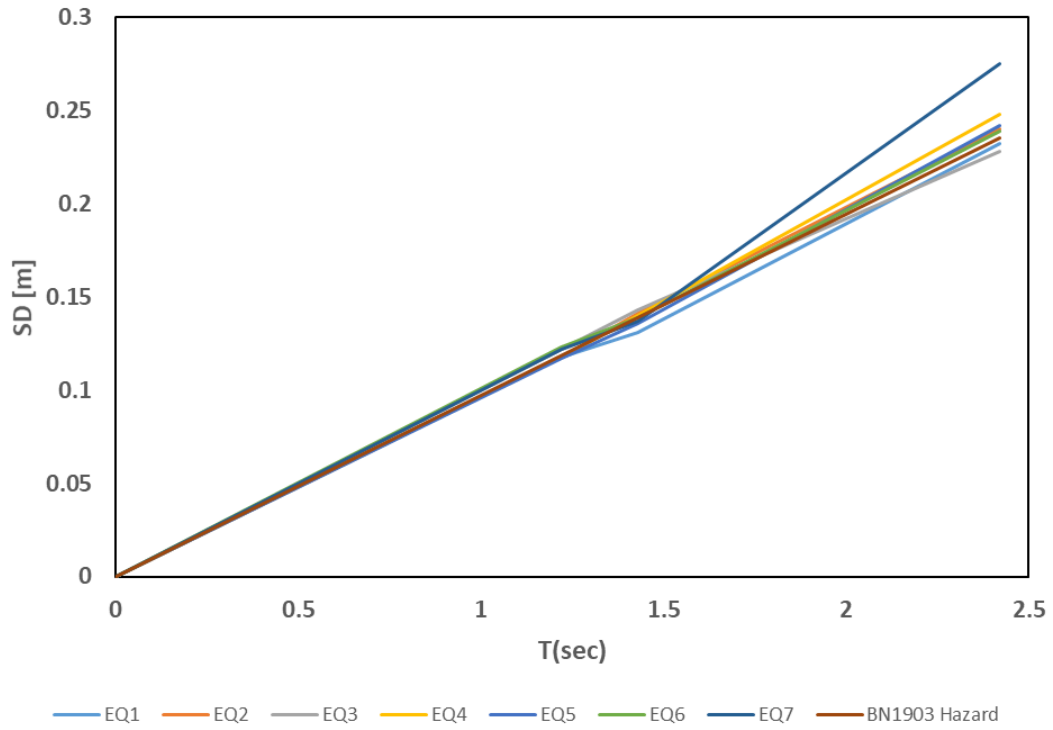


Figure 4.21 Spectral displacement responses of the seven records matched to BN1903 hazard

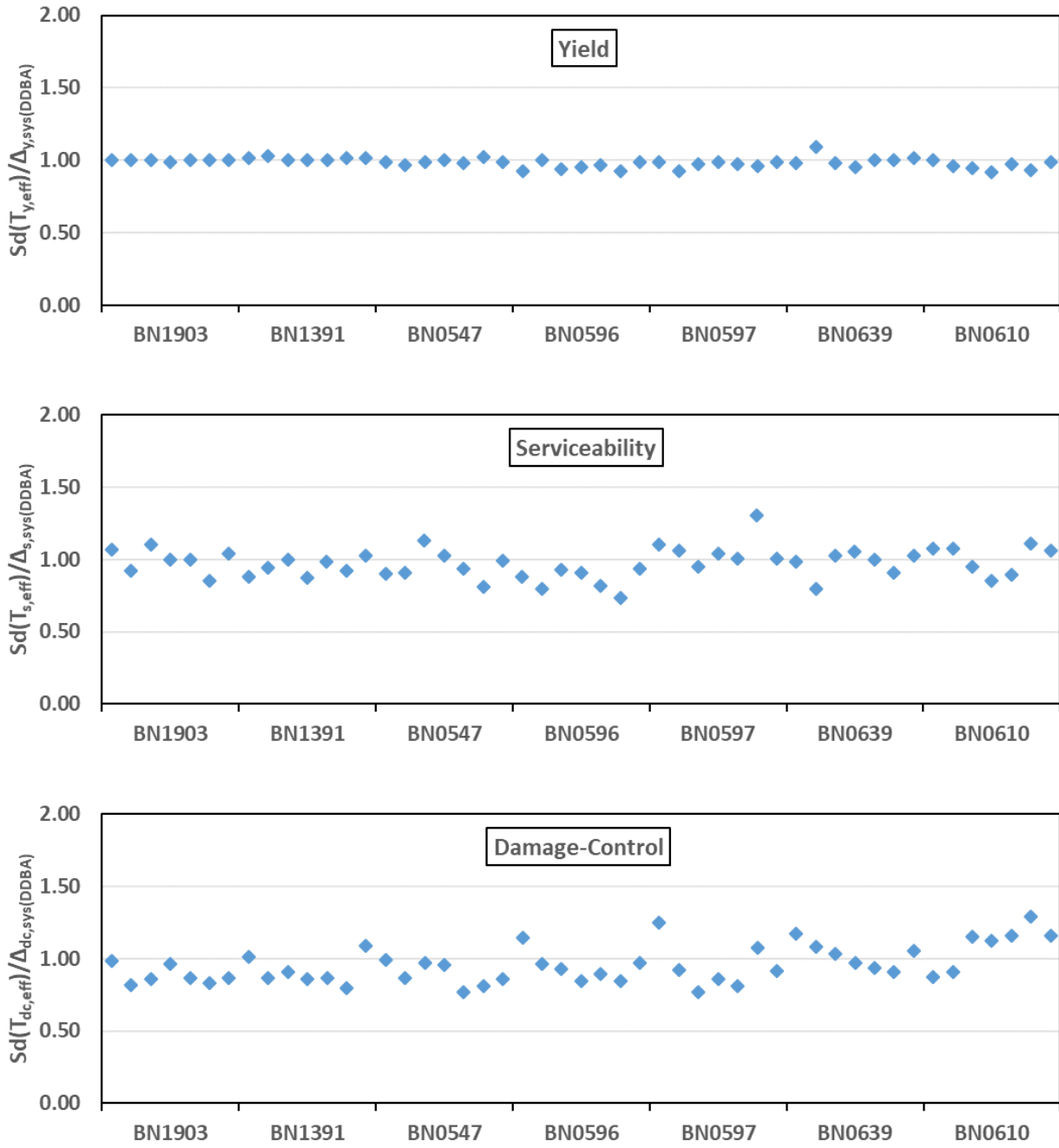


Figure 4.22 $Sd(T_{eff})/\Delta_{sys}(DDBA)$ ratios for Yield, Serviceability and Damage-Control performance limit states

Table 4.13 Mean and Standard deviation for ratio $S_d(T_{eff})/\Delta_{sys}(DDBA)$

Performance Level	Mean	Standard Deviation
Yield	0.98	0.03
Serviceability	0.97	0.10
Damage-Control	0.96	0.13

In this section, yield, serviceability and damage-control performance level of the case study bridges estimated by DDBA have been tested under a scenario earthquake processed by ShakeMap. Different level of ground-motion hazards at the bridge sites have been generated by fitting location-specific ShakeMap outputs to the generalized response spectrum shape. The next section will discuss how rapid seismic assessment of a bridge whose system parameters are defined by DDBA can be conducted for a real event given the IMTs at the bridge location by ShakeMap.

4.6 Rapid Post-Earthquake Assessment Application under 2018 Anchorage Earthquake

A magnitude 7.1 earthquake hit Anchorage, AK on November 30, 2018. The epicenter of the earthquake was 14km north of the central district of Anchorage with a depth about 46.7km ("2018 Anchorage-Earthquake", 2019). The ShakeMap of the event was released minutes after the earthquake by USGS with an event ID of ak20419010 ("2018 Anchorage-Earthquake", 2019). The intensity map of the earthquake, shown in Figure 4.23, shows that the areas in which BN1903, 1391 and 0639 are located experienced high ground shaking. Rapid assessment of these three bridges was conducted to ascertain which limit state was achieved. Location-specific IMTs provided by ShakeMap were used to generate seismic demands at the bridge sites. Table 4.14 shows ShakeMap IMTs at the bridge sites and epicentral distance, r , of the bridges. It is worth noting that the seismic demand at BN1903 site is higher than that of BN1391 although BN1391 is closer than BN1903 to the epicenter. This indicates that earthquake rupture directivity is more

predominant to the north of the epicenter than towards the south, which is also noticeable in the intensity map of the event, shown in Figure 4.23. Four-point acceleration response spectrum was generated connecting PGA, SA[0.3s], SA[1.0s] and SA[3.0s] values given at each bridge site. Displacement response spectrum were then generated converting acceleration values into the displacements using Eq. (4.6). Acceleration and displacement response spectrum at each bridge site is shown in Figure 4.24 and Figure 4.25, respectively. Since seismic demand at the bridge sites were low, only yield performance level of the bridges was checked. Figure 4.26 shows yield performance level estimations (LS/D) of the bridges under this earthquake. Since all LS/D ratios are bigger than 1.0, none of the bridges are expected to achieve their yield performance level. However, it is a limitation of this study that equivalent system properties of the bridges were defined by only column damages assuming no abutment resistance. In reality, there would be abutment resistance hence damages at the abutment of these bridges such as shear key failures could be possible. Estimated yield performance level outcomes of these bridges were reported to AK DOT. Except a minor shear key damage on BN1391 there was no significant damage observed from post-earthquake visual inspection of these bridges (information provided by Elmer Marx, personal correspondence).

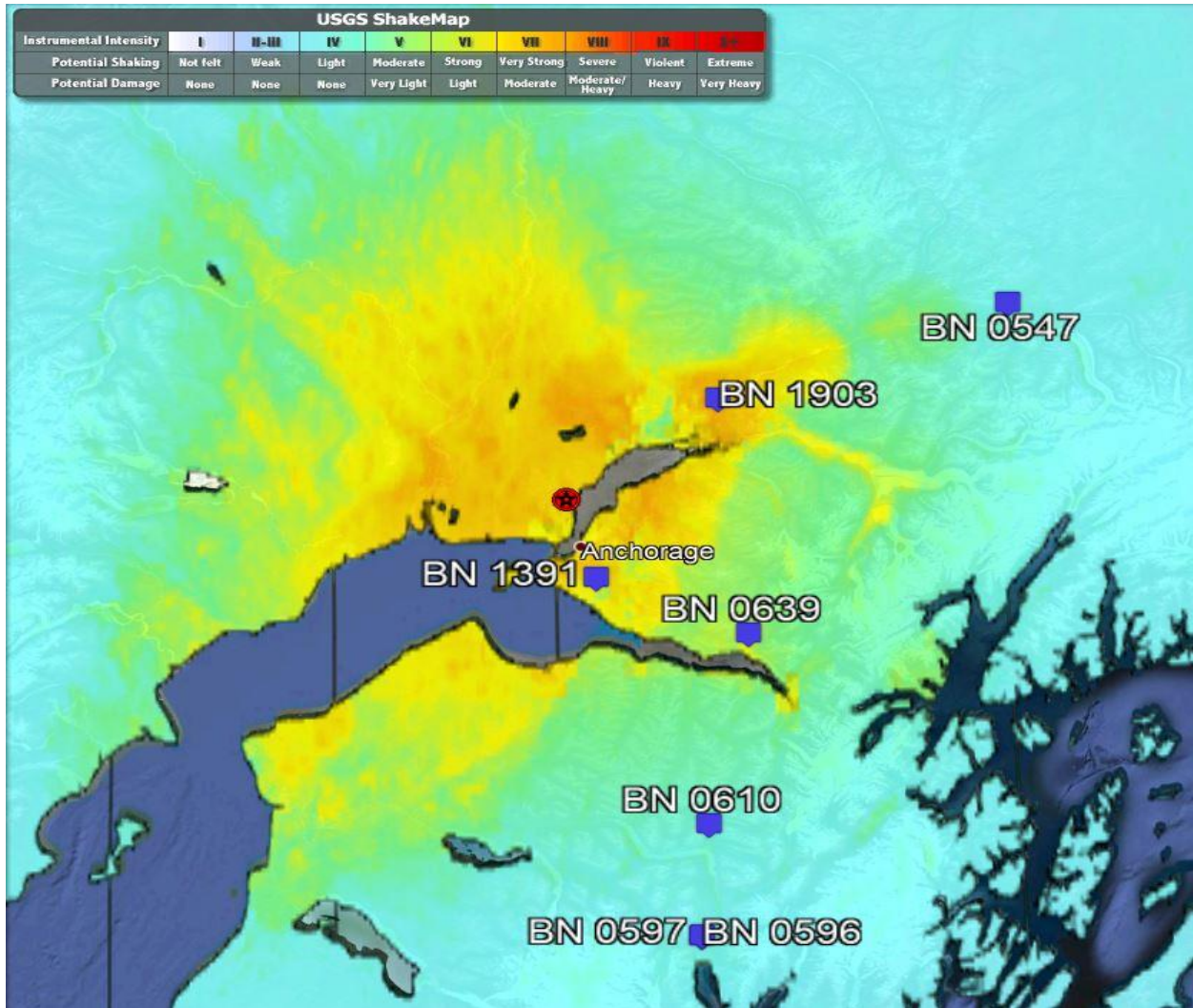


Figure 4.23 Intensity overlay of Anchorage earthquake (Google Earth, 2019)

Table 4.14 Intensity measure outputs and epicentral distances

Bridge ID (BN)	PGA (g)	PGV (cm/s)	SA[0.3s] (g)	SA[1.0s] (g)	SA[3.0s] (g)	<i>r</i> (km)
1903	0.40	25.30	0.76	0.20	0.06	91.5
1391	0.27	13.56	0.57	0.12	0.03	48.9
0639	0.17	11.65	0.31	0.09	0.02	121

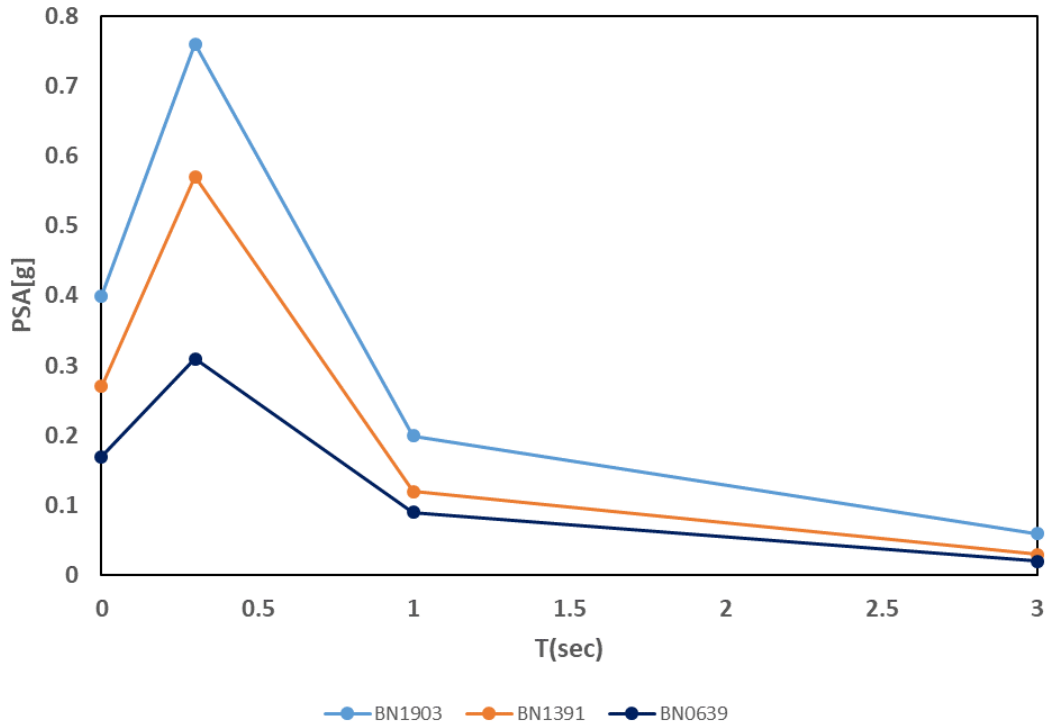


Figure 4.24 Four-point acceleration response spectrum

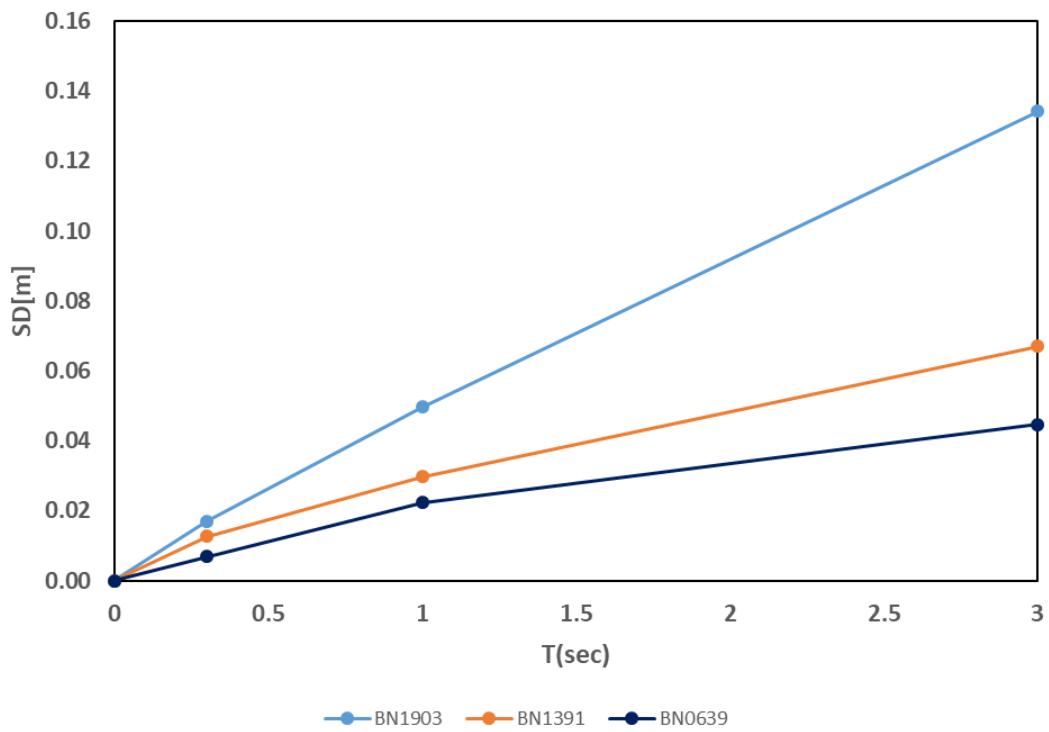


Figure 4.25 Four-point displacement response spectrum

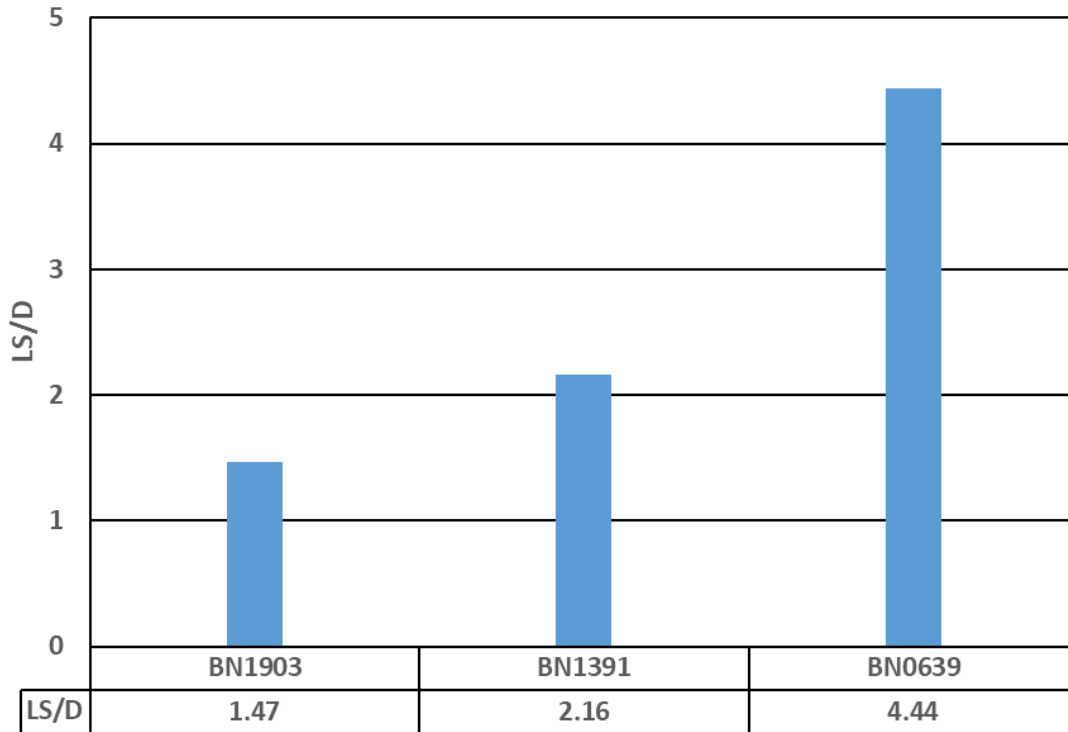


Figure 4.26 Yield performance level under 2018 Anchorage earthquake

4.7 Conclusion

In this chapter, applications of a rapid-assessment plan for AK Highway bridges were shown for a scenario and a real earthquake. According to the proposed plan, assessment of a bridge can be conducted if deformation limit states of the bridge, and seismic demands at those limit states are known. To that end, equivalent system properties of a set of bridges (3 RC and 4 RCFST) from AK were identified at yield, serviceability and damage-control PLS following the principles of DDBD. Scenario-based assessment application of the case study bridges was conducted under an earthquake scenario processed by ShakeMap. Soil amplified ShakeMap intensity measure values at the bridge locations were fitted into the generalized acceleration response spectrum shape to characterize seismic demands at the bridge sites. Yield, serviceability and damage-control performance level of the bridges have been defined by the ratio of limit state displacement to the

corresponding seismic demand (LS/D). Based on the LS/D ratios, one bridge reached serviceability, four bridges reached yield and two bridges remained elastic under the considered earthquake scenario. Reliability of the LS/D ratios was checked running IDA of the bridges. The results of IDA showed that DDBA was capable of estimating performance level of the bridges with reasonable accuracy for the three PLS. Finally, application of ShakeMap for a real event (2018 Anchorage AK Earthquake M7.1) was shown by conducting assessment of two RC and one RCFST bridges by the DDBA approach. DDBA performance level estimations indicated that all three-bridge remained elastic during this earthquake.

4.8 Discussion and Future Research

This research is intended to develop a displacement-based rapid assessment approach for Alaska highway bridges. The proposed approach uses a DDBA method to characterize bridge system properties for a performance level of interest. The following additions can be considered in the future to further develop a more comprehensive DDBA procedure for Alaska bridges.

- Displacement contributions due to shear deformations and foundation flexibility can be considered to increase accuracy of limit state displacements.
- Strength loss due to geometric nonlinearity such as, P- Δ effects, can be accounted for to better characterize strength levels at bridge performance levels.
- Additional column limit state displacements, particularly for RC columns, can be identified to account for low temperature effect on deformation capacity of bridge columns. For example, the studies of Montejo et al., (2008 and 2009) found that RC columns demonstrate lower displacement capacity at freezing temperatures than at ambient conditions.
- Performance limit states should be extended to other bridge components such as abutments, shear keys, and bearings, among others.

- The effect of soil on limit state displacements can be included considering the change of soil rigidity in summer (flexible soil) and winter (rigid soil) seasons.

The above-mentioned suggestions would provide a more precise evaluation of bridge performance levels. Once new limit states are introduced, the application process of the DDBA is the same in terms of obtaining equivalent system properties for a performance level of interest. The challenges are expected, however, for identifying which of the bridge elements will first reach its predefined limit state displacement and what will be the corresponding displaced shape along the bridge, as recognized by Priestley et al. (2007).

The ShakeMap tool has been used in this study to define the seismic hazard level at the bridge sites. The tool is invaluable in providing site-specific ground motion parameters after a very short time of an earthquake. While currently ShakeMap provides PSA at 0.3, 1.0 and 3.0 seconds for a site, the developers of ShakeMap aim to release PSAs at 20 response periods in the near future (Wald et al., 2017). Such an improvement would help to define seismic demands more accurately at effective periods across performance levels. Another important feature of ShakeMap is its ability to run scenario earthquakes by assuming a particular magnitude, location, and fault geometry. Once these three parameters are provided to ShakeMap, ground shaking levels can be estimated for a specified region by selecting a GMPE. The GMPE library in the ShakeMap software helps users to select GMPEs that are suitable for specific faulting mechanisms of the region. The most challenging part of creating scenario events from ShakeMap would be to decide on the parameters of magnitude and fault geometry for a location of interest. As stated previously, seismic hazard disaggregation analysis could help to evaluate these two parameters, or seismologists could provide the parameters for specific location of interests, or available

ShakeMap scenario earthquakes generated by USGS for the Alaska region (one of them shown in this study) could be referred to for assessing bridges under scenario earthquakes.

REFERENCES

- 20 Largest Earthquakes in the World. (n.d.). Retrieved April 27, 2019, from <https://earthquake.usgs.gov/earthquakes/browse/largest-world.php>
- 2018 Year in Review | Alaska Earthquake Center. (n.d.). Retrieved April 27, 2019, from <https://earthquake.alaska.edu/2018-year-review>
- About earthquakes in Alaska | Alaska Earthquake Center. (n.d.). Retrieved April 27, 2019, from <https://earthquake.alaska.edu/earthquakes/about>
- Aguirre, R.A.D. (2017). *Seismic Performance and Displacement Capacity of RCFST Drilled Shafts*. North Carolina State University.
- Alan Yong, Eric M. Thompson, David J. Wald, Keith L. Knudsen, Jack K. Odum, William J. Stephenson, and S. H. (2016). *Compilation of Vs30 Data for the United States*.
- ANTONIOU, S., & PINHO, R. (2004). Development and Verification of a Displacement-Based Adaptive Pushover Procedure. *Journal of Earthquake Engineering*, 8(5), 643–661. <https://doi.org/10.1080/13632460409350504>
- ASTM A706 / A706M - 16 Standard Specification for Deformed and Plain Low-Alloy Steel Bars for Concrete Reinforcement. (n.d.). Retrieved April 2, 2019, from <https://www.astm.org/Standards/A706.htm>
- Basoz, N., & Mander, J. B. (1999). *Enhancement of the Lifeline Transportation Module in HAZUS, Report Draft #7, National Institute of Building Sciences, Washington, D.C.*

- Biasi, G., Mohammed, M. S., & Sanders, D. H. (2016). Earthquake Damage Estimations: ShakeCast Case Study on Nevada Bridges. *Earthquake Spectra*, 33(1), 45–62. <https://doi.org/10.1193/121815EQS185M>
- Cardone. (2014). Displacement limits and performance displacement profiles in support of direct displacement-based seismic assessment of bridges. *Earthquake Engineering and Structural Dynamics*, 43(8), 1239–1263. <https://doi.org/10.1002/eqe>
- Cardone, D., Capone, V., Perrone, G., & Petrini, L. (2011). Direct Displacement-Based Seismic Assessment of Multi-Span Simply Supported Deck Bridges. In *Thematic Conference on Computational Methods in Structural Dynamics and Earthquake Engineering*. Retrieved from http://congress.cimne.com/eccomas/proceedings/compdyn2011/compdyn2011_full/178.pdf
- Carr., A. J. (2017). *RUAUMOKO: The Maori God of Volcanoes and Earthquakes*. Christchurch, New Zealand.
- D. J. Wald, K. Lin, C.A. Kircher, K. Jaiswal, N. Luco, L. Turner, and D. Slosky. (2017). Development and Utilization of USGS ShakeCast for Rapid Post-Earthquake Assessment of Critical Facilities and Infrastructure (pp. 1–15). Santiago, Chile.
- ERDIK, M. (2001). *Report on 1999 Kocaeli and Düzce (Turkey) Earthquakes. Report on 1999 Kocaeli and Düzce (Turkey) Earthquakes*. https://doi.org/10.1142/9789812811707_0018
- Faccioli, E., Paolucci, R., & Rey, J. (2004). Displacement Spectra for Long Periods, 20(2), 347–376. <https://doi.org/10.1193/1.1707022>

- Goodnight, J. C., Kowalsky, M. J., & Nau, J. M. (2016). Strain limit states for circular RC bridge columns. *Earthquake Spectra*, 32(3), 1627–1652. <https://doi.org/10.1193/030315EQS036M>
- Google, Google Earth. (n.d.). Retrieved April 13, 2019, from <https://www.google.com/earth/>
- HAZUS-MH. Multi-Hazard Loss Estimation Methodology: Earthquake Model HAZUS-MH MR5 Technical Manual*, Federal Emergency Management Agency, Washington D.C. (2011).
- King D.J., Priestley M.j.N., and P. R. (1986). *Computer Programs for Concrete Column Design*. New Zealand.
- Koehler, R. D. and, & Carver, G. A. (2018). *ACTIVE FAULTING AND SEISMIC HAZARDS IN ALASKA*.
- Kong, C. and Kowalsky, M. J. (2016). Impact of Damping Scaling Factors on Direct Displacement-Based Design. *Earthquake Spectra*, 32(2), 843–859. <https://doi.org/10.1193/021815EQS031M>
- Kowalsky, M. J. (2002). A displacement-based approach for the seismic design of continuous concrete bridges. *Earthquake Engineering and Structural Dynamics*, 31(3), 719–747. <https://doi.org/10.1002/eqe.150>
- M 7.1 - 14km NNW of Anchorage, Alaska. (n.d.). Retrieved April 26, 2019, from <https://earthquake.usgs.gov/earthquakes/eventpage/ak20419010/executive>
- Mander, J. B., Priestley, M. J. N., & Park, R. (1988). Theoretical Stress-Strain Model for Confined Concrete. *Journal of Structural Engineering*, 114(8), 1804–1826. [https://doi.org/10.1061/\(ASCE\)0733-9445\(1988\)114:8\(1804\)](https://doi.org/10.1061/(ASCE)0733-9445(1988)114:8(1804))

- Montejo, L. A., Kowalsky, M. J., and H. T. (2008). “*Seismic Design of Reinforced Concrete Bridge Columns at Subfreezing Temperatures*,” *CFL Technical Reprt No. RD-08-01*,. Raleigh, North Carolina.
- Montejo, L. A., Asce, S. M., Sloan, J. E., Asce, A. M., Kowalsky, M. J., Asce, A. M., ... Asce, A. M. (2008). Cyclic Response of Reinforced Concrete Members at Low Temperatures, 22(3), 79–102.
- Montejo, L. A., González-Román, L. A., & Kowalsky, M. J. (2012). Seismic performance evaluation of reinforced concrete-filled steel tube pile/column bridge bents. *Journal of Earthquake Engineering*, 16(3), 401–424. <https://doi.org/10.1080/13632469.2011.614678>
- Montejo, L. A., & Kowalsky, M. J. (2007). *CUMBIA Set of codes for the analysis of reinforced concrete members*. *CFL Technical Rep. No.IS-07-01*. Raleigh, North Carolina. <https://doi.org/Tachnical Report IS-07-01>
- Montejo, L. A., Kowalsky, M. J., & Hassan, T. (2009). Seismic Behavior of Flexural Dominated Reinforced Concrete Bridge Columns at Low Temperatures. *ASCE Journal of Cold Regions Engineering*, 23(1), 18–42.
- Montejo, L. A., & Suarez, L. E. (2013). An improved CWT-based algorithm for the generation of spectrum-compatible records. *International Journal of Advanced Structural Engineering*. <https://doi.org/10.1186/2008-6695-5-26>
- National Bridge Inventory Data, U.S. Department of Transportation, Federal Highway Administration, Washington D.C, available at <https://www.fhwa.dot.gov/bridge/nbi/ascii.cfm>. (2010).

NEHRP RECOMMENDED PROVISIONS FOR SEISMIC REGULATIONS FOR NEW BUILDINGS AND OTHER STRUCTURES (FEMA 450). (2003). Washington, D.C.

Newmark, N.M. (1959). A method of Computation for Structural Dynamics. *Journal of the Engineering Mechanics Division, ASCE*, 85(3), 67–94.

Otani C. (1974). *SAKE: A Computer Program for Inelastic Response of R/C Frames to Earthquakes*, Report UILU-Eng-74-2029,. URBANA, ILLINOIS.

PEER Ground Motion Database -PEER Center. (n.d.). Retrieved April 22, 2019, from <https://ngawest2.berkeley.edu/>

POLA Seismic Code. (2010). *POLA. The Port of Los Angeles Code for Seismic Design, Upgrade and Repair of Container Wharves*. Los Angeles, California.

Priestley M.J.N., Calvi G.M., and Kowalsky M.J. (2007). *Displacement-Based Seismic Design of Structures*. Pavia, Italy: IUSS PRESS.

Rezaeian, S., Bozorgnia, Y., Idriss, I. M., Abrahamson, N. A., Campbell, K. W., and Silva, W. J. (2014). Damping Scaling Factors for Elastic Response Spectra for Shallow Crustal Earthquakes in Active Tectonic Regions : “ Average ” Horizontal Component. *Earthquake Spectra*, 30(2), 939–963. <https://doi.org/10.1193/100512EQS298M>

Sadan, O.S., Petrini, L. and Calvi, G. M. (2013). Direct displacement-based seismic assessment procedure for multi-span reinforced concrete bridges with single-column piers. *Earthquake Engineering and Structural Dynamics*, 7(42), 1031–1051. <https://doi.org/10.1002/eqe>

Steel Rebar Sizes - Steel Rebar Stock | Harris Supply Solutions. (n.d.). Retrieved April 2, 2019,

from <https://www.harrissupplysolutions.com/steel-rebar-sizes-stock.html>

USGS Alaska Mainshock M9.2 Scenario. (n.d.). Retrieved April 15, 2019, from https://earthquake.usgs.gov/scenarios/eventpage/gllegacynep2014mainshockm9p2_se/shake-map/metadata

USGS Scenario Catalogs. (2019). Retrieved March 6, 2019, from <https://earthquake.usgs.gov/scenarios/catalog/>

USGS Vs30 Models and Data. (n.d.). Retrieved April 17, 2019, from <https://earthquake.usgs.gov/data/vs30/>

Vamvatsikos, D., & Cornell, C. A. (2002). Incremental dynamic analysis, *31*(January 2001), 491–514. <https://doi.org/10.1002/eqe.141>

Wald, D., J., V. Quitoriano, T.H. Heaton, and H. K. (1999). Relationships between Peak Ground Acceleration, Peak Ground Velocity, and Modified Mercalli Intensity in California, 557–564.

Worden, C. B., Gerstenberger, M. C., Rhoades, D. A., & Wald, D. J. (2012). Probabilistic relationships between ground-motion parameters and modified mercalli intensity in California. *Bulletin of the Seismological Society of America*, *102*(1), 204–221. <https://doi.org/10.1785/0120110156>

Worden, C. B., & Wald, D. (2016). *ShakeMap Manual Release*.

Worden, C. B., Wald, D. J., Allen, T. I., Lin, K., Garcia, D., & Cua, G. (2010). A revised ground-motion and intensity interpolation scheme for shakemap. *Bulletin of the Seismological Society of America*, *100*(6), 3083–3096. <https://doi.org/10.1785/0120100101>

Yamakawa, K. (1998). *The Prime Minister and the earthquake: Emergency Management Leadership of Prime Minister Marayama on the occasion of the Great Hanshin-Awaji earthquake disaster*, *Kansai Univ. Rev. Law and Politics* 19,.

Zhao, J. X., Zhang, J., Asano, A., Ohno, Y., Oouchi, T., Takahashi, T., ... Fukushima, Y. (2006). Attenuation Relations of Strong Ground Motion in Japan Using Site Classification Based on Predominant Period, 96(3), 898–913. <https://doi.org/10.1785/0120050122>

APPENDIX

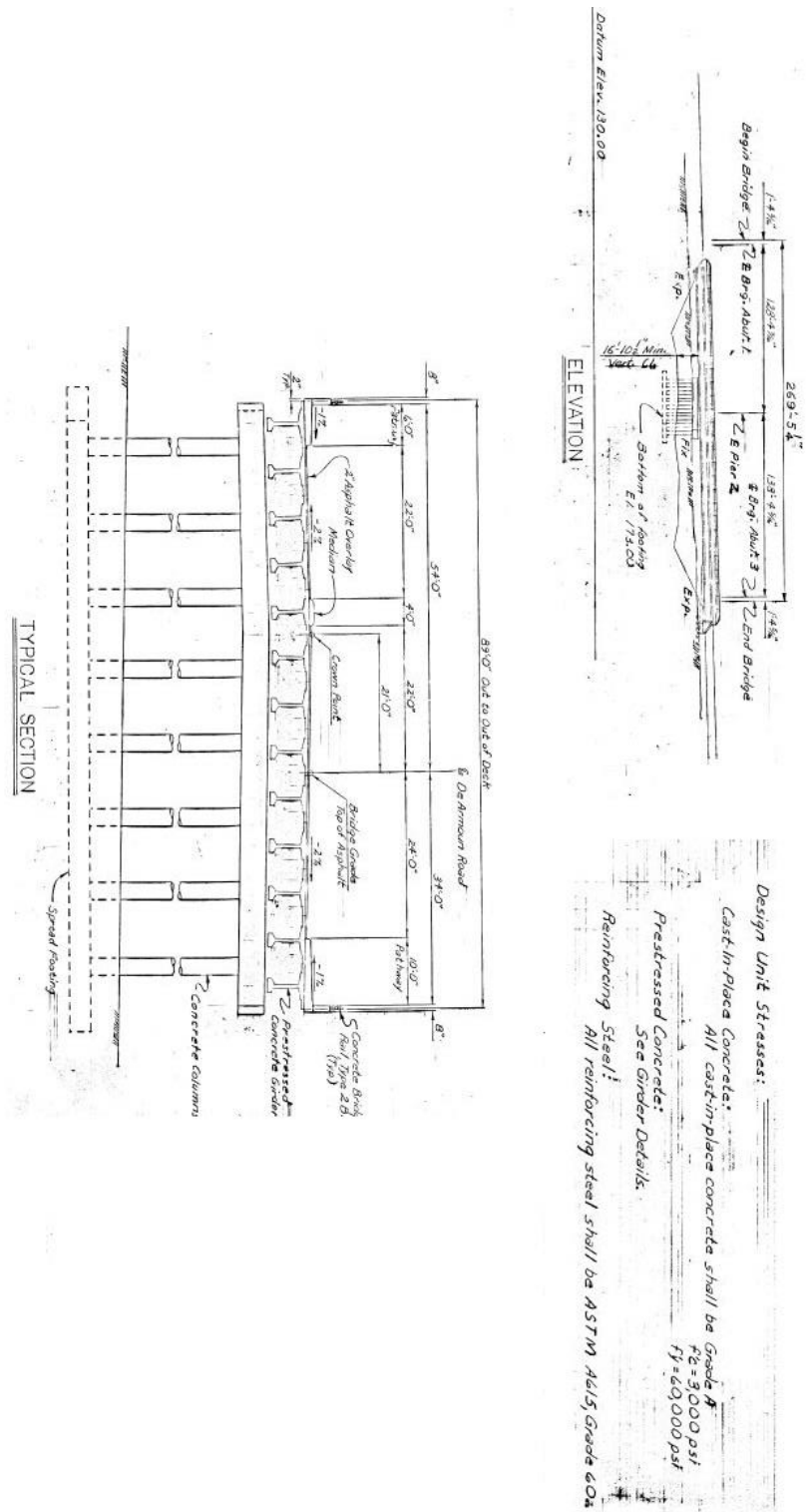


Figure A.3 BN1391 material properties, elevation and bent section views (dimensions are in U.S. units)

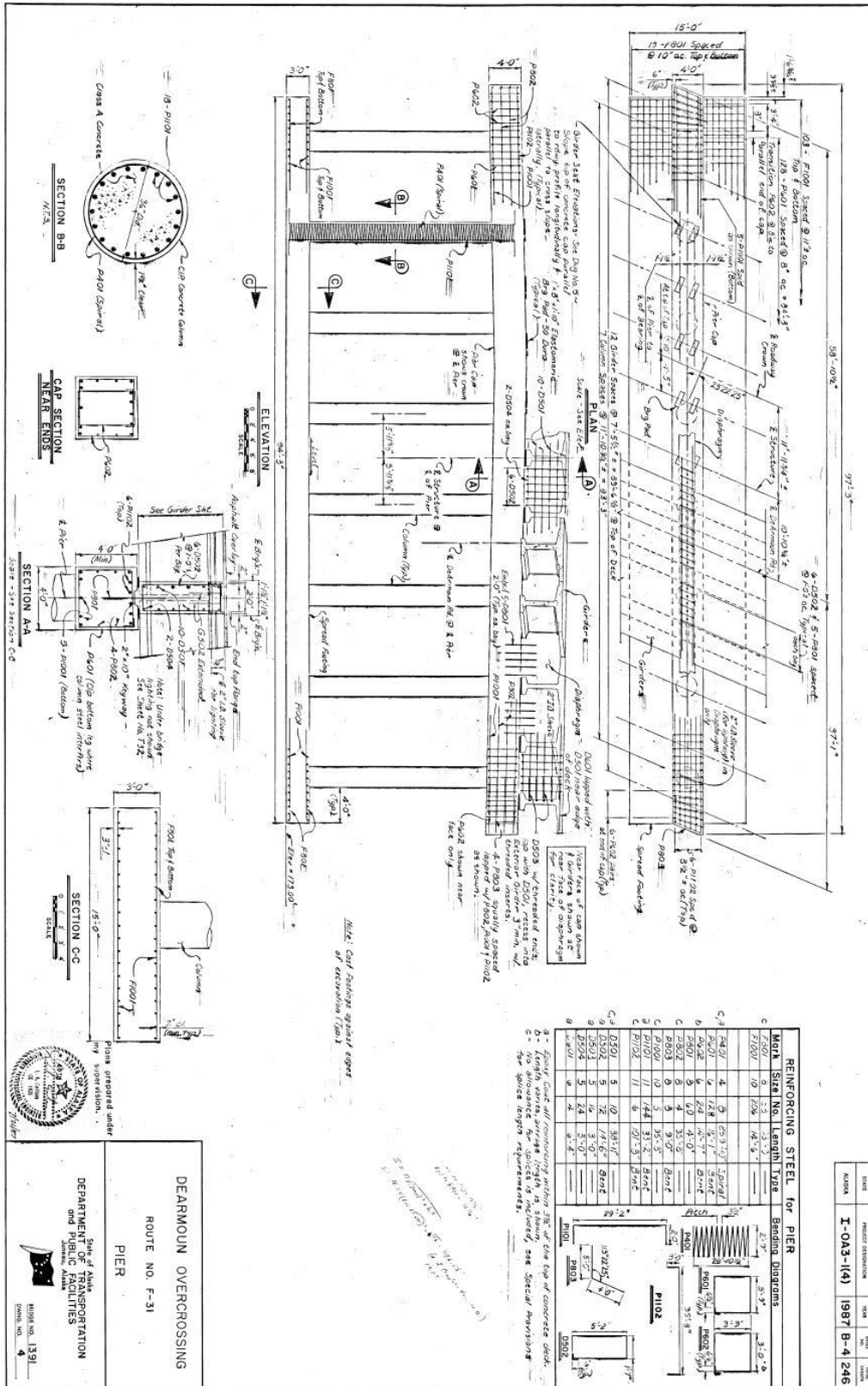


Figure A.4 BN1391 pier details (dimensions are in U.S. units)

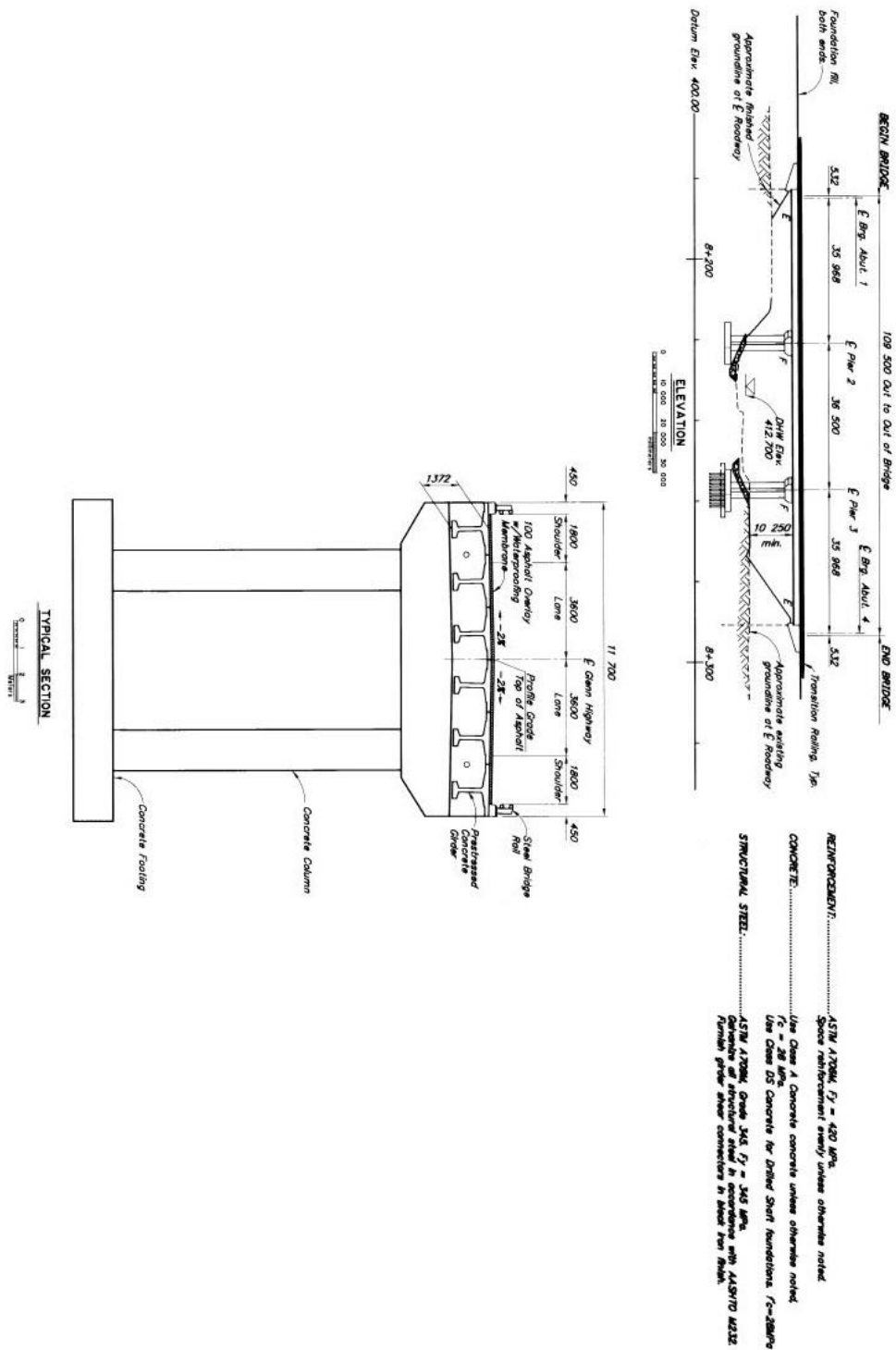


Figure A.5 BN0547 material properties, elevation and bent section views (elevations are in meters and other dimensions are in millimeters)

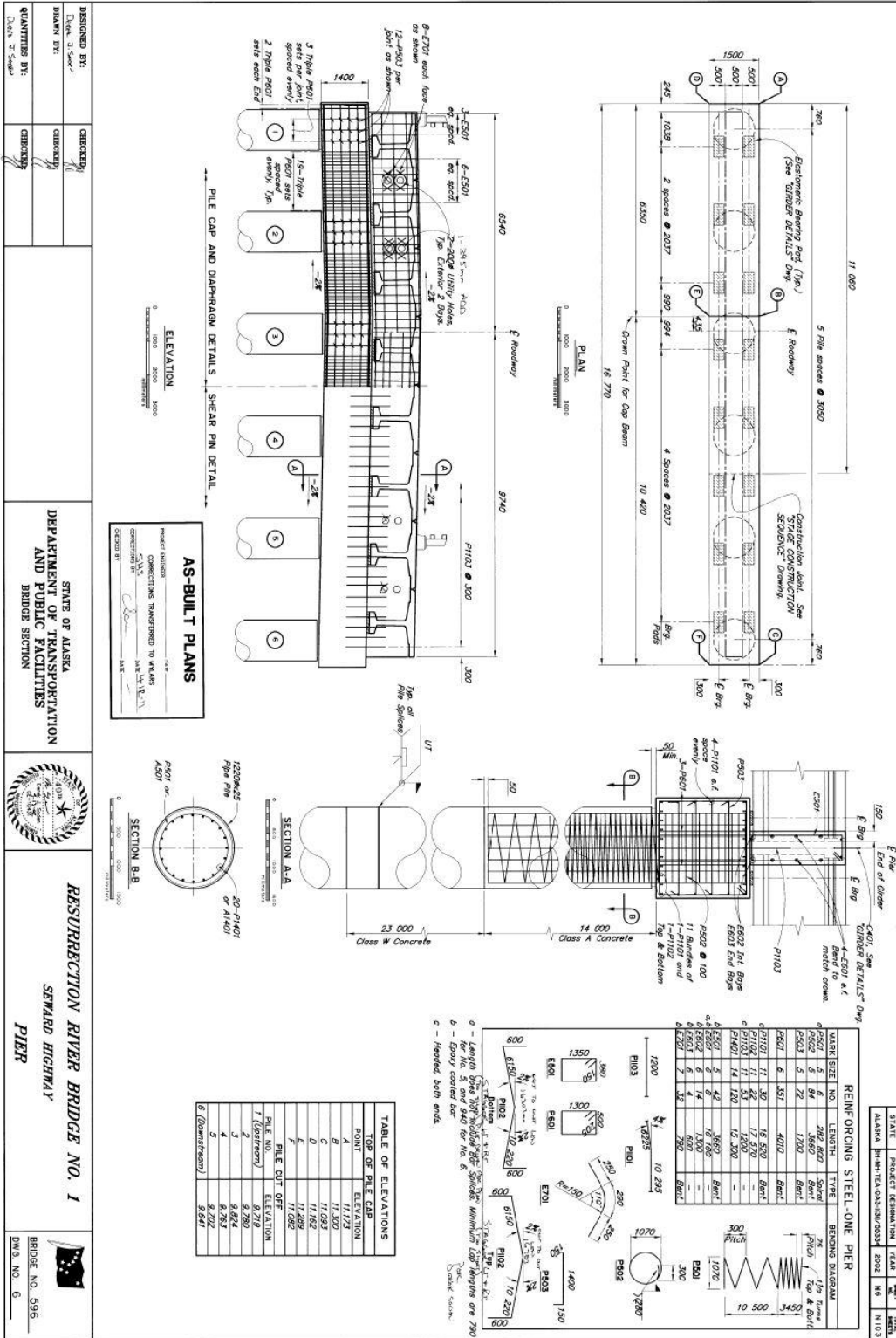


Figure A.8 BN0596&97 pier details (elevations are in meters and other dimensions are in millimeters)

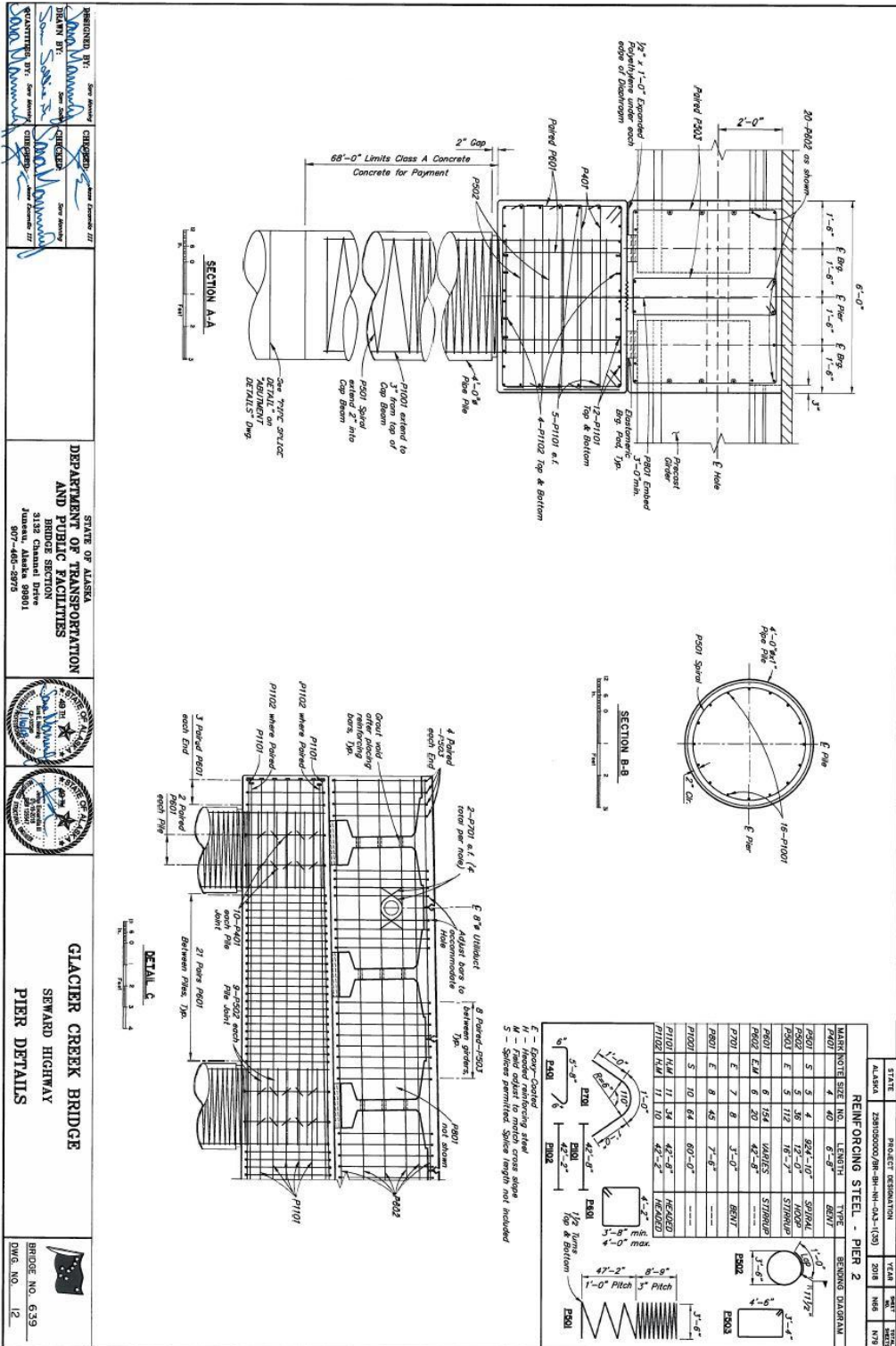


Figure A.10 BN0639 pier details (dimensions are in U.S. units)

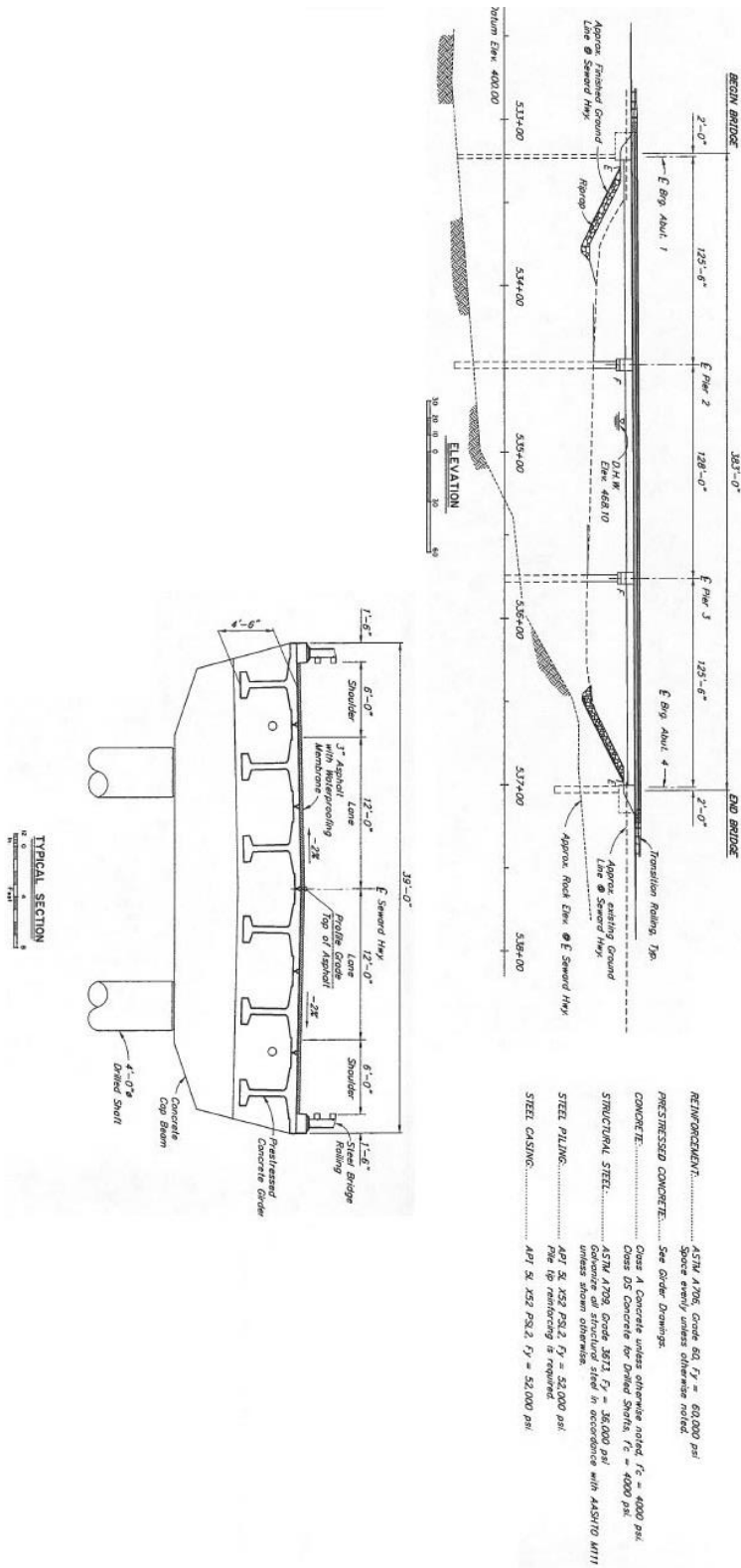


Figure A.11 BN0610 material properties, elevation and bent section views (dimensions are in U.S. units)

